POLITECNICO DI MILANO

DEPARTMENT OF CHEMISTRY, MATERIALS AND CHEMICAL ENGINEERING
"GIULIO NATTA"
DOCTORAL PROGRAMME IN MATERIALS ENGINEERING

INVESTIGATION OF RADIATION DAMAGE EFFECTS IN HL-LHC COLLIMATOR MATERIALS

Author:
Carlotta Accettura

CERN Supervisor:
Alessandro Bertarelli

Academic Supervisor:
Marco Beghi

June 2021 – XXXIII cycle

Abstract

The study of the effects of radiation-matter interaction is of great importance in the nuclear energy industry. Particle physics laboratories operating high-energy and high-intensity particle accelerators developed a growing interest in this field, as the radiation level is increasing with the stored beam energy.

The results presented in this work focus on the consequence of radiation damage on accelerators equipment and, in particular, on collimators. This PhD thesis has been carried out at the European Organization for Nuclear Research (CERN), located in Geneva (Switzerland), where the Large Hadron Collider (LHC), the world's largest accelerator, is operating. The High-Luminosity upgrade of the LHC (HL-LHC) is designed to operate with high-intensity beams, whose stored energy is about 700 MJ.

The interaction of particles with collimators induces microscopic defects in the materials, which affect the thermo-physical, electrical and mechanical properties. The evolution of the components during the accelerator lifetime is fundamental to understand if a correct operation can be guaranteed.

The aim of this thesis is to study the radiation damage on novel composite materials, specifically developed for HL-LHC collimators. In particular, ion irradiation is used to simulate the effects of protons. The use of ions has indeed numerous advantages, including the low activation induced in the irradiated material, which simplify the post-irradiation examination.

The range of the analysed materials includes two grades of molybdenum carbide-graphite composites, one of those is selected as absorber of the new HL-LHC collimators. As a comparison, carbon-fibre-carbon and isotropic polycrystalline graphite are irradiated. The irradiation test is conducted also on some samples coated with metallic films, to simulate the configuration of secondary collimators.

The design of the irradiation campaign is presented together with the thermo-mechanical simulations to determine the irradiation temperature. The materials are irradiated at different particle fluences, and the corresponding displacement per atom (dpa) is presented. Each material is irradiated at four or six different levels of dpa, to assess the degradation properties as the irradiation proceed.

The experimental part focuses on the measurement of the electrical resistivity relying on the four-probes method. Multiple-layer resistances models are applied to take into account the small penetration of ions. Microscopic investigations are carried out with Raman spectroscopy for graphitic materials, and with FIB-SEM for coatings. The aim of the microstructural analysis is to explain the different behavior of materials under irradiation, and to correlate the changes observed in the electrical resistivity with the microscopic evolution.

A comparison between the different materials tested is carried out to understand

possible improvements in view of future upgrades of the collimation system. The results presented are then discussed to evaluate the impact on collimators performance and possible mitigation actions.

Acknowledgements

I would like to thank my CERN supervisor Alessandro Bertarelli and Prof. Marco Beghi for the possibility they gave me to advance this PhD program.

I warmly thank Stefano Redaelli for the interest and the support shown in my work.

I would like to thank Marilena Tomut for sharing with me her experience about ion irradiation and Anton Lechner for helping me with all the physics behind radiation damage.

A special thanks goes to my CERN colleagues that contributed to this work. In particular, I thank Anité Perez and Adrienn Baris for the operation of the FIB-SEM microscope, Oscar Sacristan and Jorge Guardia for the setting up of the electrical resistivity apparatus, Andreas Waets for the FLUKA simulations, and Federico Carra for all the useful suggestions. I would also like to thank Valeria Russo, who guided me in the realization and analysis of the Raman tests in Politecnico di Milano.

The research leading to these results has received funding from the European Union's Horizon 2020 Research and Innovation programme under Grant Agreement n. 730871. The research presented here is a result of a RD project experiment UMAT at the M-Branch, UNILAC beam line in the frame of FAIR Phase-0 supported by the GSI Helmholtzzentrum fuer Schwerionenforschung in Darmstadt (Germany). Research supported by the High Luminosity LHC project.

Contents

List of Figures

List of Tables

Introduction and motivations

High-power and high-energy accelerators rely on different advanced technologies. Among them, the role of beam-intercepting devices (BIDs) is fundamental to control the beam and for safety aspects. The materials of BIDs are thus exposed to severe radiation fields, which can deteriorate their thermo-physical and mechanical properties and jeopardise the equipment performance.

This thesis focuses, in particular, on the materials employed in the upgraded collimation system of the High-Luminosity Large Hadron Collider (HL-LHC) at CERN. During the HL-LHC operation the beam-stored energy can reach up to 700 MJ, becoming potentially destructive for BIDs.

Twelve of the new HL-LHC collimators are equipped with a new composite material, the molybdenum-carbide graphite (MoGr). This material has a lower electrical resistivity compared to the presently installed carbon-fibre-carbon (CFC), which allows reducing the impedance budget of the collimation system. The development and characterization of this new composite has been carried out in dedicated R&D programs such as EuCARD, EuCARD2 [1] and ARIES [2].

On top of this, eight out of twelve of these collimators (e.g. secondary collimators) are equipped with MoGr blocks coated with a thin molybdenum layer, which further decreases the electrical resistivity. Besides the thermo-mechanical, electrical, and Ultra-High Vacuum (UHV) characterization, it is fundamental to predict the evolution of these materials under irradiation.

The first step towards the prediction of the collimator performance degradation is the calculation of the radiation damage levels expected at the end of the HL-LHC era. Monte-Carlo based codes are used to support these studies, and especially to calculate the expected displacement per atom (dpa) and gas production induced in the materials. The unique radiation field on the HL-LHC cannot be replicated, but alternative irradiation facilities are considered to reach similar dpa as in HL-LHC collimators.

In this thesis, the possibility of using ion irradiation to mimic the effect of high-energy proton is investigated. The results presented here are obtained after irradiation with Ca ions with 4.8 MeV/u at the M-Branch of the UNILAC accelerator at GSI. The advantages of using ions are numerous: the radiation-induced activation of the irradiated samples is limited compared to protons, and the post-irradiation examination does not require the long waiting time envisaged with proton campaigns as well as the adoption of hot cells. On the top of this, the higher stopping power of ions allows a faster dpa accumulation. The immediate drawback is the small penetration of ions in the material, which must be considered during the post-irradiation examination. The irradiation conditions reached during this experimental campaign are analysed and compared to the radiation environment of the HL-LHC to try to

understand the consequences on the collimator operations. The evolution of properties is notably analysed in terms of dpa, which allows quantifying the damage induced by different particles and different energies. The high dpa rate reached with ions allows reaching a dpa in the coating equal to the one expected at the end of the HL-LHC era. It is however worth noticing that important phenomena such as the production of gas by nuclear reactions are not induced by ions with energies up to tens of MeV per nucleon (MeV/u).

The aim of this work is to characterize especially the radiation damage to a novel grade of MoGr, whose thermo-physical and UHV properties have been optimized for the installation in the novel HL-LHC collimators. Other graphite-based materials are simultaneously irradiated to assess the impact of the production routes and of the initial material state on the radiation resistance. Besides graphitic composite, this work also focuses on the evolution of thin metallic films deposited with sputtering onto graphitic substrate.

The focus is placed on the measurement of the electrical resistivity of both graphitic materials and metallic films, this property being fundamental for the operation of collimators. The evolution of electrical resistivity is analysed and compared to microscopic changes, to understand the interaction of the radiation-induced defects with the pre-existing microstructure.

The thesis is structured as described below. The first two chapters serve to give a background on the relevant concepts for this work: radiation damage and the object of the thesis, the HL-LHC collimation system. **Chapter 1** provides an introduction to the relevant concepts of radiation-matter interaction, and, in particular, it focuses on the mechanism behind the radiation damage in inorganic materials. The influence of the irradiation conditions on the microscopic and macroscopic changes of materials is highlighted. **Chapter 2** is dedicated to the presentation of the LHC collimation system, and on the challenges required by its upgrade, the HL-LHC.

Chapter 3 provides an overview of the radiation level in the accelerator and it summarizes the previous irradiation campaigns for collimator materials to focus then on the design of the irradiation test presented in this thesis.

The experimental methods adopted to characterize the materials are then presented in **Chapter 4**. The material characterization before irradiation are shown in **Chapter 5**, and after irradiation in **Chapter 6**.

The results are then discussed in **Chapter 7**, with the main focus on the correlation of the radiation damage with the initial material microstructure and the impact on the collimation system is highlighted.

The conclusion and the future work are then discussed in **Chapter 8**.

Chapter 1

Introduction to radiation effects on matter

This chapter provides an introduction to the concepts of radiation-matter interaction relevant for the thesis. The focus is placed on the radiation-induced damage mechanisms on inorganic crystalline materials. The degradation of materials under irradiation is discussed under different points of views, starting from the microscopic changes induced in the lattice. The evolution of the damage is then followed up to a macroscopic level to understand the degradation of the thermo-physical and structural properties that can affect the lifetime of critical components.

1.1 Interaction of radiation with matter

The interaction of radiation with matter has drawn much attention from different technological fields: it finds application in nuclear medicine, radiation detection for high-energy physics experiments and radioprotection devices. In material science, different analysis techniques exploit the response of materials to a particle beam to study their morphological, crystallographic or chemical properties. On top of that, ion beams are widely used in surface engineering and nanotechnology to tailor material characteristics. Besides this extensive use of radiation, it has been long recognized that the interaction of particles with matter induces important changes in the materials that can lead to failure of components. This thesis focuses on the detrimental effects of radiation on matter, this being a topic of interest for all the equipment operating in an environment exposed to radiation, such as fusion and fission reactors, but also for aerospace applications and in particle accelerators [3–5].

When a particle interacts with matter, it loses energy via different mechanisms, depending on its charge, mass, and energy. Charged particles such as electrons, protons, alpha, or heavier ions lose most of their energy by *Coulomb interaction* with the atomic electrons. This type of radiation is called directly ionizing because it can induce an atomic excitation or ionization, depending on the energy transferred to the electrons and the electronic properties of the atom. The energy loss per unit length, or *electronic stopping power*, increases as a function of the particle charge, the density and the atomic number of the target material. Additionally, lighter particles, such as electrons, lose a significant part of their energy when their trajectory is

deviated by an electric field. This mechanism causes the so-called *Bremsstrahlung* and the *radiative energy losses* can significantly contribute to the deceleration of the incoming particle. At lower energy, charged particles can also be elastically scattered by the nucleus, inducing its recoil. This mechanism is called *nuclear energy loss* or *non-ionizing energy loss* (NIEL). In some cases, the interaction of high energy charged particles can result in a nuclear reaction that causes the transformation of at least one of the internal states of the nuclides involved [6].

Radiation induced by neutral particles, such as gamma rays and neutrons, is called indirectly ionizing radiation because their first interaction with matter produces secondary particles that are the main origin of the subsequent ionization. Neutrons, which are not subjected to Coulomb interaction, directly interact with nuclei. They can be scattered elastically or inelastically, leaving the nuclei in an excited state. Depending on their energies, neutrons can also induce different nuclear reactions in the material, whose products can be a source of ionizing radiation. Photons interacts mainly with atomic electrons though coherent or Compton scattering, photoelectric effect, electron-positron pair production. The dominant effect depends on the photon energy and the target atomic number. At higher energies they can also induce photonuclear reaction [7, 8].

In Tab. 1.1, the main mechanisms of interaction and their effects on the matter are presented.

Particle	Interaction Mechanism	Outcome
Charged particles	Coulomb interaction e^-	Ionization/Excitation
	Coulomb interaction nuclei	Atom recoil
	Bremsstrahlung	Photon emission
	Nuclear reactions	Secondary particles production/Transmutation
Neutrons	Elastic scattering	Atom recoil
	Inelastic scattering	Secondary particles production
Photons	Coherent scattering	Photon scattering
	Photoelectric effect	e^+ emission + atomic relaxation
	Compton scattering	Photon scattering + atomic relaxation
	Pair production	e^+/e^- production

Table 1.1: Interaction mechanisms and effects of different particles. Modified from [9].

In high-energy particle physics, the aforementioned processes are usually coupled: some events can in fact generate secondary particles, which interact with the surrounding matter to activate a cascade process. A relevant example is the so-called *electromagnetic shower*. High-energy electrons losing energy by Bremsstrahlung or high-energy photon-induced pair production can indeed generate secondary particles in cascade. The *hadronic shower* is instead induced by high energy hadrons which undergo nuclear reaction and produce several particles with enough energy to give rise to a multiplication process. Some secondary particles can also further induce an electromagnetic shower [10].

As a result of the aforementioned processes, the material can be significantly damaged. It is important to distinguish the deterioration of material properties

related to changes of the lattice structure induced by particles, the so-called radiation damage, from the effect related to the heating of the material, which can give rise to high deformation or thermal-shock phenomena [11]. In addition, it is worth noticing that as a result of a nuclear reaction, stable nuclei can become radioactive, and alien chemical species are introduced. The activation of components has to be taken into account to understand the proper handling and analysis of components [12, 13].

1.2 Primary radiation damage

The radiation effect on matter is not merely a function of the incoming particle, but it is strongly affected by the nature of the intercepting material. In organic materials, the damage is related to the ionizing energy losses. The extracted electron is, in fact, hardly replaced, and this causes breaking of chemical bonds. The damage depends on the total dose received by the material, i.e. on the energy per unit mass deposited by ionizing radiation [14–16].

In metals and ceramics, the lattice of a crystalline structure can be significantly changed by radiation by means of two mechanisms:

- impurity production
- displacement of an atom from its ideal position

Nuclear reactions can create nuclei with a different atomic number in the irradiated material. The transmuted nuclei cannot perfectly fit in the regular lattice and they induce a distortion in its surroundings, thus they are considered as impurities. On the top of this, nuclear reactions can also give rise to gas particles (He and H nuclei). Being an insoluble gas, He tends to accumulate and precipitate into nanoscale He bubbles. Finally, during ion irradiation, the particles are stopped inside the medium and they stay there as impurities. The transmuted nuclei produced by nuclear reactions, and in particular the gas species, contribute to radiation damage, and they also interact with the lattice defects induced by the displacement of atoms [13].

1.2.1 Displacement cascade

The scattering of an incoming particle with a nucleus induces a recoil that can displace the atom from its position in the lattice. For charged particles, this is mediated by the Coulomb force and is therefore related to the nuclear stopping power or NIEL. For neutrons, it is driven by the strong nuclear force. When a particle collides with a nucleus, it transfers part of its energy to the atom; if this energy is higher than the displacement energy E_d of the atom, it will be ejected from its lattice site, leaving a vacancy behind. This atom is called *primary knock-out atom* (PKA) and provided it has enough energy, it can displace further atoms, inducing a collision cascade. When the projectile's energy goes below E_d, the particle eventually comes at rest in the lattice as interstitial. As a result, the lattice is characterized by a number of *Frenkel pairs*, that is a pair of point defects, a vacancy and an interstitial [17, 18].

An overview of the primary damage mechanism is given in Fig. 1.1

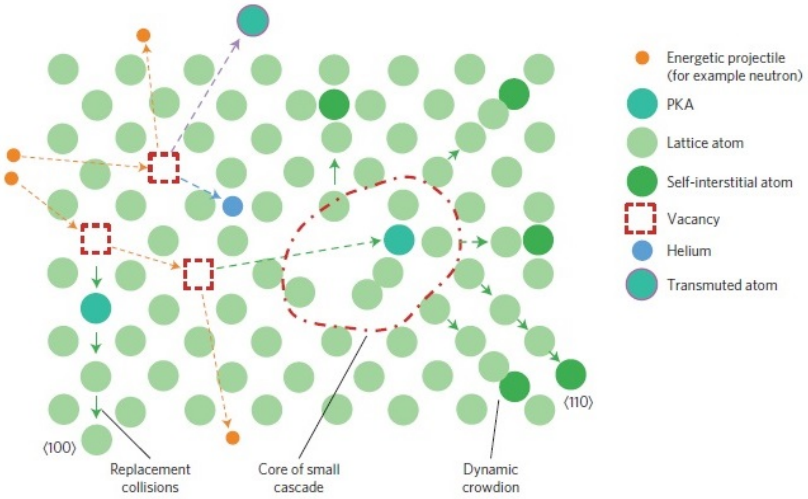

Figure 1.1: Primary damage induced by incoming particles [19].

In literature, it is widely recognized that the correct theoretical model to calculate the number of Frenkel pairs N_F induced by a PKA with energy T is the *Norgett, Robinson and Torrens* (NRT) model [20], according to Eq. 1.1.

$$N_F = \kappa \frac{\xi(T)\, T}{2E_d} \tag{1.1}$$

where $\xi(T)$ is the Lindhard partition function that represents the fraction of energy available for a nuclear displacement. The displaced atoms can indeed lose energy also by means of electronic losses, which do not feed the collision cascade. The term κ is the displacement efficiency and takes into account a more realistic potential to describe the scattering (other then the hard sphere potential). The term $2E_d$ comes from the assumption that the energy is equally split between the two colliding atoms, according to the hard sphere model.

A useful quantity to characterize the displacement damage induced under different irradiation conditions is the *displacement per atom* (dpa). It represents how often an atom is displaced on average during the irradiation and it can be calculated according to Eq. 1.2 [13].

$$dpa = \int \sigma_{disp}(E) \frac{d\phi(E)}{dE}\, dE \tag{1.2}$$

In this equation, E is the energy of the incoming particle and $\phi(E)$ is the energy-dependent particle fluence. The *displacement cross-section* $\sigma_{disp}(E)$ depends on the *damage cross-section* $\sigma_{damage}(E,T)$, which represents the probability of creating a PKA of energy T, and on the number of atoms displaced by that PKA N_F, as shown in Eq. 1.3.

$$\sigma_{disp}(E) = \int \sigma_{damage}(E,T)\, N_F(T)\, dT \tag{1.3}$$

The dpa is a widely diffused parameter in nuclear physics to quantify radiation damage because it allows a direct comparison between different irradiation condi-

tions. The displacement cross section is in fact related to the recoil spectrum of the atoms, which depends on the incoming particle energy and type [21]. The displacement cross-section is higher for heavy particles, with higher nuclear stopping power, and a higher dpa is reached in a short time. As example, in Fig. 1.2 the displacement cross section for different particles on carbon target is shown.

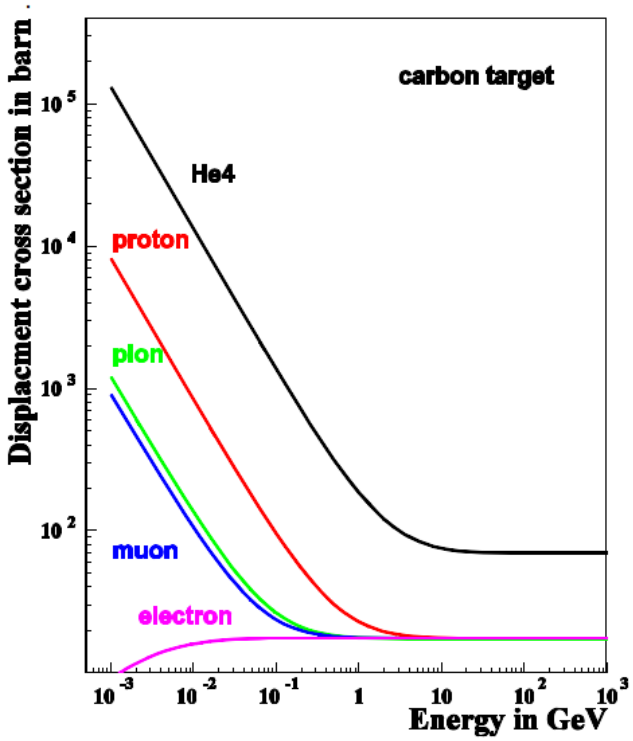

Figure 1.2: Displacement cross-section as a function of the beam energy for different particles [12].

The dpa can be calculated with Monte-Carlo codes such as FLUKA [22, 23] or MARS [24]. In these codes, different physical models are included to calculate the damage cross-section, that combined with the NRT model give the dpa [12, 25].

The dpa is therefore representative of the displacement cascade, which starts with the interaction of the particle with a lattice atom and concludes when all the knock-out atoms come at rest. This collision phase is very fast, it typically lasts 10^{-13}–10^{-12} s; at its end, the lattice is characterized by a supersaturated solution of Frenkel pairs. This configuration is unstable and further evolves towards equilibrium in successive steps.

1.2.2 Thermal spike

At the end of the collision phase, the atomic configuration is unstable, because of the strongly distorted lattice. In a second phase, which lasts 10^{-12}–10^{-11} s, a thermodynamic recrystallization of the material occurs, which leads to a spontaneous athermal recombination of the point defects that are separated by small distances (typically few lattice distances). This phase is called *thermal spike*, because the

average energy of atoms corresponds to 10^4 K. The amount of surviving defects decreases with the increase of the PKA energy, which produces a higher concentration of defects. This is not taken into account by NRT which is therefore overestimating the dpa. In a very dense cascade, the distance between defects is reduced, and they can easily migrate and coalescence to reach a more stable configuration [26–28].

1.3 Microscopic evolution of radiation damage

After the thermal spike, the configuration of the lattice is still unstable, and a further evolution is therefore expected. On a longer timescale, the thermally activated diffusion process becomes important. A summary of the different stages of radiation damage evolution is given in Tab. 1.2.

Phase	Timescale	Effect
Collision cascade	10^{-13}-10^{-12} s	Creation of PKAs
Thermal spike	10^{-12}-10^{-11} s	Athermal recombination of in-cascade point defects and clustering
Defects diffusion	10^{-8} s	Recombination at sinks or grain boundaries, large clustering

Table 1.2: Timescale and description of the radiation damage evolution and of the representative events.

From a macroscopic point of view, the diffusion is described by *Fick's laws*. In these equations, the flux J of the diffusing species is related to the concentration C through the diffusion coefficient D, as shown in Eq. 1.4a, 1.4b.

$$J = -D\,\nabla C \tag{1.4a}$$

$$\frac{\partial C}{\partial t} = -\nabla \cdot J \tag{1.4b}$$

The diffusion coefficient D can be generally written as a constant term D_0 multiplied by a temperature-dependent exponential, which contains the *activation energy* Q and the Boltzmann constant k, as shown in Eq. 1.5.

$$D = D_0 \exp\left(\frac{-Q}{kT}\right) \tag{1.5}$$

The activation energy for diffusion depends on the type of defects and on the crystal lattice, but also on diffusion mechanisms. Interstitial defects, for example, are mobile at lower temperature with respect to vacancies. This characteristic is fundamental for the evolution of radiation damage [18].

During diffusion, in fact, radiation-induced defects interact between themselves and with the pre-existing lattice. In particular, we can distinguish three main processes:

- Annihilation of a vacancy with an interstitial

- Clustering of interstitial or vacancies
- Capture of point defects at dislocations, grain boundaries, and voids

As a result of the aforementioned process, the final microstructure of an irradiated crystal can be very different with respect to the primary damage made of isolated Frenkel pairs or small defect clusters [26, 27, 29–32]. At the end of irradiation, different types of defects are present:

- Surviving point defects (vacancies, interstitials, impurity, point defect clusters)
- Line defects (dislocations)
- Planar defects (grain boundaries, interphase boundaries, twin boundaries, domain boundaries, stacking faults)
- Volume defects (voids, bubbles, precipitates, cracks)

An overview of the different radiation-induced defect clusters is provided in Fig. 1.3

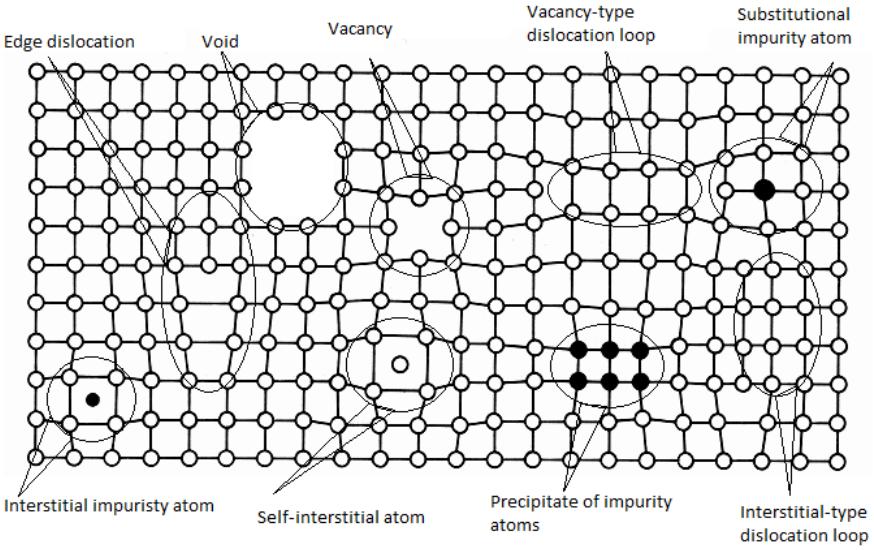

Figure 1.3: Schematic of different defect configurations after irradiation. Modified from [13].

Dislocations are particularly relevant for understanding the evolution of microscopic but also macroscopic radiation damage. These defects are present already before irradiation, but they are not equilibrium defects. Dislocation lines are defined as a boundary between a slipped and a fix region of crystal. As a consequence, dislocations are characterized by a distortion of the lattice around them. In Fig. 1.4, edge and screw dislocations are shown. The classification is based on the slipping direction with respect to the dislocation line: perpendicular for edge dislocation, parallel for the screw one. Generally, real dislocation are mixed, containing different sections characterized by either edge or screw behavior and they are present as closed loops inside the crystal [33]. During irradiation, interstitials and vacancies cluster to form dislocation loop. Point defects can also diffuse to dislocations and be

(a) Edge dislocation

(b) Screw dislocation

Figure 1.4: Schematics of dislocation geometries [33].

absorbed there. As a results, dislocations move with a mechanism known as climb and they also act as point defects sink.

The oversaturation of vacancy-like defects can also lead to the formation of 3D defects. Void clusters grow during irradiation by absorbing vacancies. Transmutation gases can also be absorbed by void and, as a results, they increase the stability of the cavity.

1.3.1 Review of experimental parameters influencing radiation damage

The multiplicity of radiation-induced defects clusters, their distribution and evolution are important to determine the effect of radiation on the properties of the material. Therefore, even if we can initially quantify the radiation damage with the dpa, this parameter alone fails to capture certain properties of the damage. When comparing different irradiation conditions, it is therefore important to consider not only the dpa, but also other parameters that influence the damage. At the same time, the pre-existing characteristics of the irradiated material affect the radiation-induced effects.

Irradiation temperature

Diffusion is the key process due to which defects interact, determining an evolution of the microstructure. Both, the activation and the intensity of the diffusion process depend on the temperature, which thus becomes a key parameter to monitor during irradiation. The energy needed to activate diffusion depends mainly on the defect geometry: point defects are put in motion at lower temperature. The different recovery stages, corresponding to the activation of diffusion for different defects, can be identified with post-irradiation annealing experiments. During these tests, the variation of a property which is influenced by the defect concentration is measured after irradiation at very low temperature and after thermal treatments at different temperature. It is generally accepted that five main irradiation temperature regimes exist [28, 32]:

- $T < Stage\ 1$: all the defects are immobile, defects concentration increases linearly with dpa until primary damage defects overlap and annihilate

- *Stage* $1 < T <$ *Stage* 3: Self-interstitial atoms (SIA) and small SIA clusters are mobile and they can diffuse to form dislocation loops or combine with vacancies.

- *Stage* $3 < T <$ *Stage* 5: both SIAs and vacancies are mobile, different defects nucleation are possible.

- $T >$ *Stage* 5: vacancies aggregates in 3D voids and swelling is observed.

- $T >>$ *Stage* 5: He cavities nucleation (if transmutation gas is present)

These stages are generally related to the melting temperature of the irradiated material and their activation occurs generally at lower temperatures for metals compared to ceramics. In copper, a recover of electrical conductivity is observed at a temperature as low as 20 K [32], while in graphite it is not detected before 150 K [34]. Post-irradiation annealing is also influenced by the irradiated temperature, which determines the structure of defects. From a practical point of view, it is important to understand the minimum temperature to annihilate the damage and the maximum to achieve a complete recovery, as a function of the material properties and the irradiating conditions [35].

PKA energy

The distribution of the primary recoiling atom energy depends on the energy, charge and mass of the incoming beam. Heavier ions induce higher recoil energy compared to light ions. The PKA energy, however, also depends on the potential describing the interaction between particles; this results in a higher average recoil energy for neutrons compared to ions [36].

An energetic cascade typically leads to direct clustering and recombination of point defects, whereas a low energy PKA induces isolated Frenkel pairs [29]. In Fig. 1.5, for example, electron irradiation induces a flux of point defects that lead to dislocation loop formation, while in the fission the energetic neutrons cascade in small nucleation loops that nucleate and act as sinks preventing growth of bigger loop [32].

Dose rate

The evolution of radiation damage depends on different competitive mechanisms such as in-cascade clustering or annihilation at sinks of defects. These processes are influenced by the rate at which defects are introduced in the crystal, namely by the dose or dpa rate. The macroscopic effect and thus the degradation of thermophysical and mechanical properties can be therefore different for the a material irradiated at the same dpa, but with different dpa rates.

The critical dose (dpa) to induce complete amorphization in silicon carbide crystal is, for example, decreasing as the dose rate (dpa rate) is increasing [32]. This effect is, however, strongly coupled to temperature, and the respective correlation should be addressed separately [37]. The dose rate effects are generally more visible at elevated temperature [32], where the role of diffusion is relevant for the final defect distribution.

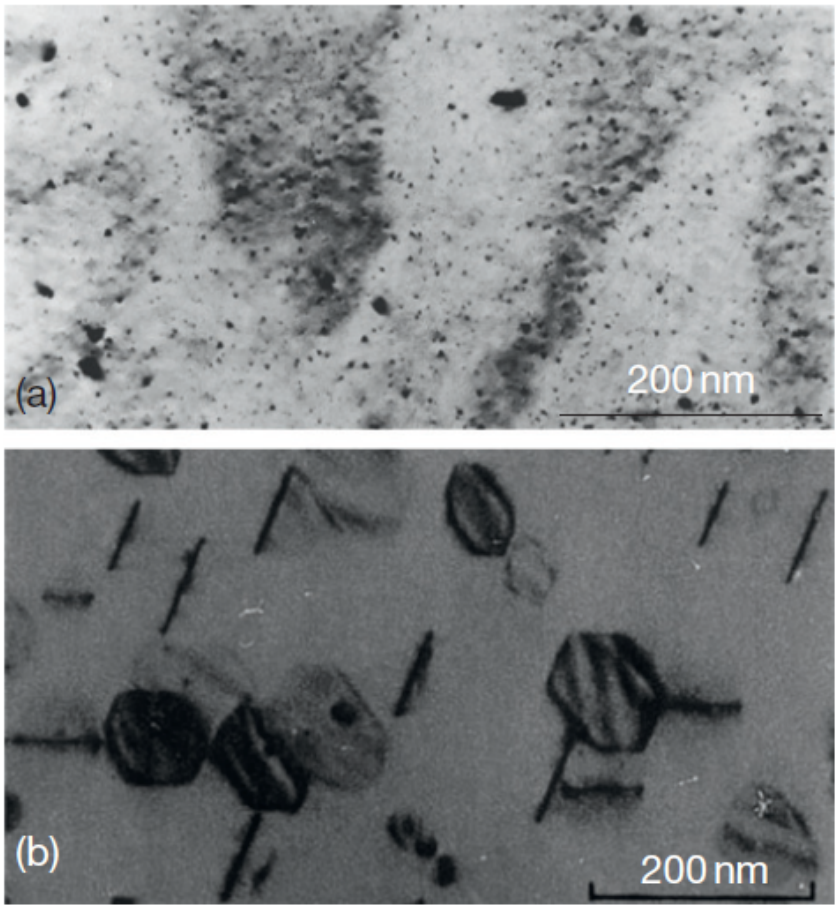

Figure 1.5: Micrographs of copper irradiated with fission neutrons (top) and 1 MeV electrons. The defect clusters in the high energy cascade induced by neutrons act as a sink and they prevent bigger loops from nucleating [32].

Transmutation gases

Transmutation gases as H or He are important because they can stabilize 3D vacancy voids and migrate to grain boundaries, contributing to failure. The interaction of these products with defects can modify the recombination and diffusion of the defects. It is therefore important to take into account such effects simultaneously. For this reason, a useful parameter to be evaluated during irradiation is the ratio between dpa and atomic parts per million (appm) of He and/or H. In Tab. 1.3 , the typical value of dpa/appm is presented for different irradiation environments [38]. Also in this case, the effect depends on the correlation of this mechanism with the ones induced by temperature and dpa rates.

Ionizing radiation

The radiation damage mechanisms presented in Sec. 1.2 and Sec. 1.3 are ascribed to NIEL losses of charged particles or to elastic scattering of neutrons. Although ionizing radiation is a serious concern mostly for organic components and insulators, also metals, semiconductors, and conductive ceramics might be affected. Depending

Irradiation source	dpa rate [dpa/s]	He gas production [appm/dpa]	Irradiation T [°C]
Fission reactor	$3 \cdot 10^{-7}$	0.1	200-600
Fusion reactor	$1 \cdot 10^{-6}$	10	400-1000
High-energy proton beam (accelerators)	$6 \cdot 10^{-3}$	100	100-800

Table 1.3: Comparison of typical dpa and gas production obtained under different irradiation environments [38].

on the material, *ion tracks* are detected above a certain electronic stopping power. Ion tracks are cylindrical regions characterized by ionized matter. The ionization is induced directly by the incoming ions or by secondary electrons (delta-rays) [37]. The positive ion repulsion along the track cause a lattice distortion, but it also influences the diffusion of point defects produced with nuclear losses [32, 39, 40]. The relative importance of ionization and displacement damage also depends on irradiating beam. Electrons and light ions are characterized by an higher ionization to dpa ratio compared to neutrons and heavy ions [32].

Initial lattice structure

Pre-existing grain boundaries and defects act as sinks for irradiation-induced defects. The annihilation of defects at sinks is therefore a competitive process and it depends on the sink concentration in the material [18]. For this reason, a material with a higher initial lattice disorder can be less affected by radiation given its capability of removing the defects from the lattice.

On top of this, it is reported that also the packing arrangement of crystals can influence the defect evolution: the anisotropy of hexagonal close-packed (hcp) crystals can indeed inhibit the migration and hence the recombination of defects [32].

Atomic weight and density

The effect of the atomic weight of the irradiated material is related to the higher nuclear and electronic stopping power characterizing heavy targets. For this reason, the higher energy and the higher density of the cascade can enhance the point defects clustering. In a similar way, a higher mass density induces a more compact displacement cascade.

Energy of formation and activation motion of defects

The nature of the crystal irradiated determines also the formation of defects, and in particular the displacement energy E_d depends on the material, and the energy needed to activate diffusion. The first parameter, E_d, is taken into account by the dpa, while the further evolution of the microstructure should consider also the mobility of defects in a lattice.

1.4 Macroscopic evolution of radiation damage

The radiation-induced defects and the associated evolution of the microstructure affect in turn the macroscopic properties of the irradiated material. Some mechanisms are common to all the materials, while some are typical of a specific structure. In the following sections, changes of some fundamental properties of material are discussed.

1.4.1 Electrical and thermal conductivity

Electrical and thermal conductivity are transport properties that define the transport of electrical charge and heat inside a crystal out of the equilibrium state. From a macroscopic point of view, electric and heat transports can be described by the Ohm and Fourier laws. For crystals, we can generalize these laws to include the tensorial form of the conductivity terms, as shown in Eq. 1.6 and Eq. 1.7.

$$j_i = \sum_{l=1}^{3} \sigma_{il} \, E_l \tag{1.6}$$

$$q_{th,i} = -\sum_{l=1}^{3} k_{il}^{th} \frac{\partial T}{\partial x_l} \tag{1.7}$$

Where j is the charge current density, σ is the electrical conductivity, E the electric field inducing the transport, q_{th} is the heat current density, $\frac{\partial T}{\partial x_l}$ is the thermal gradient inducing the transport, and k^{th} is the thermal conductivity.

In order to understand the effect of radiation, the microscopic interpretation of these quantities must be analysed. The charge carriers are the electrons, therefore the electrical conductivity depends on their mobility. The electron path is slowed down by scattering processes inside the crystal. The main responsibles for electron scattering are lattice vibrations, impurities and lattice defects [41]. According to Matthiessen's rule, by decomposing the contribution of the different sources of electron scattering, the electrical resistivity ρ, the inverse of the electrical conductivity, can be written as a sum of the contributions due to the different scattering processes, as shown in Eq. 1.8.

$$\rho = \rho_{phonons} + \rho_{impurities} + \rho_{defects} \tag{1.8}$$

Similar considerations apply for heat conduction, though in this case it is important to distinguish between metals, where heat carriers are essentially electrons, from non-metals where the heat conduction is dominated by lattice vibrations. In both cases, scattering due to lattice defects decreases their mobility, inducing a reduction of thermal conductivity.

During irradiation, different defects are created as explained in 1.3 inducing an increase of the scattering of carriers and reducing therefore their mobility.

It is important to notice that the effect of irradiation on the transport properties depends on the surviving defects: the athermal and thermal recombination of defects during irradiation are therefore contributing to reduce the effective damage. As a

consequence, the effect in metals is much lower because of the higher mobility of defects already at relatively low temperature [42].

Graphitic materials are more sensitive to irradiation. In particular, many studies are available from neutron irradiation, given the extensive use of graphite as neutron moderator in fission reactors. The degradation of thermal conductivity as a function of dpa is reported in literature, showing relevant effects already at 0.001 dpa [43]. Higher irradiation temperature mitigates the property changes thanks to a higher mobility of defects that enhances annihilation [43–46]. The variation of thermal conductivity is also related to the material morphology; in particular, a higher degradation is observed in carbon-fibre composites compared to fine grained graphite [46]. On top of this, a higher initial value of conductivity is associated to a faster degradation during irradiation [34, 43, 47]. The same effect is observed for electrical conductivity: the decrease of this property during irradiation is more pronounced for materials having a higher initial conductivity. This phenomenon is related to the interaction of radiation-induced defects with the pre-existing microstructure. Grain boundaries and porosities are responsible for a lower initial conductivity. During irradiation, they can mitigate the decrease of conduction induced by defects by accommodating them [48, 49].

Some tests conducted with heavy ions indicate that the degradation induced in graphite is higher compared to neutron irradiation, but the beneficial effect of higher irradiation temperature is confirmed [50, 51].

It is worth noticing that point defects have a different impact on the transport properties. In particular, perpendicularly to the graphite basal plane, the cluster defects have a higher impact [52]. The evolution of the microstructure is therefore fundamental to determine the final effects of radiation.

1.4.2 Dimensional instabilities

The effects of radiation damage on the dimensional stability of material are several and related to different phenomena. It is fundamental to understand how to prevent these phenomena in the design of structural components or where high geometrical tolerances are required. The dimensional changes induced by radiation are classified as growth, creep and swelling, as a function of their effects and the boundary conditions under which they happen [28, 32, 53, 54].

Irradiation-induced growth is an anisotropic change of dimensions and shape that is not accompanied by a volume change. It is commonly observed in low-symmetry crystals. In non-perfectly symmetric crystals there is, in fact, a preferential direction for dislocation loops which can lead to an increase of crystal length in the direction of the loop nucleation. In symmetric crystals, the nucleation is random, and the global effect is null. This effect is mitigated also in polycrystalline materials with random orientation of grains, but it is relevant for highly textured crystals. The irradiation growth is therefore particularly relevant for hcp crystal structures such as Mg, Ti and Zr alloys, widely used in nuclear reactors, but also for graphite that finds application in different fields where radiation is present [55]. In a graphite crystal, interstitial loops develop between basal planes, forming an additional plane between two pre-existing layers. As a consequence, the crystal growths along the c-axis. Conversely, the coalescence of in-plane vacancy leads to shrinkage along the

a-axis. The two mechanisms are represented in Fig. 1.6 [56] .

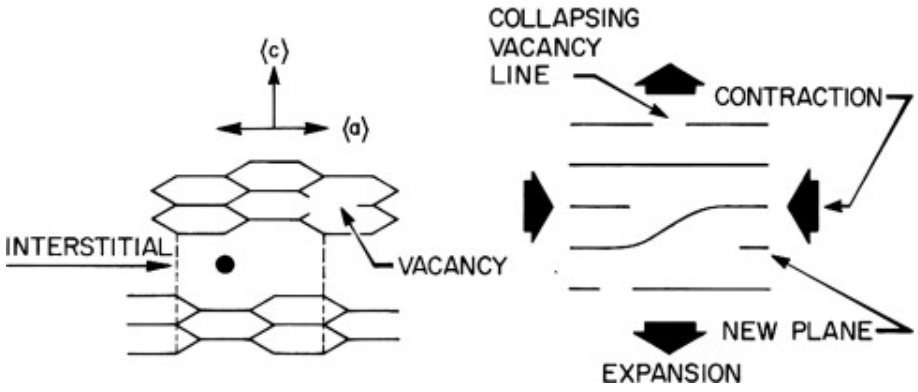

Figure 1.6: Radiation growth in graphite. Accumulation of interstitial dislocation loops between basal planes, and vacancy collapsing along a basal plane [56] .

It is worth noticing that in polycrystalline graphite, porosity can partially accommodate the c-axis expansion.

The random distribution of the directions of dislocations can also be altered by applied stresses that induce a continuous deformation in time, the so-called *irradiation creep*. Creep and growth are dimensional changes characterized by a conservation of the total volume. On the contrary, voids cause an isotropic increase of volume, known as swelling. Although the swelling in hcp material is less relevant compared to fcc or bcc crystals, anisotropic swelling can induce cracks at the grain boundaries.

Under irradiation, it is also important to consider the variation of the coefficient of thermal expansion (CTE) for graphitic materials. The CTE is, in fact, controlled by the pore accommodation capability, which is modified under irradiation. Increase of the thermal expansion coefficient as a consequence of radiation damage is in fact reported for different graphite grades under neutron and proton irradiation [57, 58], but also for some alloys [35].

1.4.3 Mechanical properties

The mechanical properties of crystals are strongly affected by irradiation and in particular by the formation of dislocation-like clusters. Dislocation motion is in fact the mechanism behind plastic deformation. During irradiation, the concentration of dislocations increases and the interaction between two dislocations becomes possible. A possible outcome of this interaction is the creation of a section of dislocations out of the glide plane, that hinders their movement. As a consequence, an increase of the yield stress, the so-called *radiation hardening*, is observed, and the plastic deformability of the material is reduced. A similar effect is also ascribed to voids [28, 32, 53, 54]. This behaviour is usually accompanied by an increase of the elastic modulus, but also by a decrease of the strain to rupture, which causes material embrittlement. For graphite materials, an increase in both, the strength and the elastic modulus, is detected under neutron and proton irradiation. At high dose rates, the contribution of the pore closure to the increase in the elastic modulus must be considered [58, 59].

The structural properties of material under irradiation are greatly affected also by the production of transmutation gases in nuclear reactions. In particular He, which can be produced in different nuclear reactions, is insoluble and precipitates into bubbles. Under tensile stress, He bubbles migrate to grain boundaries and accelerate the intergranular fracture by decreasing the strain to fracture [32, 53].

1.5 Thermal-induced load and shock waves

The previous sections are dedicated to the long-term effects of radiation-matter interaction. The energy deposited in the materials is also leading to material heating. In an inorganic crystal the energy is converted into heat as a consequence of the electron-phonon coupling [16]. The energy deposition map can be calculated with the same multi-purpose codes used for dpa calculations [10].

In particle accelerators, particle beams store a significant amount of energy that can be deposited in the material. The high-energy physics requirements have driven the development of machine with higher energy stored in the beam, as shown in Fig. 1.7.

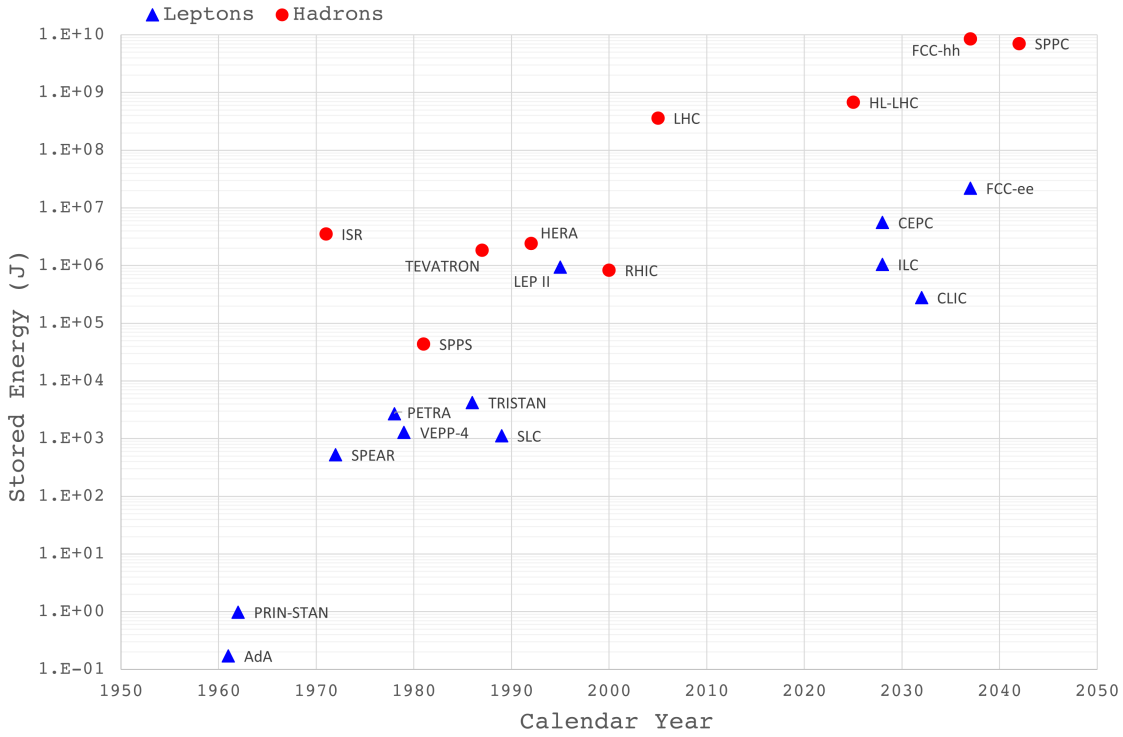

Figure 1.7: Stored energy in present and future particle accelerators [60].

The temperature increase related to the deposited energy induces different thermo-mechanical phenomena in the material, as a function of the space distribution and timescale of the beam energy deposition. Under quasi-static heating, the thermal load rate is low enough to neglect the variation of temperature over time. As a function of the material thermal conductivity, a temperature gradient develops along the body, inducing thermal stresses. Thermal stresses can also arise as a consequence

of inhomogeneities in the body (contact between materials with different CTE) or when free deformation is prevented, as in hyperstatic designs [11].

At higher load rates, temperature variation over time must be considered, but dynamic effect can be neglected. Slow-transient heating scenarios represent what happens to some beam-intercepting devices, named collimators (see Ch. 2), during the normal operation of an accelerators.

One of the most peculiar events related to particle interaction with matter is however related to thermal shock phenomena. In case of accidental scenarios, the particle beam can indeed release its stored energy in a very short time. In this case, the material expansion is prevented by its inertia and the phenomena can lead to the generation of elastic or plastic stress waves. On top of that, the high energy density can induce changes of phase in the material, becoming a liquid, gas or plasma, as shown in an example in Fig. 1.8. The understanding of the dynamic regime is important to predict the integrity or functionality loss of a component.

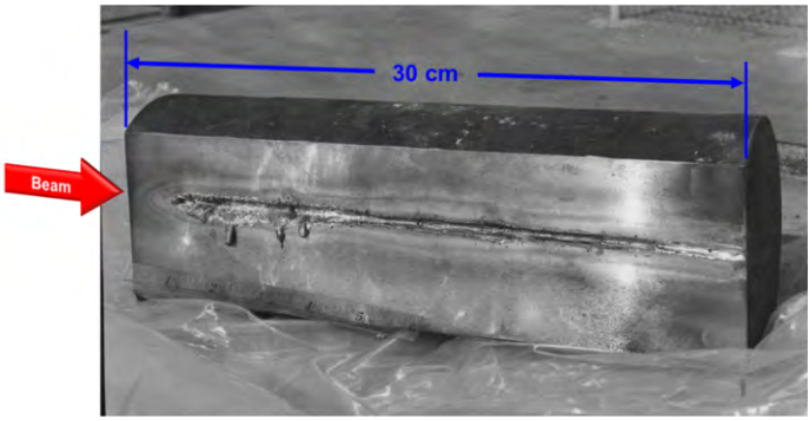

Figure 1.8: Extensive melting of copper block hit by 18 GeV/c electron beam at Stanford Linear Accelerator Center (SLAC) [11]. The picture is in black and white.

The dynamic response of a material depends on the power density deposition and on the duration of the interaction, but it is also deeply related to the thermo-physical and mechanical properties of the target material. The thermo-mechanical response of material under beam impact depends in fact on its properties, which are affected by radiation damage. Radiation damage and thermo-mechanical response of material under beam-induced thermal load are strongly related in particle accelerators.

Chapter 2

Accelerators and Beam-Intercepting Devices (BIDs)

This chapter describes the main field of application of the materials investigated in this work: beam-intercepting devices in accelerators, and collimators in particular. The focus is placed on high-energy and high-intensity accelerators such as the Large Hadron Collider (LHC) and its upgrade, the High-Luminosity LHC (HL-LHC). The state-of-art of the materials applied in collimators is presented together with their requirements, and the need of predicting and mitigating radiation damage is underlined.

2.1 Introduction to accelerator technologies

Modern particle accelerators produce high-energy particles enabling to access incredibly small dimensions. The energy is indeed inversely proportional to the De Broglie wavelength of a particle, allowing to resolve objects with dimensions of the same order of magnitude. At TeV energies, it is possible to detect entities down to 10^{-18} m. The fundamental constituents of our universe have been detected and studied thanks to the high-energy physics (HEP) and put together in the Standard Model theory. At these energies, it is also possible to recreate conditions similar to 1 ps after the Big Bang [61].

The challenges for the design, construction and operation of powerful accelerators cover different technological fields. Among these, it is important to mention at least radio-frequency (RF) cavities for particle acceleration, normal and superconductive magnets for the beam trajectory control, cryogenic systems, and ultra-high vacuum (UHV) systems.

The presence of high-energy particles and intense beam calls for a special attention to potential radiation damage in different accelerator components. The failure of electronic components due to both ionizing and non-ionizing energy losses, for example, is studied [12]. It is also well reported the deterioration of superconducting cable due to beam damage [62]. Besides the aforementioned situations, components at the 'loss points' of accelerators are mostly exposed to energy deposition by particles and hence radiation damage [13]. This thesis focuses on these devices, that are known as beam-intercepting devices (BIDs).

2.2 Beam-intercepting devices (BIDs)

The family of beam-intercepting devices (BIDs) encompasses in a general way components subjected to particle absorption. These devices cover different functions and, as a consequence, a variety of designs and materials are involved in their construction. In particular, these categories are identified:

- Targets. Fixed-target experiments cover a significant part of physics activities involving particle accelerators. The term target indicates a component impacted by the particle beam [63]. As a consequence of the interaction, secondary particles are produced. Opposite to a collider, where two beams in motion hit each others, targets are fixed in the laboratory frame. As a consequence, the centre of mass energy, which is available for new particle production, is lower for fixed target test compared to colliders [64]. These experiments are, however, widely used for some specific applications where the interaction cross-section or the production cross-section are low. Among them, it is worth mentioning the neutron spallation targets (e.g. at J-PARC), muon production targets (e.g. at TRIUMF), antiproton production (e.g. at FNAL) and neutrino factories (e.g. at FNAL, CERN). The target material depends on the specific physic requirements, and it can be, for example, tungsten, lead, carbon or mercury [65].

- Dumps. Beam dumps are also fix targets, but they cover a safety role inside accelerators. When the beam inside the accelerator has to be stopped for whatever reason, it is directed to the dump, where it loses energy by interacting with the absorber material. In a non-collider, the dump is always in use.

- Collimators. These BIDs are dedicated to cleaning and control of the unavoidable beam losses on sensitive equipment during operations, as detailed in 2.3.2. The specific design and requirements are strongly related to the configuration of the accelerator.

- Destructive beam diagnostics. This category encompasses all the instruments that rely on beam-interception in order to monitor one of its properties.

BIDs play a fundamental role for the performances of accelerators, and for this reason their properties degradation under beam damage must be carefully assessed and mitigated.

In this thesis, the focus is on the collimation system of the Large Hadron Collider (LHC) at CERN. So far, the LHC is the most powerful accelerator and the energy stored in the beam reaches an even higher level in its upgrade, the High-Luminosity LHC (HL-LHC). The uniqueness of this accelerator and its collimation system are detailed in the following sections.

2.3 The LHC collimation system

2.3.1 Introduction to the CERN and to the LHC

The European Organisation for Nuclear Research (CERN) is an international laboratory involving 23 member states and several associated members. CERN provides

a unique complex of machines and laboratories to study fundamental physics. Its mission engages scientists from all over the world to push the technological and scientific knowledge for the benefit of society: chemistry, material science, information technology, and hadron therapy for medicine are also investigated.

CERN laboratories are located in Geneva, but they extend around the Swiss-French border. In this area, the LHC machine is operating since 2008.

The LHC is a two-ring accelerator and collider installed in a 27 km tunnel between Switzerland and France. The LHC is fed with two counter-circulating proton or ion beams injected by a chain of linear and circular accelerators, depicted in Fig. 2.1.

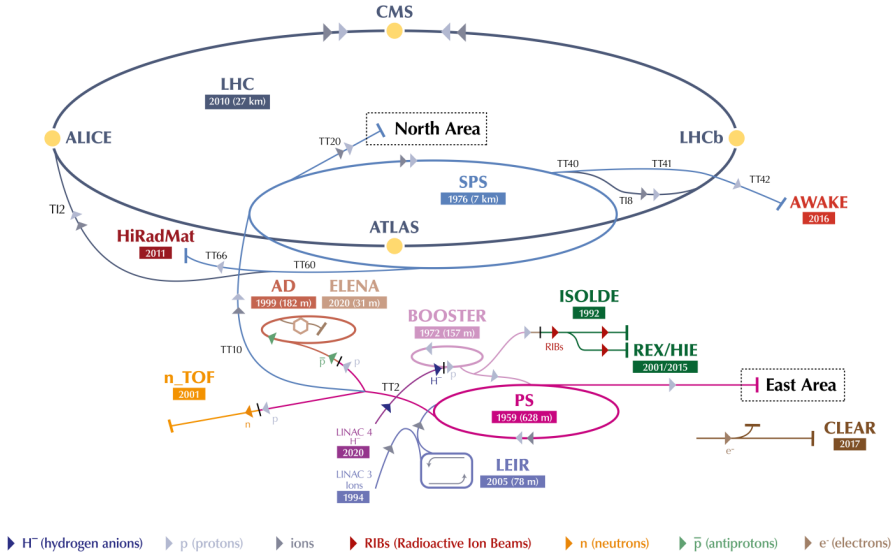

Figure 2.1: The chain of linear and circular machines that accelerates the particle beam until its injection in the LHC.

The energy of the particles is progressively increased up to 7 TeV through the accelerator complex. The beams are not continuous but split into bunches, each composed by almost 10^{11} particles. One LHC beam is generally composed by 2808 bunches. A summary of the nominal proton beam parameters of the LHC is given in Tab. 2.1 [66].

Proton energy	7 TeV
Particles per bunch	$1.15 \cdot 10^{11}$
Bunches per beam	2808
Bunch spacing	25 ns

Table 2.1: Main parameters of the LHC proton beam.

The LHC ring is composed by eight long straight sections (LSS) and eight arcs, as shown in Fig. 2.2. The straight sections are dedicated to different functions:

- The LSS1, LSS2, LSS5 and LSS8 are located at the collision points of the two beams, and they host the four particle detectors ATLAS [67], ALICE [68], CMS [69] and LHCb [70].

- The LSS3 and LSS7 are dedicated to the momentum and betatron cleaning of the beams. Most of the collimators are located in these sections.
- The LSS4 is the insertion region for the radio-frequency (RF) cavities that accelerate the particles.
- The LSS6 contains the LHC dump.

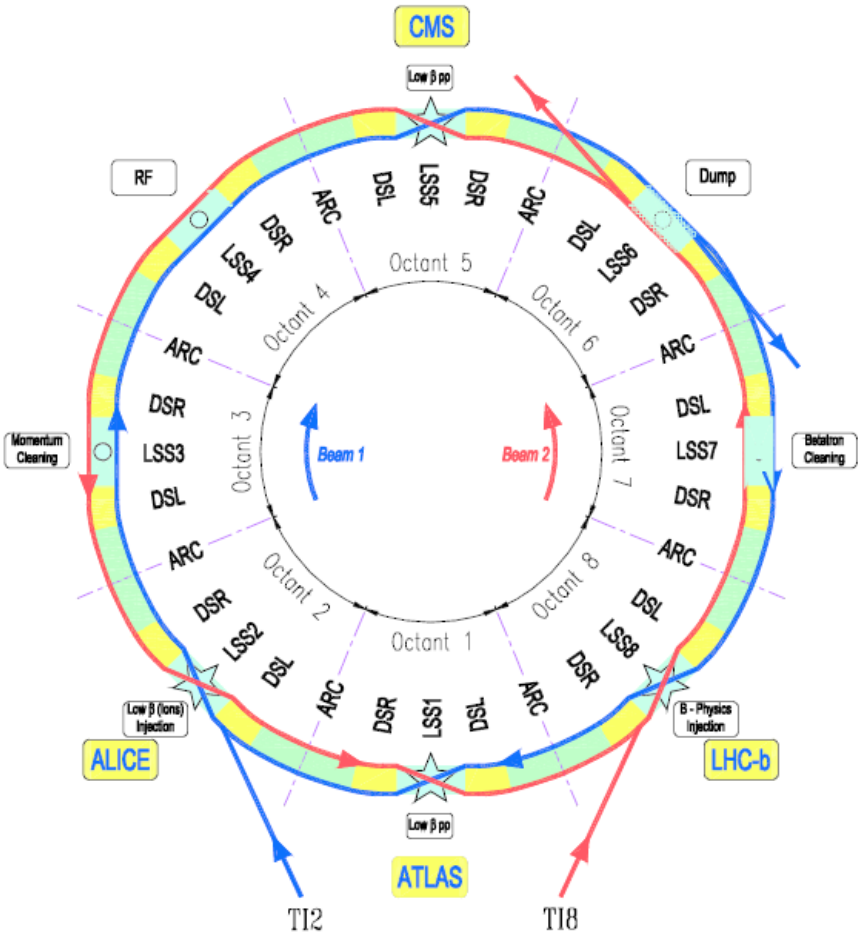

Figure 2.2: Scheme of the LHC ring layout and its main sectors [71].

The arcs are dedicated to the installation of the magnets. Each arc is composed by 23 cells with a regular design defined by a standard half-cell containing three bending magnets (dipole), a focusing magnet (quadrupole), and several multipoles magnets for chromaticity control or dispersion suppression. On the top of these magnets, others are installed along the ring leading to a total of more than 9000 installed [72, 73].

The bending of 7 TeV proton beam demands a magnetic field of 8.33 T within the chosen layout, almost five order of magnitude higher than the earth magnetic field [74]. The use of a superconductive technology is fundamental to reach this field strength. Superconductors show zero resistance to a current flow below a critical temperature T_c; therefore this technology allows overcoming the current density limitation imposed by Joule heating in normal conductor magnets [75]. In the LHC,

NbTi superconducting cables are used, thus requiring an operating temperature of 1.9 K. For this reason, a powerful cryogenic system and distribution line are installed in the LHC tunnel.

If particles interact with the magnets, they deposit energy and cause heating. If the temperature overcomes T_c, there is a sudden transition to the normal conductor state. This situation is potentially dangerous for magnets, because the high flow of current density is converted into Joule power, and temperatures close to melting can be reached [76].

For this reason, in a superconductive machine it is fundamental to engineer an efficient layout and design of collimators, which must intercept the particle losses that would otherwise induce heat deposition in the magnets.

2.3.2 LHC collimation system function and layout

The unprecedented energy stored in the LHC proton beams pushes the complexity of the collimation system design: even a small fraction of this energy would in fact induce a quench in the superconductive magnets, compromising the accelerator operation and potentially damage the magnet. In the LHC, the energy stored by the beam reaches 362 MJ, while the quench limit for magnet is nine orders of magnitude lower [77]. The most stringent design requirement of the LHC collimation system is thus related to this aspect.

Beam losses during operation mainly come from the so-called beam halo, which defines particles with transverse amplitudes or energy deviations significantly larger than those of the reference particles [78]. Betatron halo refers to particles with a transverse emittance higher than nominal, while particles with an energy error belong to the off-momentum halo. If the proton beam is approximated by a perfect Gaussian distribution, the halo is defined as the particles outside of 3σ, where σ characterizes the beam size, as shown in Fig. 2.3. Thus, in a perfect 2D Gaussian beam, about 1.1% of the particles belong to the halo [78]. During normal operation, the number of particle populating the halo increases because of different phenomena: particle-particle collision in the interaction points, collision with residual gases, different beam instabilities or feedback system noise [78, 79]. The halo particles are diffusing towards the external region and they ultimately turn into losses that can hit and deposit energy in magnets or other sensitive equipment. For this reason, solid blocks are placed close to the beam to intercept these particles. The first role of the collimators is therefore to safely intercept and dispose the particles populating the halo during the LHC operation. Thanks to their robustness, these BIDs are efficiently exploited also to scrape the beam and probe the population of the beam halo.

The heat loads absorbed by the collimation system during operation can be estimated by modelling the losses with the beam lifetime η_b. This parameter is defined as the time after which the beam intensity I is reduced to the 37% of the initial value I_0 because of operation losses. In a linear approximation, the loss rate R is inversely proportional to η_b, as shown in Eq. 2.1.

$$R = \frac{dI}{dt} = \frac{I}{\eta_b} \tag{2.1}$$

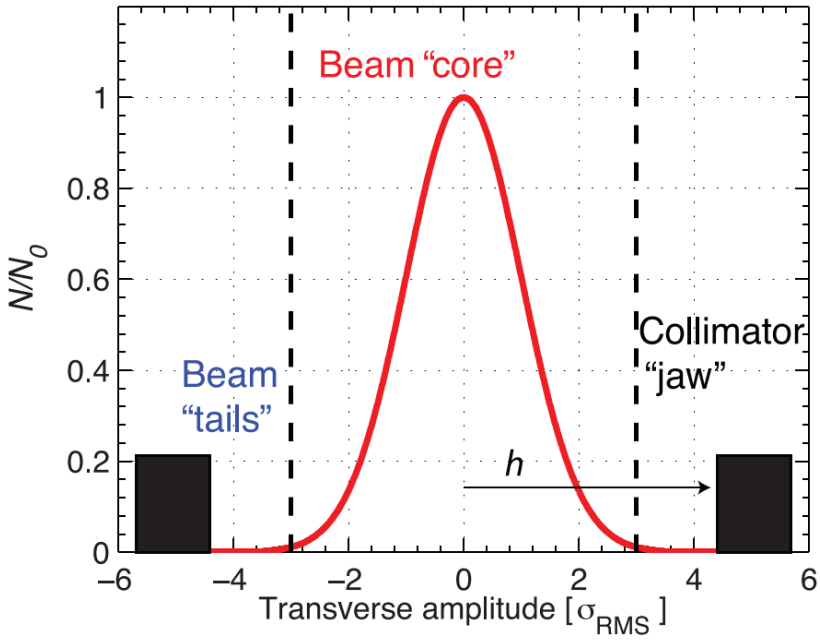

Figure 2.3: Model of the LHC proton beam shape. The corresponding beam core and halo are represented [78].

The beam lifetime is not constant over the LHC operation, and phenomena leading to losses can appear at different moment. The maximum losses are detected for the minimum η_b as shown in Eq. 2.1, $\eta_{b,min}$ is therefore used for collimator design. The scenarios considered are [79, 80]:

- Steady-state losses condition: the beam losses are continuously absorbed at collimators. In this case, the minimum $\eta_{b,min}$ is assumed to be 1 h. With the nominal LHC beam parameters, this case corresponds to 100 kW on the collimation system.

- Transient losses condition: an increase of losses is detected and the collimator must withstand for 10 s a power corresponding to a $\eta_{b,min}$ of 0.2 h. In this situation, 500 kW are dissipated on the collimators.

The energy deposited by the lost particles and the material properties determine the temperature increase and the deformation.

Collimators are the closest elements to the beam. For this reason, besides operational losses, collimators represent also the first defence in case of accidental beam losses. Errors during injection from the SPS or during the beam dump must be taken into account, for example, to design the collimation system. The passive machine protection in this case represents one of the critical aspects to be considered for their design.

In the vicinity of the collision points, different collimators are placed to fulfill two main functions: they reduce the background of the experiment measurement related to the halo-induced noise and they clean the outgoing beam from the collision products.

On the top of the aforementioned functions, collimators are also useful because they concentrate the radiation dose, limiting the activation of the equipment along

the ring and they also prevent the long-term effects of radiation damage to sensitive equipment such as warm dipoles.

In order to fulfill all these functions and driven by the requirement to keep a cleaning efficiency that ensure quench protection, a multi-stage collimation system is implemented, as shown in Fig. 2.4 . Collimators can be classified as a function of their distance from the beam in [81]:

- Primary Collimators or Target Collimators Primary (TCP). These objects are the closest to the beam and they first intercept the losses. Some of the particles, however, escape without being absorbed, forming the secondary halo. On the top of this, in primary collimators the interaction of the primary halo with the material produces secondary particles, and, at these energy, an hadronic and electromagnetic cascades are generated.

- Secondary Collimators or Target Collimators Secondary (TCS). They are further from the beam with respect to the primary collimators. Their role is to intercept the secondary halo and the hadronic shower induced in the primaries.

- Target Collimators Long Absorber (TCLA). They attenuate the particle shower and the tertiary halo.

- Tertiary Collimators or Target Collimators Tertiary (TCT). They protect the magnets that are providing the final focusing to the beams before the experiment. This represents the bottleneck aperture during physics experiment.

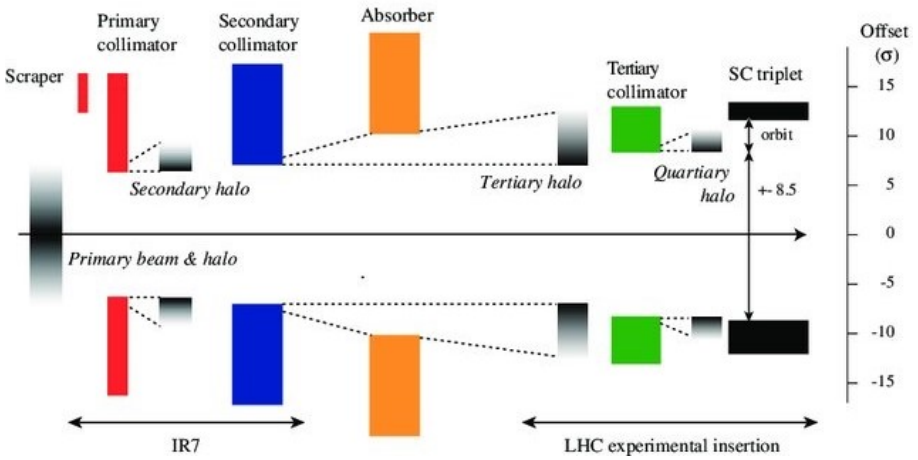

Figure 2.4: The LHC multi-stage collimation system. Collimators are classified as a function of their distance from the beam [80].

In addition, other collimators are installed to protect the system from injection or extraction errors or to clean the particles debris after collisions.

Collimators are horizontal, vertical or screw to further optimize the cleaning. A summary of the collimators installed in the LHC is given in Tab. 2.2. In total, more than 100 collimators are installed in the ring to clean the beam and protect the machine [78].

Functional type	Name	Plane
Primary IR3	TCP	H
Secondary IR3	TCSG	H
Absorbers IR3	TCLA	H,V8
Primary IR7	TCP	H,V,S
Secondary IR7	TCSG	H,V,S
Absorbers IR7	TCLA	H,V
Tertiary IR1/2/5/8	TCTP	H,V
Physics debris absorbers	TCL	H
Dump protection	TCSP/TCDQ	H
Injection protection	TCDI/TDI/TCLI/TCDD	H,V

Table 2.2: List of collimators installed in the LHC, belonging to different families and installed in different insertion regions.

2.3.3 LHC collimator design

The specific configuration of a collimator depends on its specific role and position, but the general design features are common for all the families mentioned in in Tab. 2.2 [71, 78, 82]. The collimators are composed of a stainless steel vacuum tank, which is placed on a support with different orientation (vertical, horizontal, skewed). The beam is entering in the vacuum tank, which is connected through flanges to the beampipe, as illustrated in Fig. 2.5(a). Inside the vacuum tank, two parallel jaws are installed. The beam is passing in the middle of the two jaws, which are typically separated by 2 mm, as shown in 2.5(b). They are provided with an actuation system to move inwards or outwards the beam. The jaws are made of dispersion strengthened copper (Glidcop®) bars, brazed on copper cooling pipes to evacuate the heat load induced by the beam. The jaws host the active part of the collimator, the absorber, which is shown in Fig. 2.6. The taperings are the final blocks of the jaw and they provide a smooth transition between the beam line geometry and the jaw narrow aperture, to avoid beam instabilities. A similar function is played by RF fingers, shown in Fig. 2.5(b) [82].

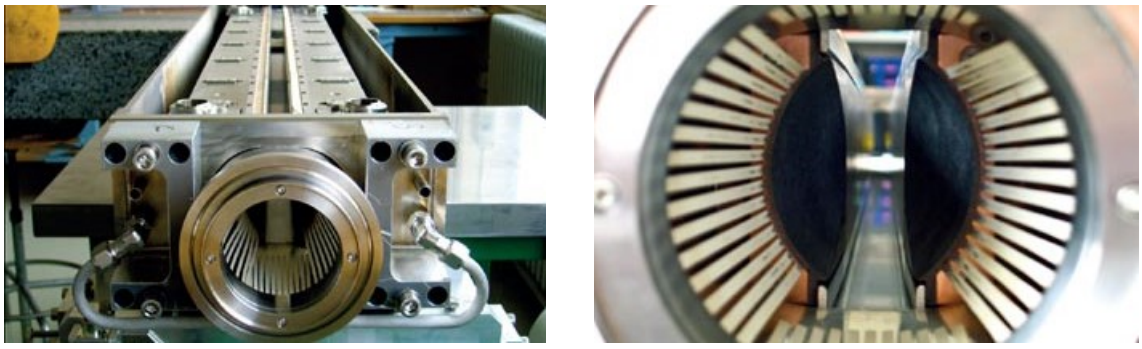

(a) Vacuum tank-external view.

(b) Jaws installed in the tank.

Figure 2.5: Pictures of a LHC collimator.

The collimator design plays a key role to ensure their correct behaviour. An efficient design permits, in fact, to evacuate the thermal load and to maintain tight

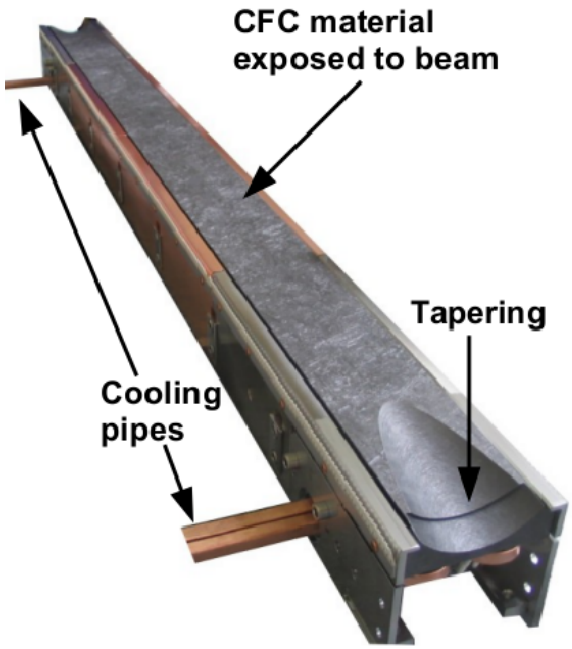

Figure 2.6: Picture of a LHC jaw before its installation in the tank. The absorber material is the part exposed to the beam and, in this examples, is made of carbon-fibre-carbon (CFC).

dimensional tolerances and mechanical stability. This is a fundamental requirement for high-precision devices which operate in the vicinity of the beam.

2.3.4 LHC collimator absorber materials

The absorber blocks installed in the collimators jaws are the key element because they actively interact with the particle beam. For this reason, the material composing the blocks must satisfy different stringent requirements in order to properly clean the beam and protect the machine, while keeping its structural integrity.

The main technical characteristics of an ideal absorber material are listed below [11]:

- Maximum electrical conductivity. A charged travelling particle induces an electromagnetic field on the surroundings, the so-called wake-field, which can, in turn, act back on the beam [83]. The beam coupling impedance describes the intensity of the perturbation exerted on the beam. For a cylindrical beam pipe, the impedance is inversely proportional to the square root of the electrical conductivity of the surrounding material [84]. A conductive material dissipates in an effective way the accumulated charges, which would perturb the successive train of beam.

- Minimum outgassing rate. The outgassing rate is the quantity of gases leaving the surface of a material per unit time [85]. The maximum pressure in the LHC must be limited because beam-gases interactions are one of the principal causes

of losses and beamtime limitation. For this reason, the maximum outgassing rate of a collimator is fixed to $2 \cdot 10^{-7}$ mbar l/s [86, 87]. This limit is shared between all the components of the collimator, and half of this is allocated to the absorber material [88].

- Maximum thermal conductivity. The beam-induced heating must be dissipated efficiently to limit the thermal gradient and hence the thermal-induced deformation, which compromise the geometrical stability. The maximum allowable temperature is also related to the outgassing rate, which increases with temperature [85].

- Minimum thermal expansion coefficient. The increase of temperature induced by the beam induces a dimensional change which must be minimized to ensure dimensional stability to the collimator jaws.

- Maximum melting temperature. During accidental situations, the absorber can reach a very high temperature which must be lower than melting.

- Maximum specific heat. In the accidental scenario, it limits the maximum temperature.

- Maximum ultimate strength. This requirement is related to the requirement of surviving to accidental beam impact where high stresses are reached.

- Minimum elastic modulus. Collimators under steady state losses are subjected to a deformation-imposed load case. A small elastic modulus allows reducing the corresponding induced stresses.

- Adequate density. The density is one of the parameters that is influencing the absorption of particles. For this reason, it should be high enough to ensure a high fraction of captured particle, but at the same time, the energy deposition must guarantee an increase of temperature compliant with the aforementioned requirements. As a function of the distance from the beam, a different heat load affects the absorber. Primary collimators are very close to the beam, the fraction of intercepted particle is greater and hence a lower density is envisaged to avoid a huge energy deposition. On the contrary, tertiary collimator are the last barrier of protection and hence the density must guarantee to stop the incoming particles.

- Maximum radiation damage hardness. As explained in Ch. 1, the interaction of high energy particles with matter induce microscopic and macroscopic degradation of material which should be minimized to ensure a long lifetime of the components.

On the top of these characteristic, the industrial feasibility, the cost and the production timeline must be evaluated. It is also worth mentioning that the elemental composition of the absorber materials determines their radioactive activation. This aspect must be monitor to foreseen access restriction or waiting time before technical intervention [10]. None of the existing materials possesses all these properties, and a compromise must be therefore found to ensure the correct operation of the

collimator system. The aforementioned requirements are to some extent even contradictory: the need of increasing the electrical conductivity, for example, is typically accompanied by an increase of density which could lead to an excessive energy deposition. For this reason, *Figures of Merit* (FoM) are introduced to orient the material choice [11]. These indexes combine several properties in a single parameter, and they are used to compare the materials envisaged for collimators: the higher the indexes, the better would be the collimator performances [80]. In particular, these FoM are defined:

- *Thermo-mechanical robustness index* (TRI). It includes thermal and mechanical properties to represent the robustness against beam impact.
- *Thermal stability index* (TSI). It combines the thermo-physical properties that determine the geometrical stability under steady-state heat loads.
- *Impedance index* (RFI). It expresses the needs of reducing the collimator contribution to impedance.

In the LHC collimator system primary and secondary collimators are made of a Carbon-fibre Carbon (CFC) Composites, while for denser tertiary collimators a tungsten alloy is selected.

Carbon-fibre Carbon (CFC) Composites

Carbon-fibre composites are widely used in different industries such as aerospace, cars, competition skis, for their outstanding ability of bearing loads. Carbon-fibre carbon composites are composed by a carbon matrix and they are reinforced by carbon-fibre. The low density, excellent thermal-shock resistance and capability to withstand high temperature [89] make them appealing for using in collimators.

The CFC adopted for LHC primary and secondary collimator is named AC150K®) and it is produced by Tatsuno/Across, now CFC Design, Inc. (Japan). The fibres are randomly oriented in a plane, and then several layers are stacked [90]. The orientation of the material inside a jaw is shown in Fig. 2.7. The in-plane directions are not completely equivalent because of a rolling step during the production of the materials. The graphitization is finally enhanced by a thermal treatment at 2800°C.

Tungsten alloy

Tertiary collimators are subjected to lower heat load, then their density can be increased to ensure an adequate particle absorption. For LHC collimator, a tungsten alloy commercially known as INERMET®180 is used. It contains 95%$_{wt}$ of W, 3.5%$_{wt}$ of Ni, and 1.5%$_{wt}$ of Cu. The NiCu phase infiltrates between the W grains providing good thermo-physical properties and a high density.

2.4 The HL-LHC collimation system

2.4.1 Introduction to the HL-LHC

The LHC has given numerous contributions to the understating of the fundamental laws governing the universe. Among them, it is relevant to mention the detection of

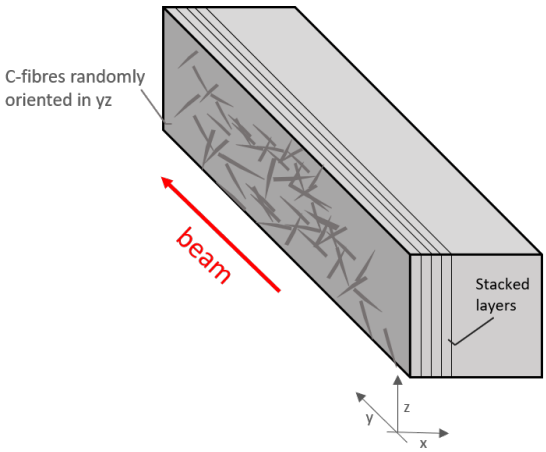

Figure 2.7: Representation of CFC material orientation inside a jaw. The plane where fibres are oriented is parallel to the beam direction. Modified from [80].

the Higgs boson in 2012 [91], whose existence is predicted by the Standard Model theory. Already in 2010, a design study to implement the High-Luminosity Large Hadron Collider (HL-LHC) has been conducted at CERN, and in 2015 a baseline program was approved to plan physics until 2030.

The aim of HL-LHC is to increase the statistic of the available data by making available a higher number of events. The number of events per second N_{event} is related to the cross-section of the phenomena under study σ_{event} and the luminosity L, as shown in Eq. 2.2

$$N_{event} = L\,\sigma_{event} \tag{2.2}$$

The HL-LHC target is indeed to increase the LHC design luminosity of a factor five in order to obtain a higher number of events. The luminosity depends on different beam parameters among which the number of particles per bunch, the number of bunches per beam, and the crossing angle at the interaction points. A comparison between the LHC and HL-LHC beam parameters is given in Tab. 2.3 [92].

	Nominal LHC	HL-LHC
Beam energy in collision [TeV]	7	7
Particles per bunch, N [10^{11}]	1.15	2.2
Number of bunches per beam	2808	2748
Energy stored per beam [MJ]	362	678
Peak luminosity [$10^{34}\ cm^{-2}\ s^{-1}$]	362	678

Table 2.3: Main beam parameters of LHC compared to the upgraded HL-LHC.

The realization of the high-luminosity configuration relies on a number of technological improvements: the upgrade of the superconducting magnet and cold powering system, the introduction of new superconductive RF crab-cavities, and the upgrade of the collimation system that is detailed in this work. The increased number of particles per bunch, and hence the higher energy stored in the beam, represents a key parameter to understand the collimator upgrade.

2.4.2 New challenges for collimators

An immediate consequence of the higher particles per bunch is the increase of the heat load that collimators must withstand both in normal and accidental scenarios. In particular, the operational losses for design scenario are shown in Tab. 2.4 for LHC and HL-LHC.

	LHC	HL-LHC
η_b=1 h	100 kW	190 kW
η_b=0.2 h	500 kW	940 kW

Table 2.4: Operational losses on the collimation system for LHC and HL-LHC.

This requirement is partially accommodated by a new design of the collimator jaws. In particular, an improved thermal contact between the absorber material and the Glidcop jaws facilitate the heat dissipation [93].

The increased energy deposited in the collimators also translates into a higher radiation damage expected at the end of collimators lifetime. For this reason, the long-term effects of radiation on the material becomes an increasingly relevant topic to be considered in the material selection.

The efficiency of the LHC collimation system is defined as the ratio between the particles safely disposed by collimators and the particles lost at the sensitive equipment. With the increased energy stored in the beam, the efficiency must be increased to keep the energy lost in the magnets below the quench limit. This limitation is overcome with the installation of additional absorbers in the most exposed regions [80].

The most stringent requirement for HL-LHC collimators is, however, related to the beam instability induced by the beam-coupling impedance, whose major contribution comes from the collimator absorber materials, and from CFC in particular [94, 95]. The higher beam intensity calls for reducing the beam-coupling impedance, hence to increase the electrical conductivity of the absorber materials. The selected materials must always satisfy the FoM mentioned in 2.3.4, and it must survive to the new operational loads.

For the HL-LHC collimators an intense R&D program has started more than ten years ago at CERN, together with the support of different European programs (EuCARD, EuCARD2 [1], ARIES [2]) and external companies.

The materials finally selected for HL-LHC collimators are:

- Molybdenum-carbide graphite composite (MoGr) for primary collimators
- MoGr with 6 μm of Mo coating for secondary collimators
- Copper-diamond composite (CuCD) for tertiary collimators

It is worth mentioning that the validation of materials for this application involves a variety of tests to prove peculiar characteristic that are typically unknown. Besides the thermo-physical and mechanical properties that are tested at CERN in a wide range of temperature [96], the material must be tested under vacuum [97]. Their response under particle beam is assessed to simulate radiation damage [80] or beam-induced instantaneous heating, in order to simulate accidental scenario. This

last property is tested in CERN facility called HiRadMat (High irRadiation to Materials) [98]. Several tests have been done during years to assess the thermo-mechanical response of novel materials for collimators material under quasi-instantaneous heating [60, 93, 99–102]. In the last experiment named MultiMAT a variety of novel material have been tested, including coated samples, as shown in Fig. 2.8

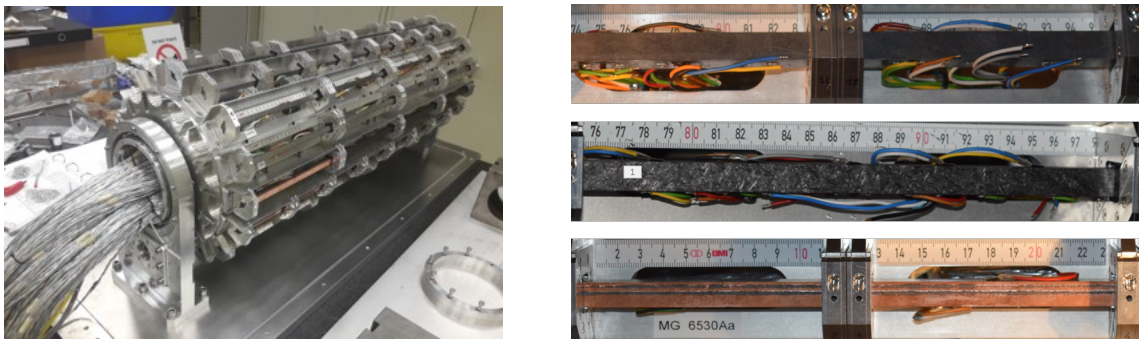

(a) The MultiMAT vacuum tank showing all the lines for holding different materials

(b) Samples after beam impact: from the top: MoGr, CFC, Cu-coated MoGr.

Figure 2.8: Some images of the configuration of the MultiMAT experiment.

2.4.3 Novel materials for collimators

Molybdenum-carbide graphite composites

Molybdenum-carbide graphite composite (MoGr) has been developed by CERN in collaboration with BrevettiBizz (Verona, Italy).

The idea is to combine the excellent thermal properties of graphite with the high strength and electrical conductivity of Mo. Over years, different compositions and production parameters have been changed, and the influence of these conditions on the final properties of the material are largely characterized [80, 90, 103].

The production of MoGr is divided into four steps:

- Powder mixing. Graphite and molybdenum particles are mixed in a dry environment to guarantee a good homogeneity. In some grades, additional metallic powders or carbon-fibres are added.

- Green body compaction. The first compaction step is a cold uni-axial pressing. The graphite powders start orienting with the basal plane perpendicular to the pressing direction.

- Sintering. The green body is then sintered in a Spark Plasma Sintering (SPS) machine, where a current flowing in the graphite mould represents the heating source. The temperature reached during this phase ranges from 2600-2700 °C, with an applied pressure around 35 MPa. Above 1000 °C, all the Mo reacts with C atoms to form Mo_2C. At the same time, the combined action of temperature and pressure enhances the graphitization of the material. The final morphology of the material resembles the one of a transversely isotropic

material: the graphite basal plane are oriented perpendicularly to the compaction direction (x), and properties along the basal planes direction (yz) are equivalent, as schematically shown in Fig. 2.9. If the eutectic temperature of the Mo-C system is reached (2854 °C), the liquid phase (LP) carbides can be spilled out and impregnate the mould, making difficult to estimate the final composition of the composites. The LP sintering is believed to further enhance the graphitization of the material, giving rise to a more ordered structure [103].

- Annealing. This post-sintering thermal treatment is performed in a pressure-free configuration, aiming at releasing the stress induced in the material during sintering.

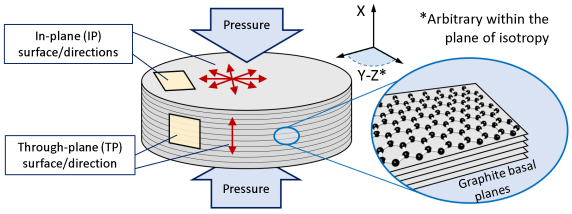

Figure 2.9: Orientation of the basel plane of graphite in MoGr compared to the pressing direction during the sintering process [103].

The resulting microstructure of one of the recent grade studied is shown in Fig. 2.10. The graphite matrix is compact, but some porosity is still present especially close to the surface. This effect is believed to be related to the machining. The carbide particles are uniformly dispersed in the matrix.

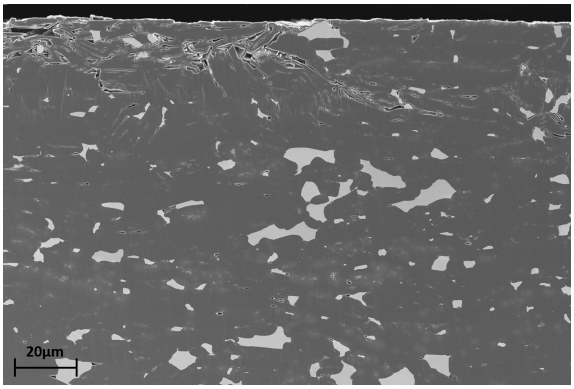

Figure 2.10: A micrograph of the MoGr cross-section: the brigher particle are MoC, while the graphite matrix is darker and it shows some porosity [88].

The properties of this composite can be tailored by changing the production parameters: the density, for example, can be increased with a higher percentage of Mo, as in the first grades studied [90]. A higher density can also be obtained by increasing the temperature or the duration during the sintering process: the enhanced compaction leads to the closure of some of the porosity present in the material. The higher compaction also increases the electrical conductivity, but a higher outgassing rate is detected in the denser grades of the material. The smaller dimension of the channels connecting the bulk of the material to the surface leads to

a slower emptying of gases trapped in the porosity: it is believed that, for this reason, the final outgassing is higher in denser grades of MoGr. Vacuum compatibility is one of the fundamental requirements of absorber materials in collimator, for this reason all the production parameters are optimized to guarantee low outgassing, while keeping the standard required for electrical and thermo-mechanical properties [88].

It is useful to introduce the formalism for the classification of the different MoGr grades. The nomenclature codes are:

$$MG - \#\#\#\# - Aa \tag{2.3a}$$

$$Na - \#\#\#\# - Aa \tag{2.3b}$$

The code in 2.3a refers to the material produced by BrevettiBizz, and the first letter simply stay for Molybdenum-Graphite. The code in 2.3b is instead used for a second producer of MoGr, the company Nanoker (Oviedo, Spain), indicated by the first latter N, and the second letter indicates the conditions of the powder mixing. The four central digits represent the volume fraction of the different component: molybdenum, graphite, carbon-fibres, others. The uppercase letter identifies the sintering cycle, whose temperature, pressure, and duration are recorded. Finally, the last letter is dedicated to the annealing cycle parameters.

Molybdenum coating

For HL-LHC secondary collimators, a 6 μm Mo coating on the MoGr surface exposed to the beam is foreseen. This conductive coating further decreases the collimator contribution to the impedance budget of the accelerator. At high frequency (1 GHz), the skin depth seen by the beam is much lower than 5 μm of Mo. The material behind the coating is not influencing the beam behaviour.

This approach cannot be pursued for primary collimators; being too close to the beam the losses would vaporize the coating in a few turns [104]. The coating material must satisfy not only the impedance requirement, but a good adherence to the substrate must be guaranteed to avoid perturbing the UHV with coating particles detached from the surface. In case of an accidental scenario, it is also important to ensure a good robustness of the coating. For this reason, Mo is preferred to Cu that has a lower melting temperature.

The Mo coating of low impedance collimators is produced with High-Power Impulse Magnetron Sputtering (HIPIMS). This coating is extensively studied in this work.

Copper-diamond composites

Copper-diamond composites combine a very high thermal conductivity with a low CTE and for this reason they have been considered for different thermal management application. CuCD the baseline for HL-LHC tertiary collimators. The material is produced by hot pressing of copper and diamond particles, by adding a quantity of binders (boron, zirconium, molybdenum, chromium, etc.) to form carbide at the Cu-diamond interface and compensate to the luck of affinity between the two elements [90]. The grade foreseen for collimator should contain around the 66%$_{vol}$ of diamonds, the 33%$_{vol}$ of copper and around 1%$_{vol}$ of binders [60].

2.4.4 Production and installation of low-impedance HL-LHC collimators

The first MoGr collimator was produced in 2016 and the prototype was installed for the LHC run during 2017-2018. The blocks installed permit to test three different approaches: the central part is uncoated, while the outer area are coated respectively with Mo and TiN coating, as visible from Fig. 2.11. In 2019, the jaws installed in the collimator was investigated with a dedicated tool, and no beam damage to the coating was observed [105].

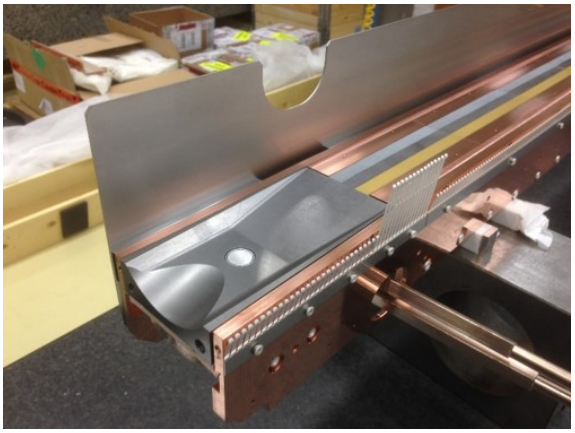

Figure 2.11: A picture of the TCSPM prototype installed in the LHC. The blocks are coated with Mo on one side, uncoated in the central area and coated with TiN on the other side.

Between 2018-2020, MoGr blocks to equip 5 TCPPMs and 10 TCSPMs (coated blocks) have been produced and 12 of these collimators have been installed in the tunnel for the HL-LHC operation.

The material installed in the collimators is the grade NB8304Ng produced by Nanoker. The composition and the high-temperature treatment parameters are optimized to satisfy the thermo-physical, mechanical and UHV requirements [88]. Prior to their installation in the jaws, MoGr blocks are vacuum fired at 950°C for 72h to minimize the outgassing rate. For Mo-coated blocks, the surface is cleaned in an ultrasonic (US) baths before the coating is applied to ensure a good adherence [106, 107].

The installation of MoGr in the collimator jaw, and a new TCPPM collimator in the tunnel are shown in Fig. 2.12(a) and Fig. 2.12(b).

(a) TCPPM jaw with MoGr blocks installed. (b) A TCPPM installed in the tunnel

Figure 2.12: Pictures of new HL-LHC low-impedance collimators.

Chapter 3

Irradiation campaigns for collimator materials

This chapter focuses on the irradiation campaigns dedicated to materials for BIDs, and for collimators in particular. The expected radiation levels reached in the LHC and in the HL-LHC are presented, and these conditions are compared to those obtained in different tests. The focus is then placed on the design of the last experimental campaign held in 2019. The results obtained in this experiment are, in fact, described in the following chapters of this work.

3.1 Radiation damage levels in the LHC collimators

Collimators play a fundamental role in the operation of a high intensity accelerator, as explained in Ch. 2. Their correct operation relies on a series of outstanding properties that they need to maintain during their lifetime. For this reason, the evaluation of radiation damage in candidate materials for BIDs is important.

As already mentioned before, it is important to distinguish the effects related to thermal shock phenomena, from the ones caused by radiation damage. Accidental beam losses can potentially damage the collimators because of quasi-instantaneous energy deposition that causes plastic deformation, material fracture or evaporation [60].

Operational losses also induce thermal load and deformation, which perturb the operation of collimators [104]. On top of this, regular losses are also responsible for long-term radiation damage: the energy deposition, in fact, is also responsible for dpa accumulation, which may become critical after years of operation.

Design scenarios are defined in Sec. 2.4.2 and they quantify the maximum power absorbed by the collimation system as a whole. The losses are however not uniform around the ring, and different simulation tools are used to evaluate the protons absorbed at each collimator site. These values are used as an input to evaluate the energy absorption and the radiation damage profiles according to the procedure explained in the next section.

3.1.1 Calculation of dpa in the LHC

The radiation damage in collimators can be estimated with the dpa value or with the gas production. Both these value can be calculated thanks to a complex chain of simulations [108, 109].

The results presented in this work are obtained with the following procedure. The step is a particle tracking code named SIXTRACK [110] which permits to calculate the trajectories of the particles populating the halo along the LHC ring [80]. A scheme of the aperture throughout the accelerator is integrated to determine the position where halo particles impact primary collimators defining the loss maps.

The locations of the particle lost is given as an input to a Monte-Carlo code named FLUKA. When a particle is intercepted by a collimator jaw, the interaction mechanisms are simulated in FLUKA [111]. This program includes different physical models: the ionisation, coulomb scattering, nuclear elastic and inelastic interactions [23]. FLUKA can also track the secondary particles generated by high energy protons in the hadron or electromagnetic showers. Different outputs are obtained from the simulations: in particular, the dpa, the gas production or the energy deposition. This last quantity serves as an input for finite element codes to calculate the temperature increase and the mechanical response of collimators.

In this thesis, the focus is on the radiation damage effects, and the dpa is used as the relevant parameter to compare radiation level in the LHC and in the irradiation campaigns. A detailed explanation of the implementation of radiation damage in FLUKA is given in literature [25]. It is important to mention that the dpa model is based on the NRT model described in 1, but the athermal recombination induced by the annealing of intra-cascade defects is considered in FLUKA. For a primary knock-on atom (PKA) with a kinetic energy T of 20-100 keV, the number of surviving defects N_F is typically 0.2-0.3$\cdot N_{NRT}$ [25].

3.1.2 Results

Once the distribution of losses around the ring is known, the total number of protons lost during the collimator lifetime must be estimated to simulate the effective dpa received at the different insertion regions. The estimation of losses during operation is possible thanks to the beam loss monitors (BLM) installed in the ring. The total dose measured by the BLM, coupled with FLUKA simulation of the BLM response to a single proton, gives the total number of protons lost per year. After different hypothesis, it is found to be reasonable to scale the proton losses with the integrated proton intensity, which represents the number of protons circulating in the machine at all times [109]. The calculated dpa values in collimators presented below refers to a total proton losses in the collimation system of 10^{17} during the HL-LHC.

In Tab. 3.1 the peak dpa values for the most loaded primary and secondary collimator is reported.

It is important to notice that primary collimators, opposite to secondaries, have a sharp distribution of the dpa, which is concentrated in an area with an extension perpendicular to the beam of about 1 mm, as shown in Fig. 3.1.

As a comparison, it is worth noticing that the peak dpa value calculated for the CFC primary collimators during run 2, with an estimated losses equal to $7.1 \cdot 10^{15}$, is 0.008.

Peak dpa		
MoGr primary	Mo coating	MoGr secondary
0.18	0.001	0.0004

Table 3.1: Peak dpa expected in MoGr primary collimators and Mo coating MoGr secondary collimators for HL-LHC [109].

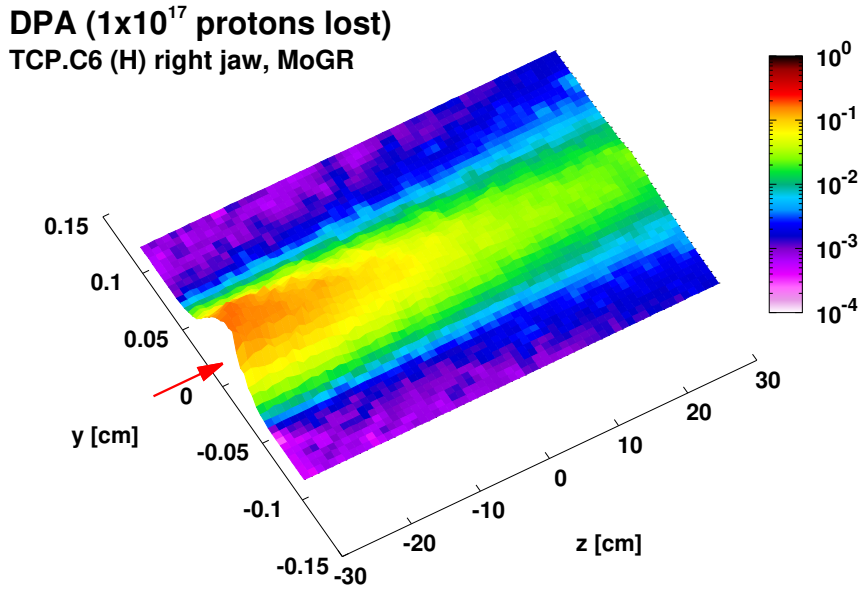

Figure 3.1: Spatial distribution of dpa in a primary collimator. The z direction is parallel to the beam axis.

The aforementioned values are useful to extrapolate the expected radiation effects in the HL-LHC collimators by knowing the property degradation measured in the irradiation campaigns.

3.2 Comparison of ion and proton irradiation

The unique radiation environment created by the 7 TeV protons of the LHC cannot be reproduced elsewhere. For this reason, the radiation hardness of candidate materials for collimators must be evaluated in a different way and in alternative facilities.

In this section, the main concepts of radiation damage explained in Ch. 1 are reviewed to understand the different possibilities to irradiate the materials of interest. The advantages and drawbacks of the different approaches are analysed.

One of the most promising solution to test materials is ion irradiations. This technique is used to simulate the effect of both fission and fusion reaction neutrons or high-energy protons. The low or zero residual activation induced by low energy (some MeV) ions in materials simplify the post-irradiation examination both in term of time and cost. The analysis does not require shielded hot cell and the samples are manageable after test without waiting the activation decay of the radionuclides

produced during the irradiation [32, 112, 113]. Ion irradiation is also convenient because with relatively fast test is possible to reach high dpa values [114, 115]. The dpa is, in fact, proportional to the displacement cross-section, as shown in Ch. 1, and it is higher for heavier ions. For this reason, ion irradiation has a dpa rate, or damage rate, greater than proton and neutron. The immediate drawback of the high stopping power of matter for ions is the relatively small penetration that they reach in the material. When considering ions with energies up to tens of MeV per nucleon (MeV/u), in fact, the expected penetration ranges are around few hundreds of micrometres, as shown in Fig. 3.2.

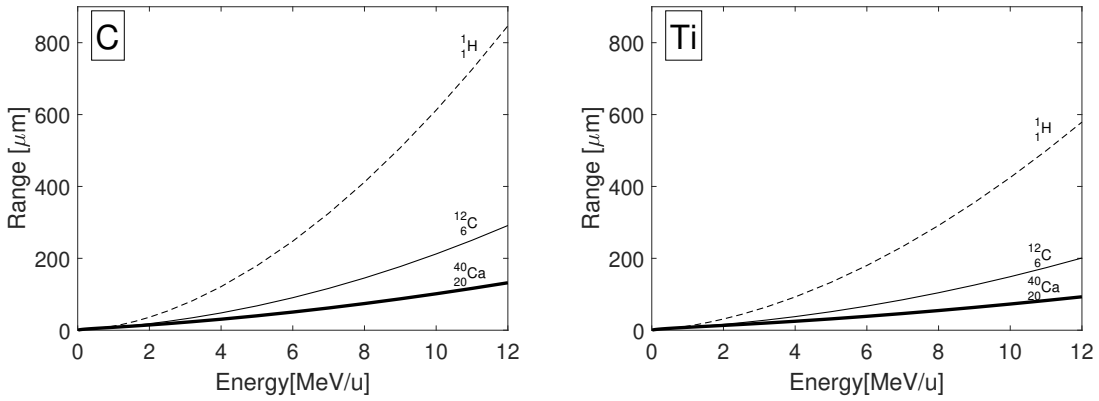

(a) Carbon target.

(b) Titanium target.

Figure 3.2: Comparison of H, C and Ca ions ranges in C and Ti targets. Ranges are calculated with the values presented in [116]

On top of this, energy losses responsible for dpa are orders of magnitude higher towards the end of the ion penetration [3]. For this reason, the dpa distribution presents a peak at the end of the ion range and it is much lower on the sample surface.

Besides the dpa, also the effect of the transmutation products as H and He plays an important role in the mechanism the radiation damage [13]. Ions do not induce nuclear reactions that lead to gas production, and this must be taken into account. This effect is sometimes simulated by dual beam irradiation: He or H are injected in the material before or simultaneously to other species that induce dpa [117].

Irradiation with protons having energies around few hundreds of MeV is also investigated as an alternative to simulate both the dpa damage and the gas production [58, 118]. The cross-section for nuclear reactions that generate gas products depends on the particle energy, and the threshold energy is around 5-10 MeV [113]. For this reason, the appm/dpa value, which could be used to compare the irradiation conditions, may be tailored to match the required value.

A summary of the main differences between the proton and ion irradiation is shown in Tab. 3.2.

The understanding of the difference between ion and proton or neutron irradiation is still an open point in literature. It is a highly investigated field because of the recognized practical and economical advantage of ion irradiation. On top of this, ion irradiation can be very useful to compare the radiation resistance of novel

	Ions	Protons
Activation	Low/Zero	Relevant
Cost	Lower	Higher
Duration	Short	Relatively long
Dose rate	Higher	Lower
Penetration	Superficial	Bulk
Gas production	No	Yes

Table 3.2: Summary of the main characteristics of ion and proton beams irradiation. Modified from [112, 117].

material and can be used in the R&D phase to tailor material characteristic. In the following section, a summary of the irradiation tests on novel materials for LHC collimators is given and the contribution of these tests to the material development is underlined.

3.3 Overview of radiation damage tests on collimator materials

Among present and novel materials for collimators, CFC has been studied the most in terms of radiation damage because it is an interesting option for plasma-facing materials and aerospace applications [56]. Several studies underlined the decrease of thermal conductivity under neutron irradiation [45, 119] and the influence of the production route on the dimensional stability [119]. In particular, the response of a CFC composite under irradiation depends on the microstructure of the fibres and on the graphite matrix [120].

A comprehensive irradiation campaign has been performed at the RRC cyclotron at Kurchatov Institute, in Russia. The CFC AC150K has been tested with protons at energies between 20-35 MeV. An increase of the electrical resistivity up to 200% and a decrease of the thermal conductivity up to 50% are detected at 0.002 dpa. Some samples tested after receiving up to 0.06 dpa show an increase of the electrical resistivity higher than 1000% [121].

More recent studies have been carried out at the Brookhaven Linear Isotope Producer (BLIP) in the Brookhaven National Laboratory's (BNL) in the USA. The facility allows irradiation with protons of energies ranging between 120-200 MeV. The test shows the ability of 2D CFC AC150K (the grade installed in the LHC collimators) to survive to fluences up to 10^{20} p/cm^2, but a relevant increase of distance between graphitic planes is observed [80, 122].

The same grade of CFC has been also tested at the GSI Helmholtzzentrum für Schwerionenforschung (Darmstadt, Germany). Heavy ions with energies up to 11.1 MeV/u induces shrinkage along the plane containing fibres [123]. This behaviour confirms that the fiber planes resemble the basal planes of the graphite structure that contracts during irradiation [56, 122].

MoGr composites have a more recent history, but several irradiation tests have been conducted on different grades during the material development. The first produced grades of MoGr presented severe structural degradation already at low

fluences both under ion and proton irradiation [80, 122, 124]. This behaviour could be related to the instability of MoC phases, while the graphitization level of the compound was already higher than CFC and graphite. The material failure can also be related to the uncontrolled release of internal stresses accumulated during the sintering process. For this reason, high-temperature annealing has been introduced in the material production. The benefit of this treatment has been confirmed by proton and ion irradiation of more recent grades, that survive higher doses. These tests have revealed a lower increase of electrical resistivity for MoGr composites containing C-fibres [80]. On top of this, microstructure analysis seems to point to a beneficial effect of Ti powder addition in the material to stabilize the carbide phase during irradiation [125].

It is worth mentioning that both MoGr and CFC have been tested at BLIP-BNL in January, 2018 in the framework of the RaDIATE [126] collaboration. The irradiated samples are coated with a Mo films of 8 μm. The analysis is foreseen in 2021 and it will be carried out in a shielded hot cell because of the high activation induced by the proton beam.

3.4 Design of new ion irradiation campaigns

In the following sections, the UMAT irradiation experiment performed in 2019 at the M-Branch of the UNILAC accelerator at GSI is described. In this facility, ion species, from proton to uranium, can be accelerated up to 11.4 MeV/u and with a repetition rate up to 50 Hz. The M-branch is composed by three beamlines. For the aforementioned experiment, the M3 beamline is used, as no online measurements are carried out.

3.4.1 Beam parameters

The ion selected for this irradiation campaign is ^{48}Ca, with an energy of 4.8 MeV/u. This combination allows reaching high dpa rates, as shown in Sec. 3.4.3, while keeping acceptable radiation level in the control room next to the beamline. The flux reaches a good stability around $5 - 8.5 \times 10^9$ $\frac{\text{ions}}{\text{cm}^2 \cdot \text{s}}$. The beam is not continuous, but pulsed and the repetition rate is set to 5 Hz. All the relevant parameters, used as input for dpa and thermo-mechanical analysis, are shown in Tab. 3.3.

Parameter	
Ion	^{48}Ca
Charge state	10+
Energy	4.8 MeV/u
Flux	$5 - 8.5 \times 10^9$ $\frac{\text{ions}}{\text{cm}^2 \cdot \text{s}}$
Pulse duration	1.8-5.2 ms
Beam repetition rate	5 Hz
Beam size	2.5×2.5 or 2.7×2.7 cm^2

Table 3.3: Summary of the beam parameters.

3.4.2 Material selection

The irradiation campaign hosted by GSI in 2019 focuses on a range of materials adopted for HL-LHC collimators, but also on possible alternative solutions for collimators and BIDs of future high-energy machines. The main focus is on MoGr composites. The Nb8304Ng, produced by Nanoker and installed in the new TCPPM collimators, is tested. As a comparison, the MoGr MG6541Fc produced by Brevetti and containing C-fibres has also been tested. The composition of the two grades is summarized in Tab. 3.4. It is worth noticing that MG6541Fc is also produced with a higher sintering temperature (> 2700 °C).

	Nb8403Ng	MG6541Fc
$\%vol.$ Mo	5.5	4.4
$\%vol.$ Graphite	93.9	90.1
$\%vol.$ Short C. fibres	-	5
$\%vol.$ Ti	0.6	0.5

Table 3.4: Volumetric composition of MoGr grades.

The CFC is the absorber material in the present collimators. For this reason, it is chosen for this campaign. The grade installed in the LHC is, however, out of production, and for this reason a similar grade named FS140® is selected. Finally, the isotropic polycrystalline graphite SIGRAFINE® R4550 by SGL Carbon SE (Germany) is tested. This material is used in other BIDs.

These materials are characterized by different production routes, different graphitization level and microstructure, which can play a different role in the radiation hardness of the materials.

Together with these samples, which represent the configuration of primary collimators, others are coated with a metallic film to simulate the configuration of secondary collimators. A Mo coating of 6 μm produced with HIPIMS is applied on graphite and MoGr Nb8304Ng. The other MoGr, the MG6541Fc, is coated with Direct Current Magnetron Sputtering (DCMS). The two production processes of coating give rise to a different microstructure, as explained in Sec. 5.2, which can also impact on the radiation hardness. The CFC is not coated because the high roughness characterizing its surface which does not allow reaching the required resistivity values after coating [127]. The detailed analysis of these materials is carried out in Ch. 5. Finally, a Cu coating is applied on the MoGr Nb8304Ng as a comparison with Mo. Cu coating is in fact widely used in accelerators. Mo has been preferred because of the higher robustness in case of beam impact [128], but Cu can still be of interest for future upgrades. A summary of the materials tested is given in Tab. 3.5.

3.4.3 Dpa simulations

The dpa simulations for this experiment are carried out with FLUKA. A summary of the studies done is reported below. In Fig. 3.3 the dpa rate for different materials, coated and uncoated is presented. It is worth noticing that in FLUKA the final dpa depends only on the total number of particles impacting the samples (i.e. the

Bulk material		Coating	
Material	Grade	Material	Technique
MoGr	Nb8304Ng	None Mo Cu	 HIPIMS HIPIMS
MoGr	MG6541Fc	None Mo	 DCMS
Gr	R4550	None Mo	 HIPIMS
CFC	FS140	None	-

Table 3.5: Bulk and coating materials tested in the calcium ion irradiation campaign.

particle fluence). The diffusion and recombination of defects is, in fact, neglected. The dpa rates in Fig. 3.3 refers to a nominal flux of 5×10^9 $\frac{\text{ions}}{\text{cm}^2 \cdot \text{s}}$.

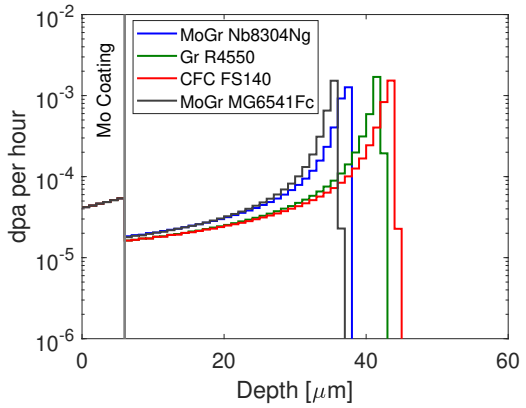

(a) Mo coated samples.

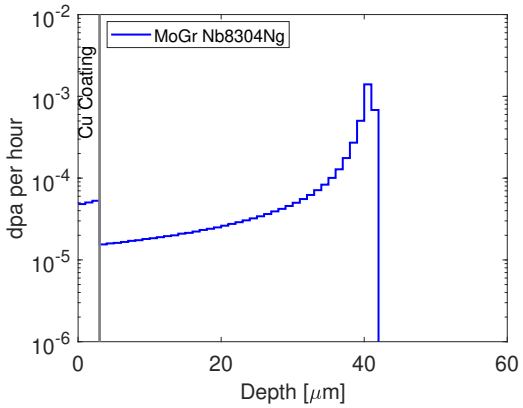

(b) Cu coated samples.

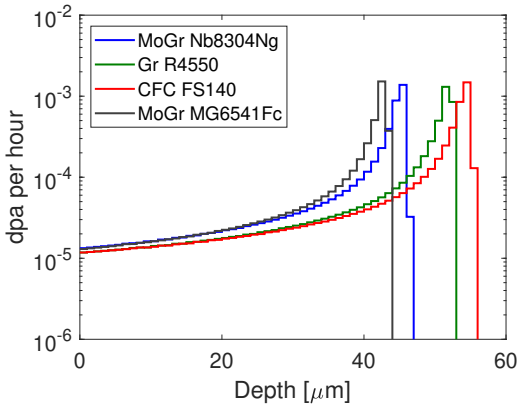

(c) Uncoated samples.

Figure 3.3: Simulated DPA rates as a function of penetration depth for different bulks and coatings.

These simulations are important also to calculate the ion ranges, which serve as

an input to calculate the response of the irradiated layer and extract its properties, as detailed in Ch. 4. The displacement energies E_d for the coatings are considered equal to the ones of bulk metals; that are 60 eV for Mo and 40 eV for Cu. The same E_d is considered for MoGr, CFC and graphite, given the small atom fraction of Mo in MoGr. The materials are however characterized by different densities which impact on the stopping power of the target, as explained in Sec. 1.3.1, and therefore on the particle range. For this reason, different simulations are performed to understand the relation between the sample density and the maximum penetration of ions. This study allows interpolating a function to calculate the penetration of particles for each samples, whose apparent density is measured before the test as explained in Sec. 4.2. The result of the interpolation is shown in Fig. 3.4.

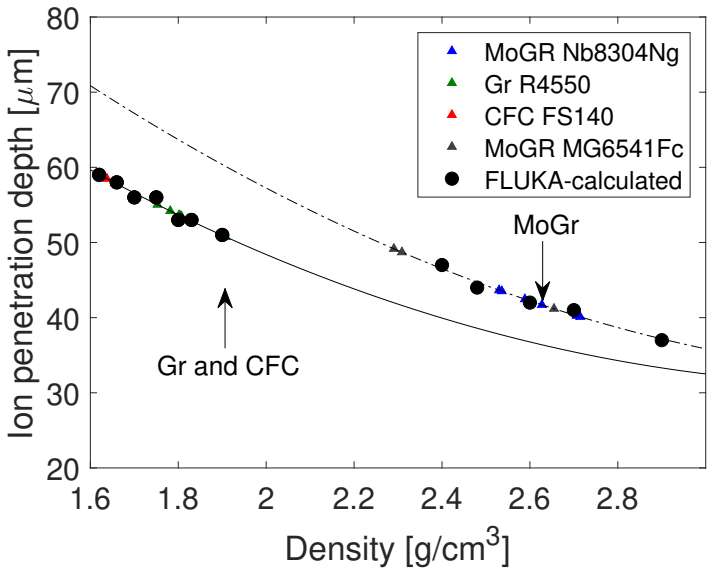

Figure 3.4: Ion penetration as a function of sample apparent density. The black dots are the FLUKA-calculated values used to fit the curves. The measured densities of each sample serve as input for the range calculation.

3.4.4 Specimen size

The size of the irradiated samples has been chosen to allow a broad post-irradiation analysis. For this reason, two specimen sizes are used:

- Thin platelets of 20x5x0.15 mm.
- Disks with 10 mm diameter and 1 mm thick.

The thin samples are foreseen for thermal and electrical measurement: these techniques, as detailed in Ch. 4, are bulk measurement and the contribution of the irradiated layer must be considered. Thick samples are designed to guarantee higher robustness in microscopic analysis where the sample need to be glued to a substrate.

The lateral dimensions are conceived to maximize the number of tested samples and to guarantee a uniform irradiation.

For anisotropic materials, the beam is impacting perpendicularly to plane that in the collimator jaws is oriented to the beam, as drawn in Fig. 3.5.

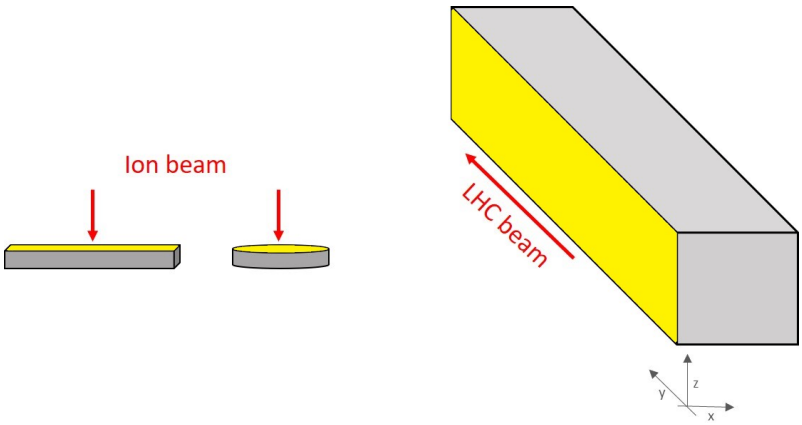

Figure 3.5: Orientation of the impacted surface in the ion irradiation compared to the orientation of the surface in the LHC collimator jaw.

3.4.5 Holder composition and fluence

The holders allow for four sample irradiation positions that can be individually exposed to the beam that is defocused and collimated with a slit before impacting. This system allows reaching different fluences, and therefore dpa, on the different target locations. For some materials, additional samples are tested at intermediate fluences. A summary of the fluences and corresponding dpa reached during the test is presented in Tab. 3.6.

Fluences $\left[\frac{\text{ions}}{\text{cm}^2}\right]$	Irradiation time [s][1]	Peak dpa coating	Peak dpa bulk	Average dpa bulk
$1 \cdot 10^{12}$	200	$3 \cdot 10^{-6}$	$8 \cdot 10^{-5}$	$5 \cdot 10^{-6}$
$1 \cdot 10^{13}$	2000	$3 \cdot 10^{-5}$	$8 \cdot 10^{-4}$	$5 \cdot 10^{-5}$
$2 \cdot 10^{13}$	4000	$6 \cdot 10^{-5}$	$1 \cdot 10^{-3}$	$1 \cdot 10^{-4}$
$7 \cdot 10^{13}$	14000	$2 \cdot 10^{-4}$	$6 \cdot 10^{-3}$	$3 \cdot 10^{-4}$
$1.4 \cdot 10^{14}$	28000	$4 \cdot 10^{-4}$	$1 \cdot 10^{-2}$	$7 \cdot 10^{-4}$
$4 \cdot 10^{14}$	80000	$1 \cdot 10^{-3}$	$3 \cdot 10^{-2}$	$2 \cdot 10^{-3}$

[1] Considering an ion flux of 5×10^9 $\frac{\text{ions}}{\text{cm}^2 \cdot \text{s}}$.

Table 3.6: Irradiation fluences and corresponding peak dpa induced in the bulk and in coating according to FLUKA simulation. The dpa presented are the mean values of the dpa calculated for the different materials, as the percentage standard deviation is 4% for the average dpa, 6% for the peak dpa and 1% for the coating.

The average bulk dpa presented in Tab. 3.6 refers to the uncoated samples. For the coated ones, the dpa distribution is different, as shown in Fig. 3.3. The average dpa for coated samples is calculated and it is almost 30% higher with respect to the uncoated.

Four samples are installed in each slot. In total, five samples holder hosting 80 samples are tested. The images of the samples installed in the holders are presented in Fig. 3.6.

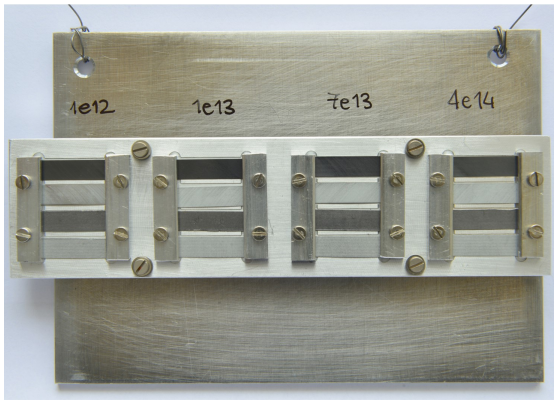

(a) Holder #1.

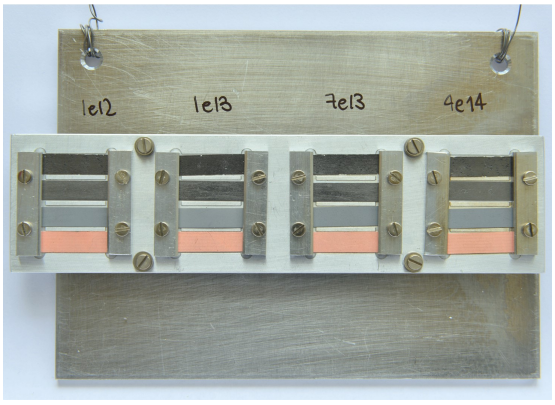

(b) Holder #2.

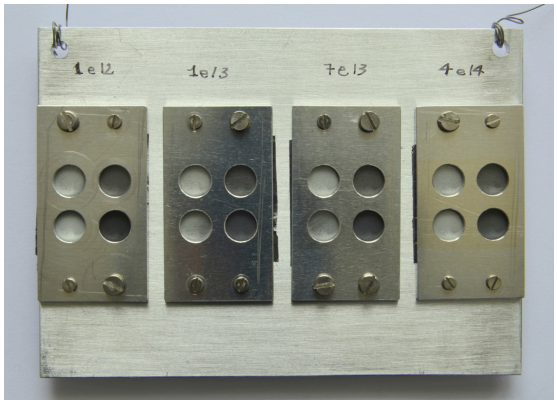

(c) Holder #3.

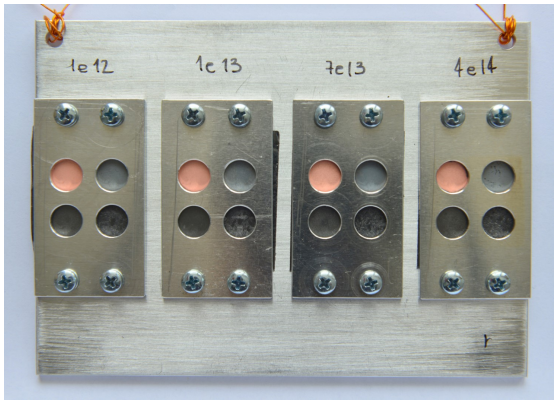

(d) Holder #4.

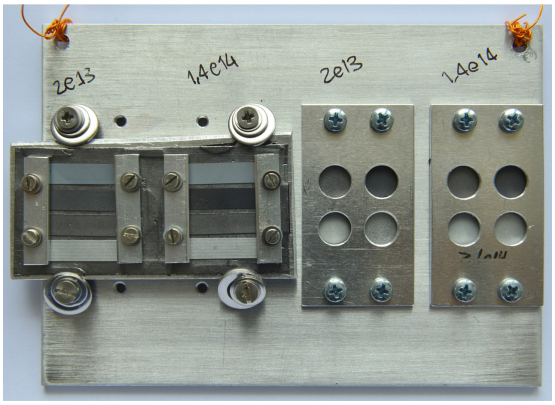

(e) Holder #5.

Figure 3.6: Pictures of the five irradiated sample holders.

3.4.6 Thermo-mechanical analysis of the design

In the following section, the finite element simulations performed with ANSYS© Workbench™are presented. The analysis is performed to verify the maximum temperature reached by the samples during the beam energy deposition. It is important to assess the temperature because it represents a fundamental parameters for the onset of the defect annealing and therefore the evolution of the microscopic damage, as explained in 1.

Thermal analysis

The particle energy which is ultimately converted into heat comes from the ionizing energy losses. This mechanism is by far the most dominant reason of particle energy losses [12], and it is therefore possible to assume that all the energy content of the beam is converted into heat.

As mentioned in Sec. 3.4.1, the ion beam is pulsed and the repetition rate is therefore needed to calculated the power deposited on the samples. The power per impact P_{impact} is, in fact, calculated as shown in Eq. 3.1:

$$P_{impact} = \frac{E_{nucleon} \cdot N \cdot \phi}{f \cdot t_{pulse}} \tag{3.1}$$

Where $E_{nucleon}$ is the energy per nucleon, which is multiplied by the number of nucleons per ion N and the time-averaged flux ϕ to obtain the beam power density. This value is divided by the repetition rate f and the pulse duration t_{pulse} to extract the P_{impact}. For the design, a nominal flux of $\phi = 8 \cdot 10^9 \ \frac{\text{ions}}{\text{cm}^2 \cdot \text{s}}$ and a time pulse of $t_{pulse} = 3.5$ ms of are considered. With these values and the parameters of Tab. 3.3, the resulting power per impact is $P_{impact} = 16.86 \ \frac{\text{W}}{\text{cm}^2}$.

A thermal transient simulation is performed to analyse the temperature evolution at different times, and therefore at different particle fluence.

The boundary conditions assumed for the analysis are:

- The power is considered uniform over the irradiating area and it is considered as a surface thermal flux, neglecting the small penetration depth of ions.
- Radiative heat transfer is considered between the sample holder and the vacuum chamber during irradiation. The emissivity of the aluminum sample holder is assumed equal to 0.1.
- Conductive heat transfer is assumed between the sample holder and the support on which it stays during irradiation. The contact pressure is guaranteed by the holder self-weight and the conductance, calculated according to Eq. 3.2 [129], is 40 $\frac{\text{W}}{\text{m}^2 \cdot \text{K}}$.

$$C = 1.55 \cdot \frac{k_s \cdot m_{ab}}{\sigma} \cdot \left(\frac{\sqrt{2} \cdot P}{E' \cdot m_{ab}} \right)^{0.94} \tag{3.2}$$

  where k_s is the equivalent thermal conductivity of the coupled materials, m_{ab} is the root mean square value for the surface profile slope measured in radians, P is the contact pressure σ is the surface roughness parameter and E' the Hertzian elastic modulus.

The same formula is also used to compute the conductance between the samples and the holder. In this case, the contact pressure is ensured by the tightening torque applied to the screws. A summary of the thermal conductances C is shown in Tab. 3.7 for the different sample holders, according to the naming convention in Fig. 3.7.

Contact	C_{Disk} $\left[\frac{\mathrm{W}}{\mathrm{m}^2 \cdot \mathrm{K}}\right]$	$C_{Platelet}$ $\left[\frac{\mathrm{W}}{\mathrm{m}^2 \cdot \mathrm{K}}\right]$
Sample-Support (C1)	30000	10000
Sample-Clamp (C2)	80000	40000
Support-Clamp (C3)	-	90000

Table 3.7: Thermal conductance between the samples and the holders used in the thermal simulation.

(a) Disk.

(b) Platelet.

Figure 3.7: Scheme of the sample geometries and thermal conductances with the holders.

This conductance are ensured by considering a preload of each screw equal to 80 N. During operation, the minimum tightening torque achievable correspond to 0.1 $\mathrm{N} \cdot \mathrm{m}$, which correspond to a preload of almost 200 N per screw. During irradiation, the temperature increase leads to an expansion of the components. The stainless-steel screw expands more than the sample, and this would lead to a loss of contact. The aluminum sample holder can partially compensate. The multi-physics problem is not discussed here because the final temperature is weakly affected by this change. The analysis of the variation of the maximum temperature as a function of the boundary conditions assumed for the simulations is discussed in details in Ap. A.

The increase of temperature induced by a beam pulse is represented in Fig. 3.9(a). This approach is computationally expensive because it requires small time-step, and it is not indicated to simulate long period. For this reason, the steady-state temperature reached by the material is computed by assuming a continuous power deposition. The power deposited on the holder is equal to $P_{continuous} = 0.295 \ \frac{\mathrm{W}}{\mathrm{cm}^2}$, in order to guarantee the same energy deposition of the pulsed case. The maximum temperature reached on the samples is shown in Fig. 3.9(c). The four temperature marked on the graph are reached at time corresponding to the irradiating fluence, and the curves for different materials are overlapped.

Structural analysis

The beam energy deposition induces thermal stresses in the samples, and their structural integrity is therefore controlled before the experiment. During the particle irradiation in this experiment, thermal stresses arise from a temperature gradient along the material and from the constrains imposed by the clamp.

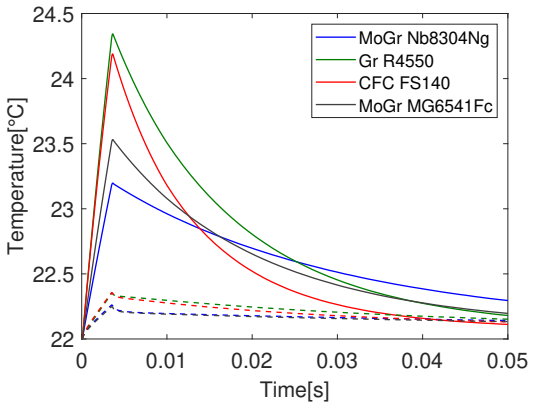

(a) Temperature increase after the first pulse induced on the different materials. The continuous line is representing the platelets samples, while the dashed line correspond to the disk samples.

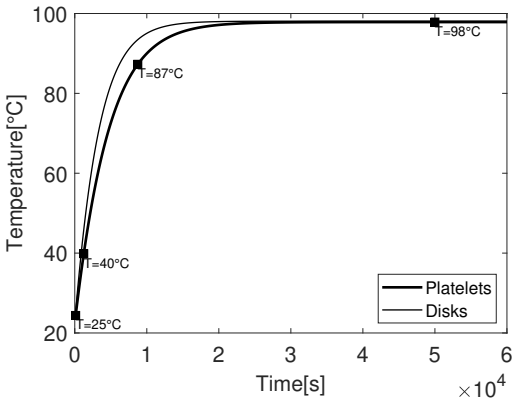

(b) Temperature evolution as function of time for the platelet and disk samples. The four points marked on the graph represent the temperatures reached at a time corresponding to the four irradiation fluences.

Figure 3.8: Average temperatures reached on the samples.

Two design cases must be considered:

- The increase of temperature provoked by a single pulse
- The steady-state increase of temperature

In both cases, the thermal and structural problem are solved sequentially. In the first case, the energy is deposited during the beam pulse, which lasts 3.5 ms. It is important to understand if, during this period, the dynamic effects due to inertia can be neglected or if the heating is too fast and the material cannot expand, and pressure waves are generated. The periods of the axial (T_z) and the radial waves (T_r) in the tested samples are shown in Tab. 3.8. Their periods are significantly smaller compared to the duration of the heat deposition, therefore, the phenomenon is modeled as a slow-transient heating [60].

	Disk [μs]		Platelet [μs]	
	T_z	T_r	T_z	T_r
MoGr Nb8304Ng	1.43	1.98	0.29	3.96
Gr R4550	0.79	3.96	0.12	7.91
CFC FS140	1.55	1.73	0.23	3.46
MoGr MG6541Fc	1.43	1.74	0.21	3.48

Table 3.8: Calculated periods of axial and radial waves for the different materials irradiated.

The system is mainly subjected to compression in the direction orthogonal to the basal planes, but a triaxal state of stresses arises in some points. In Fig. 3.9, the distributions of the directional stresses along the three axis are shown. The basal planes of MoGr are parallel to the yz plane.

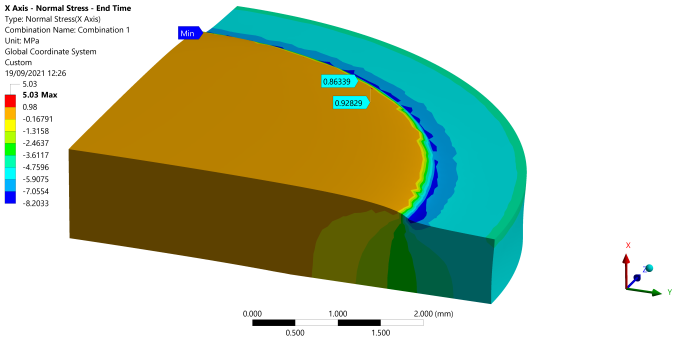

(a) σ_x.

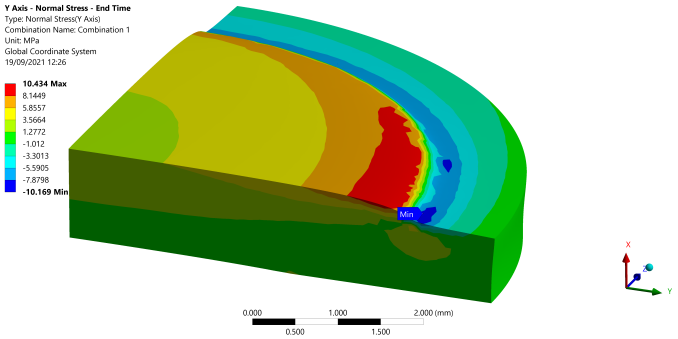

(b) σ_y.

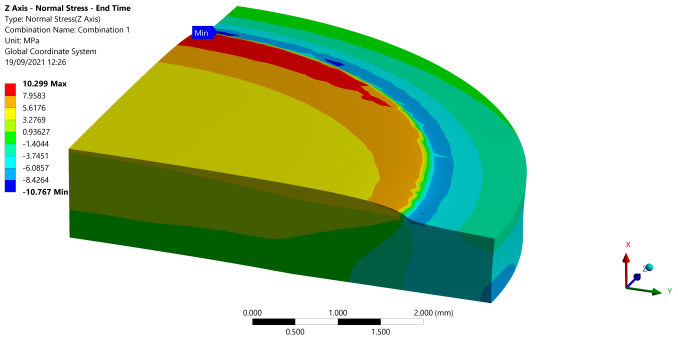

(c) σ_z.

Figure 3.9: Directional stresses in MoGr disk.

The resistance of graphite-based materials perpendicular to the basal plane is much higher under compression than under tension [130]. For this reason, the maximum directional stresses are reported. In Fig. 3.10(a), the stress condition generated in disks by a beam pulse is presented. As a comparison, two conditions are presented:

- The stresses induced by the clamping (only mechanical stresses)
- The linear combination of the mechanical stresses and the thermal stresses induced by the beam.

In this case, the contribution of thermal stresses is negligible, and the load is mainly related to the assembly procedure of the samples.

If the steady-state temperature is considered, the contribution of thermal stresses becomes relevant, as shown in Fig. 3.10(b).

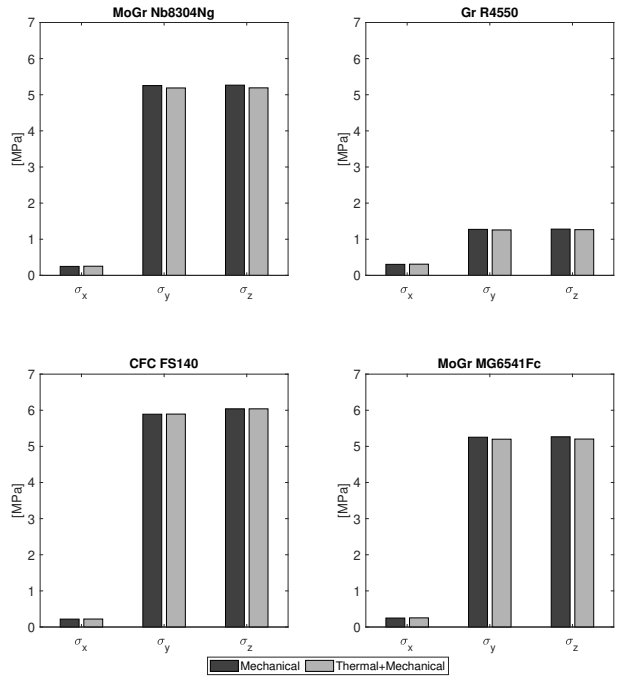

(a) Heat pulse load.

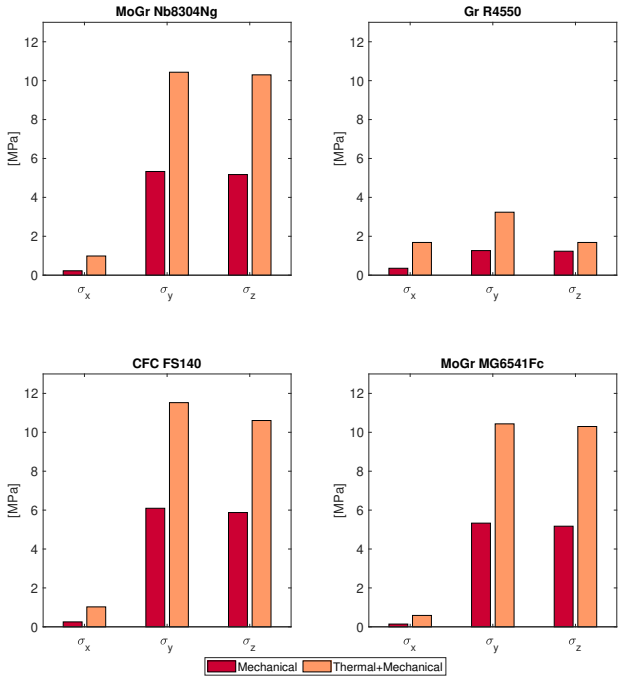

(b) Steady state heat load.

Figure 3.10: Maximum directional stresses along the three axis for disk samples. The contribution of the mechanical loads and the combination with the thermal stresses are shown.

Similar considerations applies for thin samples, those stresses are represented in Fig. 3.11. These samples suffer lower stresses compared to disks.

In both cases, the maximum normal stresses are below the maximum strength under tension, as shown in Tab 3.9.

	$\sigma_{x,max}$ [MPa]	$\sigma_{y,max}$ [MPa]	$\sigma_{z,max}$ [MPa]
MoGr Nb8304Ng	10	75	75
Gr R4550	60	60	60
CFC FS140	9	155	110
MoGr MG6541Fc	11	80	80

Table 3.9: The maximum strength under tension for each material.

The safety factors for the system with disk samples at the maximum temperature, which is subjected to higher stresses, are reported in Tab 3.10.

For isotropic graphite, the Rankine criteria is used. For all the other non-isotropic materials, the maximum stress failure theory is extended according to the Jenkins' theory [131]. The safety factors are thus calculated for all the stresses required by the theory, but only the most critical value is reported. The acceptable values for shear stresses of the materials are not known, and a conservative approach to consider equal to the acceptable stress under tension along the x axis is used.

Material	Type	Safety factor
MoGr Nb8304Ng	τ_{yz}	2
Gr R4550	σ_C	15
CFC FS140	τ_{xz}	2
MoGr MG6541Fc	τ_{xz}	2

Table 3.10: Safety factors of disk samples when subjected to steady state heat load.

The samples are thus not expected to experience a failure due to thermal stresses. Other mechanisms related to radiation-induced defects are not considered, and they may contribute to the material failure.

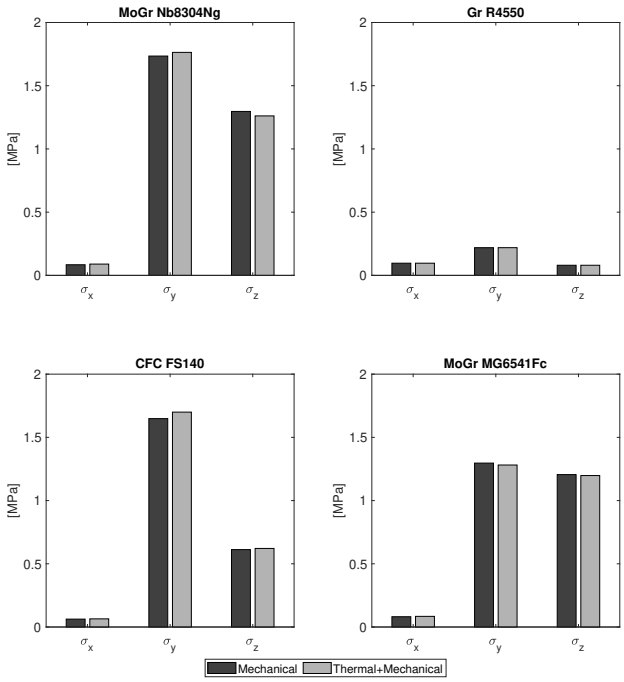

(a) Heat pulse load.

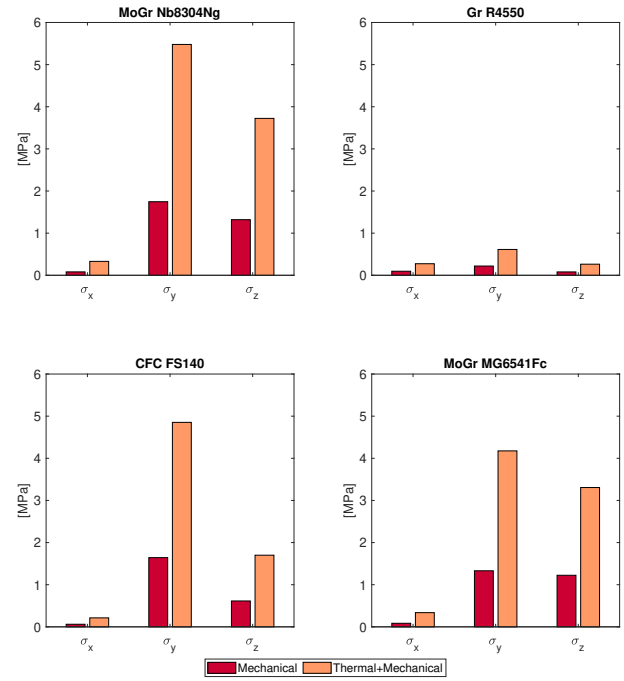

(b) Steady state heat load.

Figure 3.11: Maximum directional stresses along the three axis for platelet samples. The contribution of the mechanical loads and the combination with the thermal stresses are shown.

Chapter 4

Experimental characterization techniques

This chapter discusses the measurement techniques adopted to characterize the materials of interest before and after the irradiation test. The experimental set-ups and the theoretical backgrounds are presented. The analytical models and processing procedure implemented in the analysis are also reviewed.

4.1 Electrical resistivity

The electrical resistivity of the samples is measured with the 4-probes method [132]. The custom-built measurement set-up is composed by a power supply connected to two copper electrodes and a voltmeter connected to two probes. In order to improve the electrical contact with the sample, a soft and conductive material (adhesive electromagnetic shielding gasket) is placed on the copper electrodes [133].

A current I is applied to the copper electrodes and the voltage drop V is detected with two probes, placed at a distance d. Being the voltage drop measured across the inner part of the sample, the contact resistance between the sample and the electrode does not contribute to the measured value [132]. The sample resistivity is obtained with Eq. 4.1:

$$\rho = \frac{V}{I}\frac{wt}{d} \tag{4.1}$$

where w the width of the sample and t its thickness.

For thick samples, the current can be applied between parallel surfaces, while for thin films a different design is used, applying the electrodes directly on the top surface, as shown in Fig. 4.1.

The set-up represented in Fig. 4.1(b) is suitable for measuring conductive films on insulator. The current is, indeed, flowing only in the film, and its resistivity is measured. When the substrate material is conductive, the same configuration is adopted, but the thickness of the substrate is reduced. Conductive coatings on conductive substrates are, in fact, modelled as two layers of parallel resistors composed by the resistance of the substrate R_{bulk} and the resistance of coating

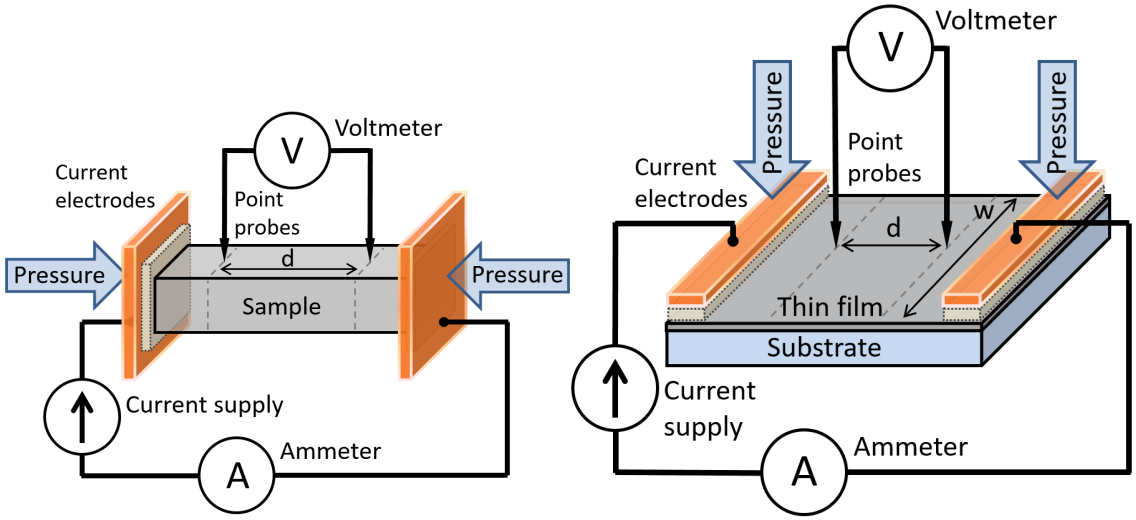

(a) Application to thick sample.

(b) Application to thin film sample.

Figure 4.1: Electrical resistivity measurement set-ups [133].

$R_{coating}$, as shown in Eq. 4.2:

$$R_{parallel} = \frac{R_{bulk}\, R_{coating}}{R_{bulk} + R_{parallel}}, \tag{4.2}$$

The R_{bulk} is measured before coating the samples, and the coating resistivity $\rho_{coating}$ is then obtained from Eq. 4.12:

$$\rho_{coating} = \frac{R_{bulk}\, R_{parallel}}{R_{bulk} - R_{parallel}} \frac{w\, t_{coating}}{d}, \tag{4.3}$$

with $t_{coating}$ the coating thickness.

The model is valid if the current flows in both of the two layers, thus implying a comparable level of the two resistances. For thin films, the resistance increases because of the small transverse cross-section. In Tab 4.1, the expected resistance ratio between a MoGr substrate and Mo coating are shown as a function of the bulk thickness [127]. It is therefore evident that the maximum allowable substrate thickness to detect the coating resistivity is in the order of hundreds of microns.

Substrate thickness [mm]	R_{bulk} [Ω]	$R_{coating}/R_{bulk}$
5	0.0003	46
1	0.0014	9
0.15	0.0093	1

Table 4.1: Ratio of Mo coating to MoGr bulk resistance in function of the bulk thickness. These values are calculated assuming a Mo coating with a thickness of 6 μm and a resistivity of 55 nΩm. The considered MoGr resistivity is 1000 nΩm [127]

.

The thickness of the samples is measured with a non-contact optic method, with a resolution of 1 μm. The average dimension is considered for the resistivity

calculation. The thickness of the coating is considered the nominal one, with a resolution of 0.1 μm, according to the calibration data supplied by the coating company. Several microscopic observations have been performed on the coating, and an uncertainty of about 5% has been detected for its thickness.

4.1.1 Application to irradiated samples

A similar approach is used to study ion-irradiated samples. The ion beam is, in fact, stopped within the sample thickness and the maximum penetration depth is calculated with FLUKA simulations, as explained in 3.4.3. The irradiated samples are therefore considered as a resistor composed by two parallel resistances: the irradiated layer and the unperturbed bulk. As a first approach, the irradiated volume is considered uniform, although the dpa is non constant across it. For coated samples, it is worth considering three layers: the unperturbed bulk, the irradiated layer of the substrate and the coating, as shown in Fig. 4.2.

(a) Uncoated sample (b) Coated sample

Figure 4.2: Multi-layers models for measuring the electrical resistivity of the irradiated samples.

The resistance of the unirradiated bulk is calculated according to Eq. 4.4:

$$R_{bulk\_pristine} = \frac{\rho_{bulk\_pristine}\, d}{w\,(t_{total} - t_{irradiated})} \tag{4.4}$$

where $\rho_{bulk\_pristine}$ is measured before the irradiation for every samples and $t_{bulk\_pristine}$ is the difference between the sample thickness and the thickness of the irradiated layer $t_{irradiated}$, calculated with FLUKA simulations.

For the uncoated samples, the total resistance $R_{parallel}$ is measured, and the resistance $R_{bulk\_irradiated}$ and the resistivity $\rho_{bulk\_irradiated}$ of the irradiated layer are obtained with Eq. 4.5 and 4.6:

$$R_{bulk\_irradiated} = \frac{R_{parallel}\, R_{bulk\_pristine}}{R_{bulk\_pristine} - R_{parallel}} \tag{4.5}$$

$$\rho_{bulk\_irradiated} = R_{bulk\_irradiated} \frac{w\, t_{irradiated}}{d} \tag{4.6}$$

For coated irradiated samples, both the coating resistivity and the resistivity of the irradiated substrate are unknown. It is therefore important to define a bulk resistivity increase factor ρ_X, as shown in Eq. 4.7:

$$\rho_X = \frac{\rho_{bulk\_irradiated}}{\rho_{bulk\_pristine}} \tag{4.7}$$

For a given fluence or dpa, ρ_X is known from the irradiated uncoated samples measurement. At this point, it possible to calculate the irradiated and unirradiated bulk resistance and their parallel resistance, as shown in Eq. 4.8, 4.9, 4.10:

$$R_{bulk\_pristine} = \frac{\rho_{pristine}\, d}{w\,(t_{total} - t_{irradiated})} \tag{4.8}$$

$$R_{bulk\_irradiated} = \frac{\rho_x\, \rho_{pristine}\, d}{w\, t_{irradiated}} \tag{4.9}$$

$$R_{bulk\_parallel} = \frac{R_{bulk\_irradiated}\, R_{bulk\_pristine}}{R_{bulk\_pristine} + R_{bulk\_irradiated}} \tag{4.10}$$

At this point, the only unknown is the coating resistance and its resistivity, that are calculated with Eq. 4.11 and 4.12

$$R_{coating} = \frac{R_{bulk\_parallel}\, R_{parallel}}{R_{bulk\_parallel} - R_{parallel}}. \tag{4.11}$$

$$\rho_{coating} = R_{coating} \frac{w\, t_{coating}}{d} \tag{4.12}$$

The main limitation of this method is that it relies on a parallel resistor model, which becomes inappropriate when one of the resistances grows much over the values of the other layers in the model. As the irradiated layers resistivity increases, the difference between $R_{bulk\_pristine}$ and $R_{parallel}$ in Eq. 4.5 becomes very small and it is then difficult to measure. The systematic uncertainty is calculated by combining the standard uncertainties of all the parameters involved in the calculation (e.g. voltage, current, dimensions,etc.), as recommended in [134]. The relative uncertainty of the irradiated resistivity is lower than 30% if the resistivity increase factor ρ_X remains below 3. For higher values, the uncertainty rapidly increases, but it should be considered that it may become also wrong the assumption that the current is flowing in both layers. The uncertainty on the resistivity of the irradiated coating is about $15 - 30\%$, depending on the bulk material.

4.2 Density

The density of the material is an important input for FLUKA simulation in order to calculate the ion penetration depth, as shown in 3.4.3 . It is calculated with the ratio of the sample weights and their volumes, obtained by measuring the three dimensions.

4.3 Raman spectroscopy

The Raman spectroscopy is a widespread technique to characterize microstructural changes, and it is thus applied to investigate the microscopic evolution of graphitic materials under irradiation. In this section, the main features of the technique are reviewed.

The Raman effect is classified as a light scattering phenomenon. When a Rayleigh scattering event occurs, the interaction of the electromagnetic radiation with matter

is elastic, and the scattered radiation is detected at the same energy of the incoming light. Raman events are instead inelastic scattering of light, and different energy components are detected in the scattered beam.

The intensity of the Raman scattering is typically 10^{-8} with respect to the incident light. For this reason, the deployment of this technique is inherently related to the development of high intensity light sources such as lasers [135].

From a quantum-mechanics point of view, the light scattering process is described as a two-photon process. An incoming photon is absorbed by the crystal lattice, which is promoted to a virtual energy state with an infinitesimally short time. When a transition from this virtual state occurs, a photon is emitted. For a Rayleigh scattering, the system comes back to the ground state, and the emitted photon has the same energy of the absorbed one. When the final state is an excited state, the photon transfers some energy to the system, and it is emitted at a lower energy. In some cases, the system belongs to an exited state, and it comes back to the ground level after emitting a higher energy photon. The last two cases are both considered as Raman scattering, and they are respectively called Stokes and Anti-Stokes signal [135–137]. The transitions corresponding to the different phenomena are illustrated in Fig. 4.3.

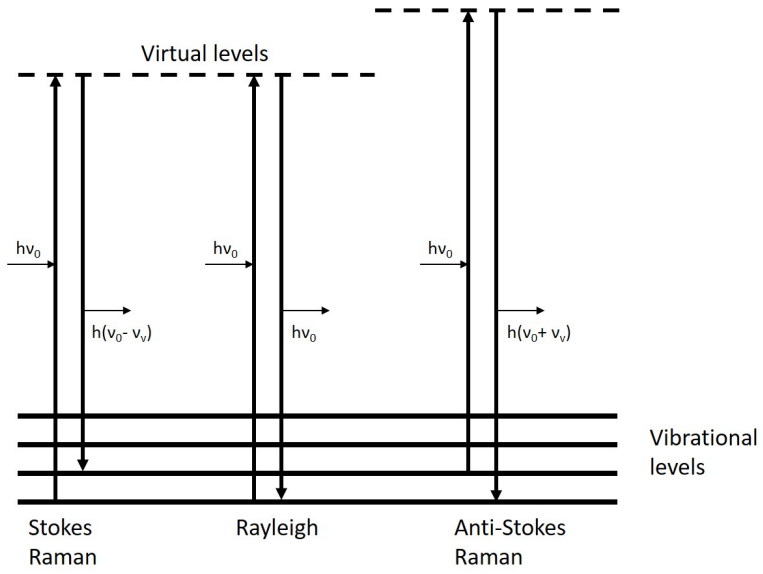

Figure 4.3: Representation of the energy level transitions in the different scattering phenomena. Modified from [135].

In Raman spectroscopy, the transitions described in Fig. 4.3 refer to quantized vibrational states. The quantum of lattice vibration is called phonon, in analogy with photon for the electromagnetic field. The phonon energy is expressed as shown in Eq. 4.13:

$$E_{phonon} = h\nu_{phonon} \tag{4.13}$$

where ν_{phonon} is the frequency of the normal mode represented by the phonon, and h is the Plank's constant. A transition between the vibrational states can be regarded as a creation (Stokes) or annihilation (Anti-Stokes) of a phonon [138]. For

the conservation of energy, the energy of the emitted photon is lower or greater of an amount corresponding to the energy of the phonon involved in the scattering process.

The photon energy E_{photon} is also proportional to its frequency ν_{photon}, as shown in Eq. 4.14:

$$E_{photon} = h\nu_{photon} \tag{4.14}$$

The energy change of the scattered photon is therefore detected as a frequency shift.

The Raman spectra is the collection of intensities of the scattered light as a function of the frequency shift. It is often represented as a shift of wavenumber [136], which is simply defined as shown in Eq. 4.15:

$$\tilde{\nu} = \frac{\nu}{c} \quad [cm^{-1}] \tag{4.15}$$

where c is the speed of light.

Raman spectra collect information on the elementary lattice vibrations of a system, and it therefore represents a fingerprint of the tested material, but it is also sensitive to the crystalline structure [136].

It is important to mention that not all the vibrations are active for Raman spectroscopy. The transition between the initial and final energy level of the molecules must, in fact, respect the quantum-mechanical selection rules. These criteria are deducted from the conservation laws of energy and momentum, and the symmetry rules of the crystal lattice [139]. The general condition for the detection of a mode with Raman spectroscopy is that the polarizability of the system must change during the vibration [140].

The next section focuses on the interpretation of the Raman spectra for graphitic materials, which are relevant for this work.

4.3.1 Raman spectra of graphitic materials

The Raman spectra of graphite is characterized by a limited number of well-defined peaks. If a green laser with an excitation wavelength of 514.5 nm is used, the resulting spectra is composed by the following peaks [141–144]:

- The D band at $\approx 1350\ cm^{-1}$
- The G band at $\approx 1580\ cm^{-1}$
- The D' band at $\approx 1620\ cm^{-1}$
- The 2D band at $\approx 2700\ cm^{-1}$
- The 2D' band at $\approx 3250\ cm^{-1}$

On the top of these, other bands are observed at $\approx 2450\ cm^{-1}$ and $\approx 2950\ cm^{-1}$.

The visualization of these modes is related to the graphite crystal structure, which allows understanding its light scattering properties.

A graphite crystal is simply an AB stacking of hexagonal planes of carbon atoms. The in-plane bonds of carbon atoms are characterized by strong covalent bonds, which lead to excellent thermal and electrical properties. The links between planes

are formed by weak van der Walls interaction, resulting in a strong anisotropic behaviour of graphite crystals [145]. The graphite crystallographic structure is represented in Fig. 4.4. The unit cell, shown in red, is composed by four atoms.

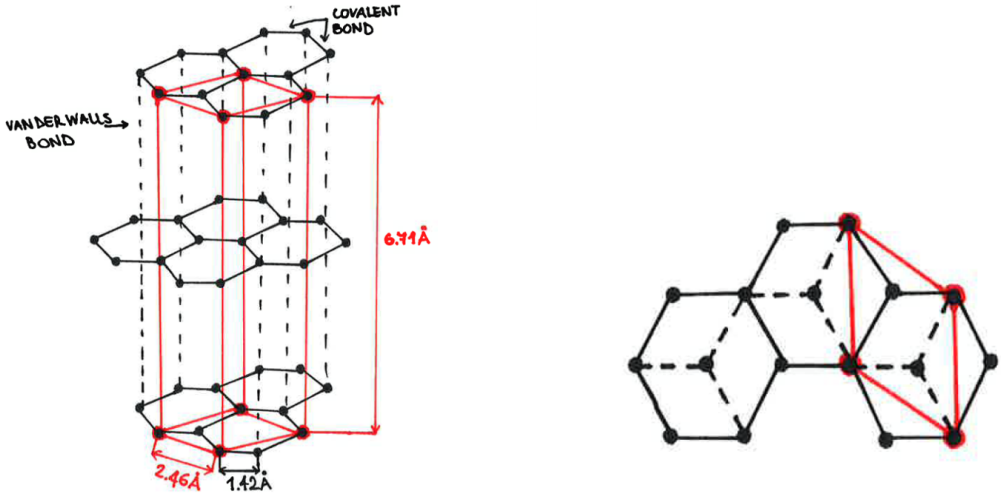

(a) 3D view of the graphite crystal structure. (b) Top view of the graphite crystal structure.

Figure 4.4: Graphite crystal structure.

With four carbon atom in the unit cell, graphite is characterized by three acoustic and nine optic branches, whose phonon dispersion relations are shown in Fig. 4.5 for the high symmetry points of the first Brillouin zone (BZ) [139].

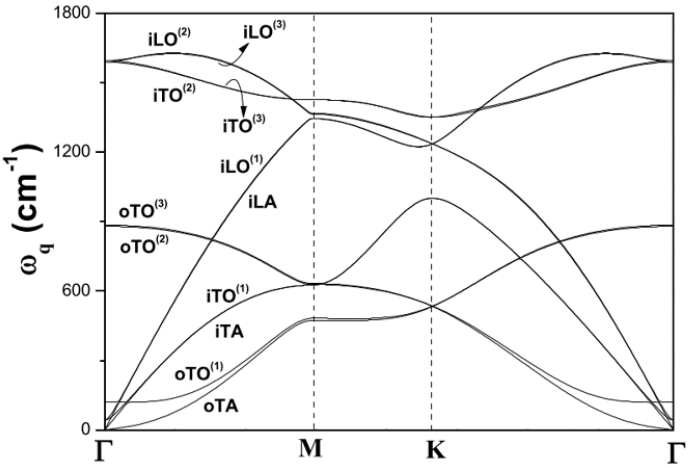

Figure 4.5: Phonon dispersion relations in the BZ [139].

The G peak detected at $\approx 1582\ cm^{-1}$ corresponds to a doubly degenerate (iTO and LO) optical phonon mode at the center of the BZ (Γ). This mode clearly identifies the in-plane bond stretching of sp^2 bondings [143] and it is represented in Fig. 4.6(a). For perfect crystal, only phonons with a wave vector $q \approx 0$ respect the momentum conservation for inelastic scattering of visible light. When defects are

present, this rule is relaxed and other modes become active. The D band is indeed related to the disorder in the graphite crystal. It comes from LO phonons around the K point of the BZ and it is linked to a double-resonance process involving electronic transition [142]. This mode represented in Fig. 4.6(b) is the breathing of sp^2 bonds. The ratio of the intensity of the D peak relatively to the G band I_D/I_G is related to the crystallite size [146].

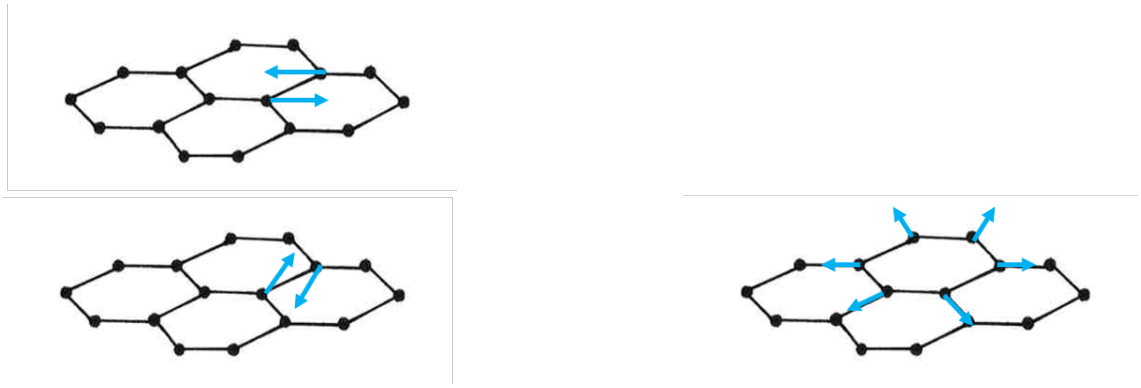

(a) In-plane bond stretching of sp^2 bondings.

(b) Breathing of sp^2 bondings.

Figure 4.6: Graphite modes corresponding to the G and D bands in Raman spectrum of graphite. Modified from [143].

The aforementioned first-order peaks are related to the in-plane crystalline order.

For graphite, it is also important to consider higher-order processes, where two or more phonons are involved in the scattering [138]. In the second order spectrum, a significant peak is indeed detected at $\approx$ 2700 cm^{-1}. This peak represents the so-called 2D band, as it is the overtone of the D peak. This band is present also for perfect graphite and it is not activated by defects, as in a two-phonon process the momentum conservation does not require $q \approx 0$ [139].

The shape of this band is however related to the disorder perpendicular to the basal planes of the graphite crystal. The 2D band is indeed modelled by a single peak centered at $\approx$ 2700 cm^{-1} for turbostratic graphite, where the stacking order of the basal planes is not respected. This structure is typically characterized by an interlayer distance greater than 0.342 nm, while for crystalline graphite this quantity is almost 0.335 nm [141]. The resulting interaction between basal planes is weaker, and structure resembles the one of graphene (or 2D graphite). When two graphene layers stacked in the correct AB sequence are measured, four Lorentzian peaks are used to model the 2D band. As the number of layers increases, the band shape approaches the one of 3D graphite, where two Lorentzian peaks form the 2D band. The peaks are named 3DA and 3DB (or 2DA, 2DB) and for perfect stacking their intensity ratio is 0.5 [147]. If their ratio is higher than 0.5, it means that a third peak could be ideally used for the fitting. This peak is centered at $\approx$ 2700 cm^{-1}, and it represents the contribution of turbostratic graphite. It is therefore an intermediate situation, where the volume of graphite investigated by Raman spectroscopy can be partially made of 2D and 3D graphite. [147]. The changes of 2D Raman band of graphite when passing from turbostratic graphite to perfect 3D graphite is represented in Fig. 4.7.

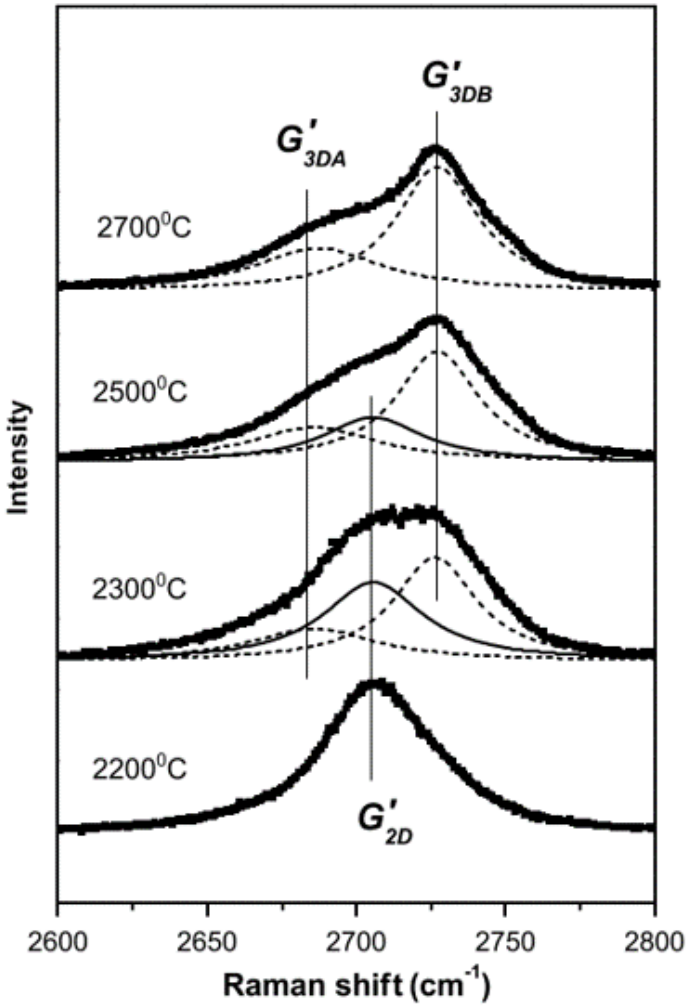

Figure 4.7: Fitting of the 2D band of graphite, as a function of the thermal treatment temperature. For high temperature, the band is fitted by only two peaks (3DA and 3DB). As the temperature decreases, the contribution of turbostratic graphite increases, and a third peak is needed for the fitting. For completely turbostratic structure, a single peak fits the curve [147].

4.3.2 Experimental parameters

The spectra presented in this work are obtained with a Renishaw InVia spectrometer in back-scattering geometry. A green laser with a wavelength of 514.5 nm and a power of 10 mW is focused on the samples with a microscope lens at 50x. The collected light is filtered from Rayleight scattering, and the Raman components are analysed with a diffraction grating and a Charge Couple Device (CCD). The duration of the accumulation is set to 10 s and 1-3 accumulations are performed on the same point. The instrument is calibrated with Si before each use.

The samples used for this measurement are the disk ones. For each sample, five spectra are measured in different positions. The background is subtracted to these spectra before doing an average of the five points. The resulting spectrum is then fitted to extract the relevant parameters to understand the disorder of the graphite structure. The details of the Matlab code developed for the fitting procedure is

detailed in Ap. B.

4.4 Thermal annealing

After the ion irradiation and the post-irradiation examination, the graphitic samples are thermally treated at different temperatures to investigate the microstructural evolution of the irradiated crystals.

When the temperature allows overcoming the *activation energy* Q for defect diffusion, they become mobile and they interact between themselves, as explained in 1.3. In particular, vacancies and interstitials can either recombine or migrate to crystal boundaries, where they self-annihilate. The diffusion of defects can, however, also facilitate their clustering. The effect of annealing is therefore not unique, but it is related to the quantity and the structure of defects present after irradiation, and hence to the irradiation conditions [148].

If the defects annihilation is relevant, a recovery of the initial crystal order is possible. Raman spectroscopy is sensitive to lattice defects concentration, as explained in 4.3.1, and it is therefore adopted to investigate the defect annealing. The ratio I_D/I_G is analysed to study the concentration of defects [149].

4.4.1 Experimental parameters

The annealing is performed in a tubular ceramic oven, connected to a pumping system that ensure a pressure of about 10^{-5} mbar. The heating ramp is set to 4 °C/min and the maximum temperature is kept for 30 minutes before starting the cooling. A Raman analysis is performed after each thermal treatment. The investigated temperatures range goes from 100°C to 350°C. A summary of the annealing treatment is given in Tab. 4.2.

Maximum temperature [°C]	Dwell [min]	Heating rate [°C/min]
100	30	4
150	30	4
200	30	4
250	30	4
350	30	4

Table 4.2: Summary of annealing parameters.

The same procedure is implemented on samples irradiated at different fluences, in order to assess potential differences in the defect produced at different dpa levels.

4.5 Focused ion beam-scanning electron microscope

For the investigation of the coating microstructure, a Zeiss Crossbeam 540 Focused Ion Beam-Scanning Electron Microscope (FIB-SEM) is adopted. The equipment consists of a column for Ga^+ ions and a column for field emissions of electrons.

The SEM operates with a typical accelerating voltage of 5-10 kV, an aperture size 30-120 μm, and a working distance of 4-15 mm. An In-Lens Secondary Electron Detector is used to obtain topological information of the top surface of the samples.

Ga^+ ions are focused on the material surface with currents from 1.5 nA to 15 nA to mill parts of the volume. The investigation of the interface between the coating and the substrate requires a removal of a volume of around $20 \times 15 \times 7$ μm^3. SEM images of the milled area are acquired with an external secondary electron detector (SESI). For unirradiated samples, a platinum (Pt) layer is applied to avoid surface damage. Pt was not applied on the irradiated samples, to avoid its detection in further test.

Chapter 5

Pristine material characterization

In this chapter, the characterization of the materials before irradiation is presented. Each sample is characterized before irradiation for a precise comparison with the irradiated properties. Some of the materials tested are not developed and produced specifically for HL-LHC collimators, and their properties are characterized for the first time. The knowledge of the main features of different materials is also important to understand their response to radiation damage.

5.1 Graphite-based materials

This section is dedicated to the characterization of the relevant properties of uncoated samples. All the graphite-based materials relevant for this work are therefore characterized: MoGr Nb8304Ng, polycristalline isotropic graphite R4550, CFC FS140, and MoGr MG6541Fc.

5.1.1 Electrical resistivity

The electrical resistivity is a key properties for the correct operation of collimators, as explained in 2.3.4. In Tab. 5.1, the average values of electrical resistivity ρ of the four materials under study is reported. The presented results refer to the platelet samples before being irradiated, with a thickness of $\approx 150 - 200\ \mu m$. As a comparison, the electrical resistivity of the same materials measured on thicker samples ρ_{bulk} is reported [127]. The highest deviation from the values measured for thick samples is registered in the case of CFC. This behaviour is ascribed to the small size of the sample compared to the size of the pores in the material, which can be in the order of hundreds of micrometers. The current flow may be hindered by pores crossing through the whole thickness and reducing the effective cross section, and it increases the resistivity. For the other materials, the deviations between the two techniques can be related to the inhomogeneity of the block from which it is cut. If the samples are indeed obtained from a denser and more compact area, this would result in a lower electrical resistivity with respect to the bulk measurement.

The lowest resistivity of MoGr is ascribed to the production process, and to the catalytic graphitization achieved with the presence of Mo during the sintering process, as explained in Sec. 2.4.3. The MoGr grade Mg6541Fc shows a lower resistivity compared to the other grade, thanks to the higher sintering temperature.

Material	ρ [n$\Omega \cdot m$]	ρ_{bulk} [n$\Omega \cdot m$]	$\mid \rho - \rho_{bulk} \mid / \rho[\%]$
MoGr Nb8403Ng	1272±155	1390	9
Gr R4550	11085±358	12600	14
CFC FS140	10687±604	8200	23
MoGr Mg6541Fc	956±51	962[1]	0.6

[1] This value refers to eddy current measurement with a commercial Sigmatest, as no DC measurement are available [133].

Table 5.1: Electrical resistivity of uncoated material before irradiation for platelets (ρ) and thick samples (ρ_{bulk}).

5.1.2 Raman spectroscopy

All the irradiated samples are characterized before and after irradiation to emphasize the evolution of the microstructure induced by the ion beam. Raman spectroscopy is performed only on the graphitic surfaces and not on the coated ones, because metals do not give a signal [150].

Fig. 5.1 shows the spectra of all the samples characterized: MoGr Nb8304Ng, polycristalline isotropic graphite R4550, CFC FS140, and MoGr Mg6541Fc. Six samples for each material are selected. It is important to notice that the differences between samples of the same material mainly regard the intensity of the D peak. This parameter is strongly related to the microstructure evolution under irradiation, and it is therefore important to know its value for each of the samples before testing.

The main features characterizing the materials are, however, similar for the set of investigated samples. For this reason, the average spectrum of each material is considered for the microstructural analysis, as represented in Fig. 5.2. It is possible to observe that the spectra reflect what is expected for graphite-based materials, as all the peaks are theoretically predicted, as explained in 4.3.1. The main peaks and their average peak positions are presented in Tab. 5.2, and compared to the value predicted in literature.

Material	x_D [cm^{-1}]	x_G [cm^{-1}]	$x_{D'}$ [cm^{-1}]	x_{2D} [cm^{-1}]	$x_{2D'}$ [cm^{-1}]
MoGr Nb8403Ng	1353	1581	1622	2693-2729	3248
Gr R4550	1352	1581	1621	2709	3247
CFC FS140	1352	1580	1621	2710	3247
MoGr Mg6541Fc	1351	1580	1621	2692-2728	3247
Literature [141–144]	1350	1580	1620	2700	3250

Table 5.2: Average peak positions of the Raman spectra for the analysed samples and expected values in literature for graphite-based materials.

MoGr grades do not show any additional peaks compared to pure graphite. MoC are, in fact, not active for Raman spectroscopy [151]. TiC are instead visible in Raman spectra [152], but the small quantity of Ti added is not detected, as shown also elsewhere by means of X-ray diffraction [103]. The Raman spectra allows therefore a comparison of the graphite matrix, which is influenced by the different production routes of the materials.

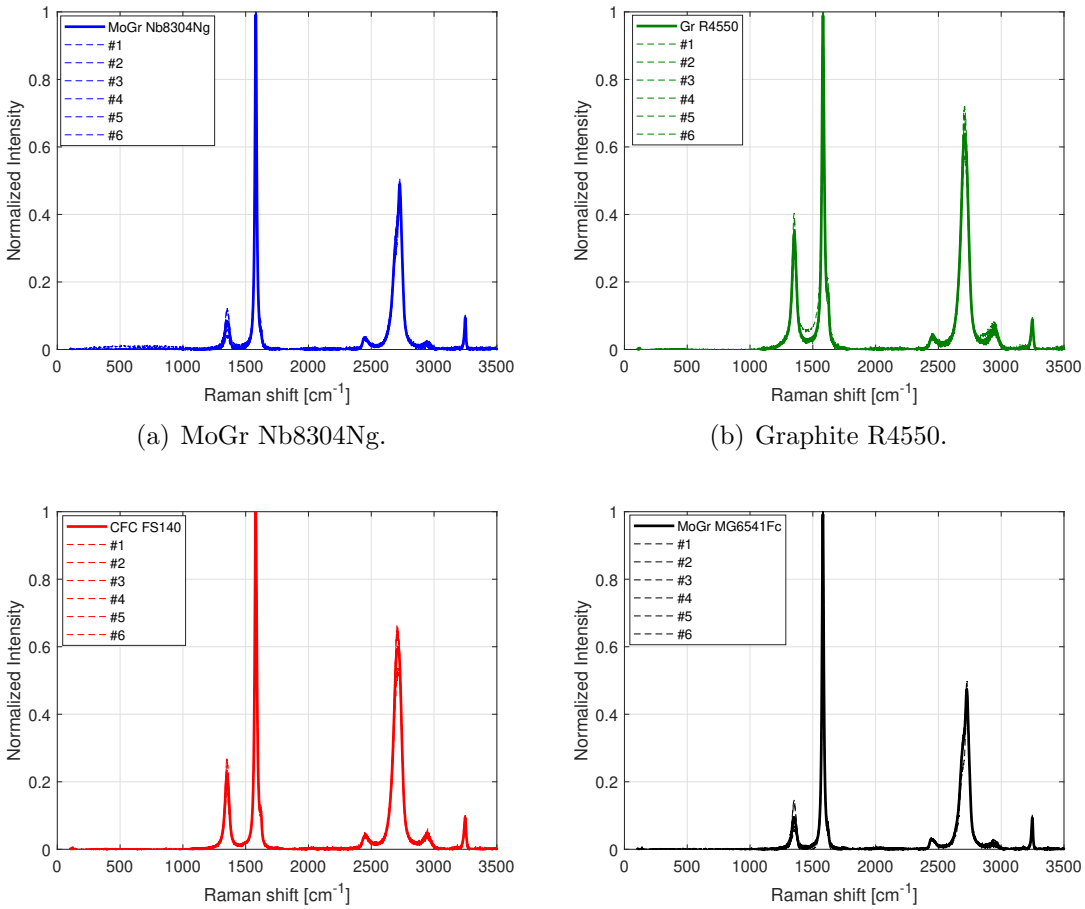

(a) MoGr Nb8304Ng.

(b) Graphite R4550.

(c) CFC FS140.

(d) MoGr Mg6541Fc.

Figure 5.1: Raman spectra of all the analysed set of samples for the different materials.

The first order Raman spectrum, between $\approx 1200-1700$ cm^{-1}, contains some interesting information regarding the graphitization level of the materials. In Fig. 5.3(a), the intensity ratio of the D peak with respect to the G peak I_D/I_G is reported for the different materials. The error bars refer to the scattering observed between the set of tested samples. It is possible to observe that MoGr grades are similar between them, and they are characterized by a lower intensity of the D peak with respect to Gr and CFC. This parameter indicates that a higher structural order is reached along the basal planes of MoGr [141, 143].

A coherent information comes from Fig. 5.3(b), where the full width at half maximum (FWHM) of the G band is represented. The two MoGr grades present narrower peaks, which correspond to a higher graphitization level [153].

The information derived from the first order peak fitting are used to calculate the crystallite size L_a in graphite. In particular, the ratio of the integrated intensities (i.e. the areas) A_D/A_G is proportional to the crystallite size, as shown in Eq. 5.1 [154].

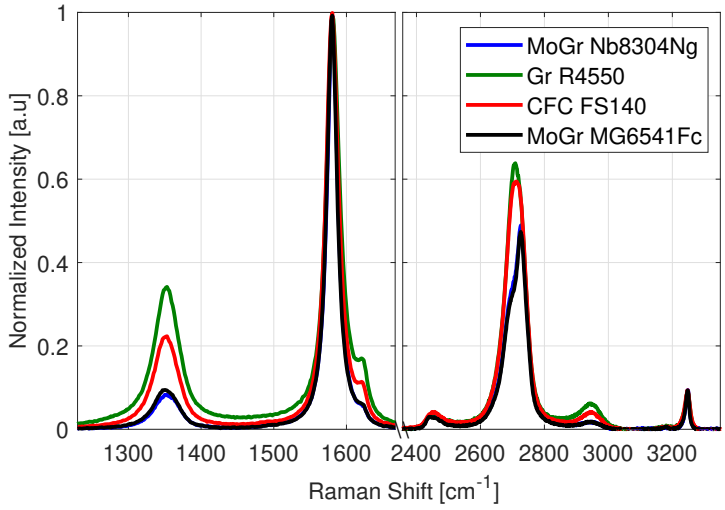

Figure 5.2: Average Raman spectra before irradiation of the four material tested.

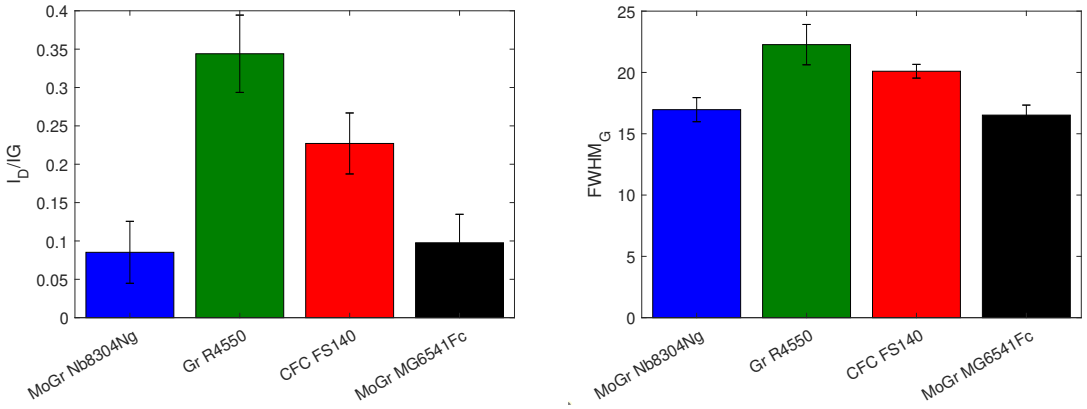

(a) Average intensity ratio between D and G peaks .

(b) Average FWHM of the G peak.

Figure 5.3: Parameters obtained from the first order spectra of the different materials.

$$L_a[nm] = (2.4 \cdot 10^{-10})\, \lambda_l^4 \left(\frac{A_D}{A_G}\right)^{-1}, \tag{5.1}$$

where λ is the wavelength of the laser light in nm.

In Tab. 5.3, the crystallite sizes of the four materials under study are reported.

The MoGr grades are characterized by bigger crystallite size, despite the higher scattering of the results. This condition is reached thanks to the catalytic graphitization of Molybdenum during the production process [133]. The L_a obtained with this formula are however lower with respect to the typical values obtained with XRD on MoGr, which range between 240-320 nm [103]. The intensity of the D peak also points to a higher order in CFC graphite matrix compared to isotropic graphite.

Material	La [nm]
MoGr Nb8403Ng	125±64
Gr R4550	27±3
CFC FS140	42±7
MoGr Mg6541Fc	97±34

Table 5.3: Crystallite size of the materials tested obtained from Raman spectra and using Eq. 5.1.

The D peak intensity is fed, however, by any defect that breaks the symmetry of C-networks along the basal plane [155]. A possible parameter adopted to understand the type of defect is the ratio between the intensity of the D peak and the one of D'. Three different type of defects are identified by the $I_D/I_{D'}$ ratio [155]:

- $I_D/I_{D'}$ is maximum (≈ 13) for defects associated with sp3 hybrization,
- $I_D/I_{D'}$ is ≈ 7 for vacancy-like defects,
- $I_D/I_{D'}$ is ≈ 3.5 for grain boundaries.

Tab. 5.4 reports the values of the $I_D/I_{D'}$ for the materials characterized. It is possible to observe that the two MoGr grades are characterized by higher values of the $I_D/I_{D'}$ ratio, which are therefore related to vacancy-like defects. This can explain why the average crystallite sizes found in MoGr are lower with respect to the measurement done with XRD. The vacancy-like defects responsible for the increase of the D peak intensity do not allow the determination of the MoGr crystallite sizes, which are underestimated. The D peak in graphite and CFC is instead related to grain boundaries and the estimation of their crystallite size by means of the I_D/I_G ratio is reliable.

Material	$I_D/I_{D'}$
MoGr Nb8403Ng	7.5
Gr R4550	3.3
CFC FS140	3.9
MoGr Mg6541Fc	6

Table 5.4: Intensity ratio of the D peak with respect to the D' for the tested materials.

The higher degree of graphitization of the MoGr grades is also evident from the second order band. In Fig. 5.4(a), the 2D band of one representative sample of MoGr is shown. The raw data are deconvoluted with two peaks, whose intensity ratio is shown in Fig. 5.4(b). Both materials present a peak ratio that is very close to the one expected for 3D graphite with a perfect stacking order. According to [147], this would correspond to a out-of-plane lattice parameters c equal to 0.671 nm, which corresponds to what is found with XRD [103].

For graphite and CFC, a single-peak fitting of the 2D band is used. Their out-of-plane structure is therefore turbostratic and characterized by a higher lattice parameter.

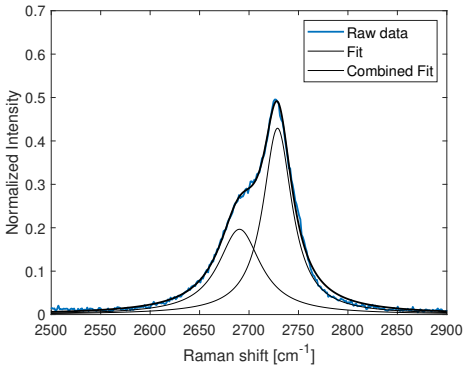

(a) Comparison of the raw data and peak fitting of the 2D band of one MoGr Nb8304Ng sample .

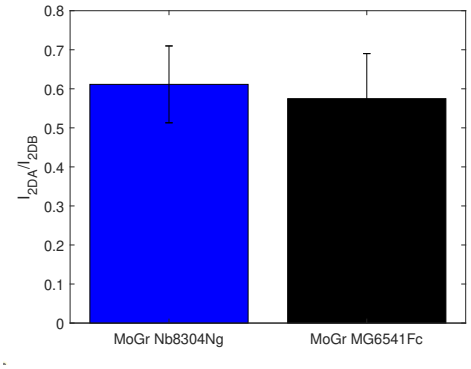

(b) Intensity ratio between the two components of the 2D band for the MoGr grades investigated in this work.

Figure 5.4: Second order peaks of MoGr grades and parameters obtained from the peak fitting.

The microstructural information extracted from the Raman spectroscopy are coherent with the observed macroscopic properties such as the electrical resistivity. The two MoGr grades show, in fact, a higher graphitization level, which reflects the lower resistivity values found. The defects detected with the spectroscopy, like vacancies or grain boundaries, are responsible for the reduction of electron mobility, and thus for the increase of resistivity [34]. The same reasoning applies to CFC and graphite: this last material is, in fact, the most disordered structure and the highest electrical resistivity. The two grades of MoGr show a similar level of order along the basal plane, as shown by the intensity of the D peak. The grade MoGr Nb8304Ng present a slightly higher crystallite size with respect to the Mg6541Fc. The electrical resistivity of the two materials indicates that the MoGr Nb8304Ng resistivity is higher. It has been shown, however, that the intensity of the D peak in MoGr can be ascribed to in-plane defects such as vacancies, and the determination of the grain size is therefore not feasible. This indicate that the electrical resistivity of MoGr is mainly influenced by the electron scattering at the grain boundaries, and not by point defects. This is coherent to what is observed for polycrystalline graphite [156].

5.2 Coatings

HL-LHC secondary collimators are coated with 6 μm of Mo to decrease their impedance. In this section, the effects of the coating production process and the substrate on the electrical properties are analysed. As a comparison, Cu coating is also analysed as an alternative for other BIDs.

5.2.1 Electrical resistivity

In Tab. 5.5 the electrical resistivities of 6 μm thick Mo coatings produced with DCMS on the four different substrates are presented. Despite the high dispersion

observed over the set of samples, it is possible to state that the measured resistivity of the Mo coating is well above the value of the Mo bulk (53.4 $n\Omega \cdot m$ [157]). It is worth mentioning that the resistivity of coating also depends on the substrate material. In particular, higher resistivities are measured for graphite and CFC. The Mo coating on CFC copies the morphology of the substrate, which is characterized by millimetric-size porosity that are not filled by the coating. These discontinuities obstacle the current flow and lead to a high resistivity value. For this reason, this option is discarded as a possible alternative to Mo-coated MoGr for HL-LHC secondary collimators.

Material	ρ [n$\Omega \cdot m$]
Mo on MoGr Nb8403Ng	120±57
Mo on Gr R4550	414±228
Mo on CFC FS140	407±83
Mo on MoGr Mg6541Fc	236±40

Table 5.5: Electrical resistivity of Mo coating produced with DCMS on four different substrates.

In Tab. 5.6, the electrical resistivities of 6 μm Mo coatings produced with HIPIMS are reported for the two substrates investigated: the polycrystalline graphite and the MoGr Nb8403Ng. A decrease of electrical resistivity is registered for both substrates. The reported values match the expected value for bulk Mo.

Material	ρ [n$\Omega \cdot m$]
Mo on MoGr Nb8403Ng	48±10
Mo on Gr R4550	56±8

Table 5.6: Electrical resistivity of Mo coating produced with HIPIMS on graphite and the MoGr Nb8403Ng substrates.

The lower electrical resistivity of coating produced with HIPIMS compared to DCMS is reported in literature [158]. This results is related to the microstructure of the coating, as discussed in Sec. 5.2.2.

In Tab. 5.7, the electrical resistivity of Cu-coated graphite and MoGr Nb8403Ng is reported. The coating is produced with HIPIMS and it is 3 μm thick. In order to increase the coating adherence, a 0.5 μm interlayer of Ti is applied. The contribution of this interlayer is included in the resistivity of copper, leading to a slightly higher value with respect to the resistivity of bulk copper(17 $n\Omega \cdot m$).

Material	ρ [n$\Omega \cdot m$]
Cu on MoGr Nb8403Ng	27±10
Cu on Gr R4550	19±1

Table 5.7: Electrical resistivity of Cu coating produced with HIPIMS on graphite and MoGr Nb8403Ng substrates.

These results obtained with a DC method are in a good agreement with the measurement performed with a resonant RF cavity. A higher resistivity value is,

however, detected for HIPIMS Mo-coated graphite. This may be related to the different geometries of the samples adopted for the analysis. The thin samples measured with the DC method, could reach a higher substrate temperature during the coating deposition, leading to a better grain aggregation [127].

5.2.2 Microstructure

The microstructure of the coating is observed before irradiation to understand the different electrical behaviour of coating and the potential impact on the radiation resistance.

In Fig. 5.5, the top surface and the cross-section images of the Mo coating on MoGr is presented. The DCMS coating presents a rough surface, characterized by a well-separated domed end, as shown in Fig. 5.5(a). In the cross-section view of Fig. 5.5(c), the coating manifests an irregular columnar structure through the whole coating thickness. It is possible to observe pores and imperfection at the grain connection. On the contrary, the coating obtained with HIPIMS presents a faceted surface, as in Fig. 5.5(b). The FIB cut in Fig. 5.5(d) shows a columnar dense structure, where grains are well connected.

For thin films, the contribution of the grain boundary scattering strongly affects the electrical resistivity. In this case, the higher resistivity of the DCMS coating, as presented in Sec. 5.2.1, is not related to smaller grain dimension, but to the poor connection of grains [127]. This condition is mathematically modelled as a transmission parameter, representing the transmission of current at the grain boundaries [159].

Similar considerations apply for coated graphite, as shown in Fig. 5.6. The coating realized with HIPIMS present a smoother and more compact texture with respect to DCMS.

The microstructural difference reflects the production process applied for the film deposition. The coating morphology is often related to the production parameters through the use of a structure zone diagram (SZD) [160]. The most simple model represents the coating microstructure as a function of the ratio between the substrate temperature during coating T_S and the melting temperature T_M of the sputtered metal, as shown in Fig. 5.7. With an estimated $T_S \approx 250 - 300\ ^\circ C$ for DCMS coating [127] and the Mo melting temperature $T_M = 2623\ ^\circ C$, the ratio T_S/T_M approaches 0.2. This value ranks in the first zone of the SZD model [160] shown in Fig. 5.7 and it well resemble the coating structure represented in Fig. 5.5(c) and in Fig. 5.6(c). This film growth is related to the reduced atom diffusion in this temperature range, and the lateral grain size is influenced only by the nucleation density [161].

The structure of the HIPIMS coatings in Fig. 5.5(d) and in Fig. 5.6(d) resemble the one in zone 2-3, but their structure cannot be simply related to deposition temperature, and the SZD in Fig. 5.7 is no longer valid for HIPIMS process [161]. The higher quality of the coating is indeed related to the higher fraction of ionized particles in the sputtered flux: the ion flux gives a more efficient momentum transfer to the atom, thus enhancing their diffusion on the substrate surface [162, 163]. A higher density, a lower roughness, and a better adhesion are detected for coating produced with HIPIMS [161, 164–166]. Ions are more easily generated in the

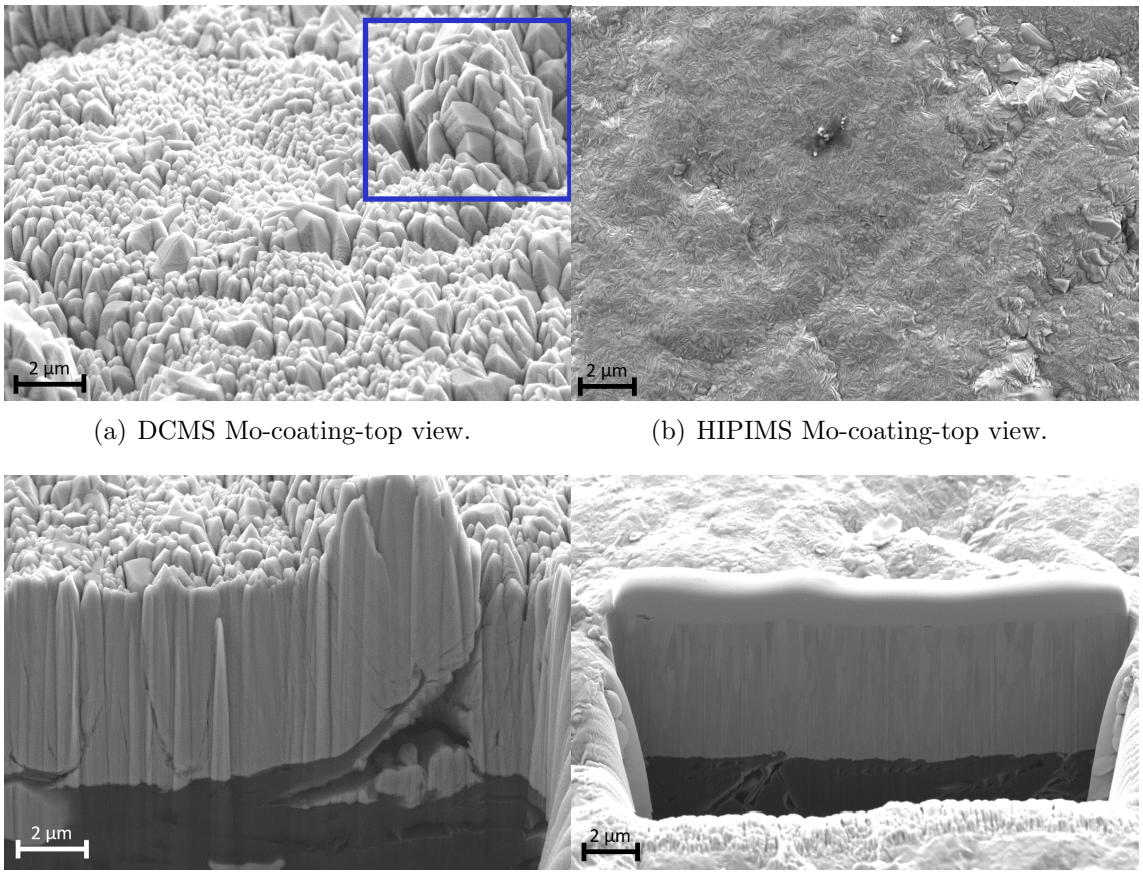

(a) DCMS Mo-coating-top view.

(b) HIPIMS Mo-coating-top view.

(c) DCMS Mo-coating-FIB.

(d) HIPIMS Mo-coating-FIB.

Figure 5.5: Microstructure of Mo-coated produced with DCMS or HIPIMS on MoGr Nb8304Ng.

HIPIMS glow discharge because of the higher plasma density. The achievement of this condition requires higher power, which may potentially damage the target. For this reason, during the HIPIMS film deposition, a pulsed power is applied to the system to guarantee an effective cooling of the target [167].

On the top of these nano-size discontinuities related to grain boundaries, in DCMS coating it is also possible to observe micrometric spherical clusters on the surface, as shown in the blue rectangle of in Fig. 5.5(a). This feature is not present for HIPIMS coating. It is worth underlining that both substrates are characterized by pores and surface inhomogeneities. The filling of these pores is also influenced by the coating process, and it is represented in Fig. 5.8 [167]. The flux of ions characterizing the HIPIMS process is reaching the substrate mainly perpendicularly to its surface. For DCMS process, the pore might be covered before being filled. This behaviour induces a protuberance similar to the spherical features detected on the surface, and it leaves the pores partially empty.

If the substrate inhomogeneities are too big and they cannot be covered by the coating, they appear as surface irregularities on the coated layer, as shown in the red rectangle of in Fig. 5.6(b).

For summarizing, the Mo coating morphology of graphitic substrates is characterized by three level of discontinuities:

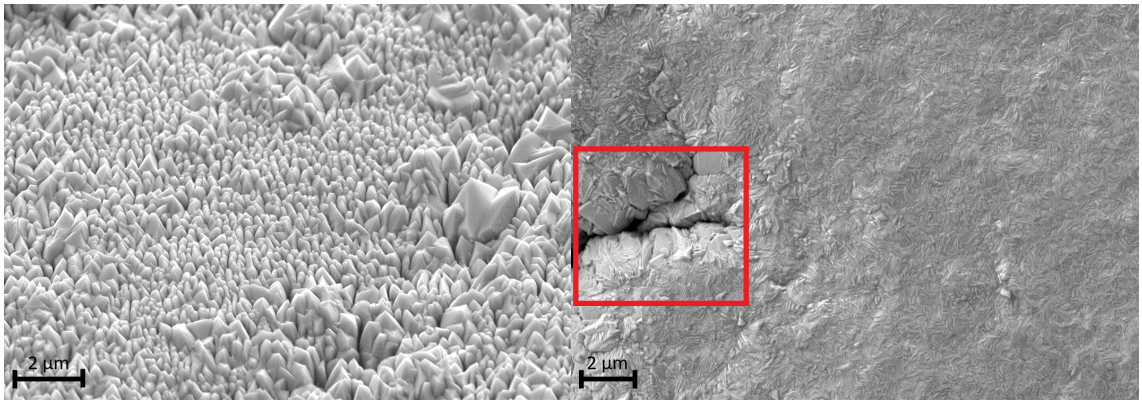

(a) DCMS Mo-coating-top view.

(b) HIPIMS Mo-coating-top view.

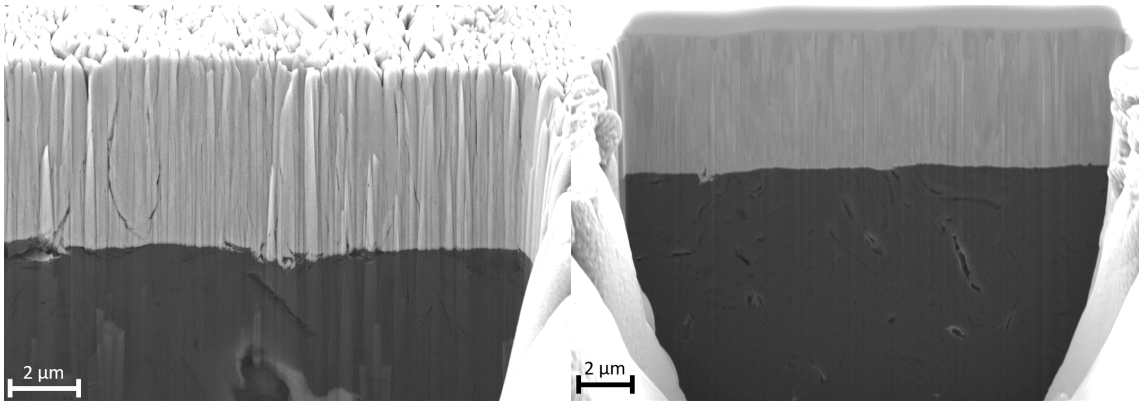

(c) DCMS Mo-coating-FIB.

(d) HIPIMS Mo-coating-FIB.

Figure 5.6: Microstructure of Mo-coated produced with DCMS or HIPIMS on graphite R4550.

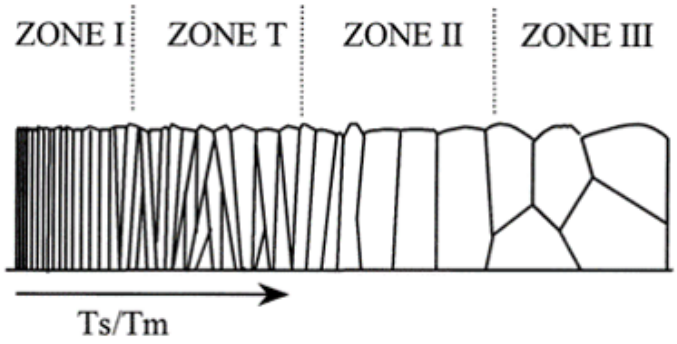

Figure 5.7: SZM model for coating, neglecting the contribution of impurity and influence of gas pressure [160].

- The grain boundaries, whose connection is determine by the coating process
- The spherical protuberance of coating related to small substrate inhomogeneities
- The main substrate profile which is replicated by the coating

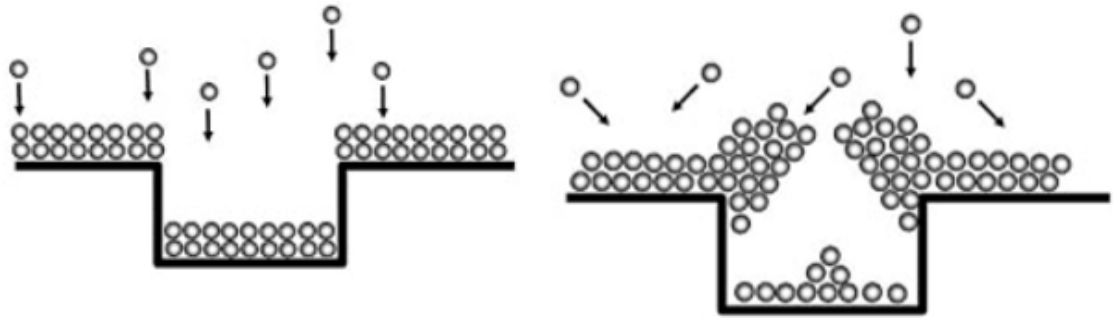

(a) HIPIMS. (b) DCMS.

Figure 5.8: Representation of porosity filling by HIPIMS and DCMS coating processes. [167]

In Fig. 5.9, the FIB cross-sections of MoGr and graphite coated with copper are shown. The coating presents an equiaxed structure, which resembles the zone 3 of the SZD shown in Fig. 5.7. This morphology is related to the presence of ions in the sputtered atoms. A secondary nucleation is indeed promoted by ions, which stop the columnar grain growth in favor of equiaxed structure [163].

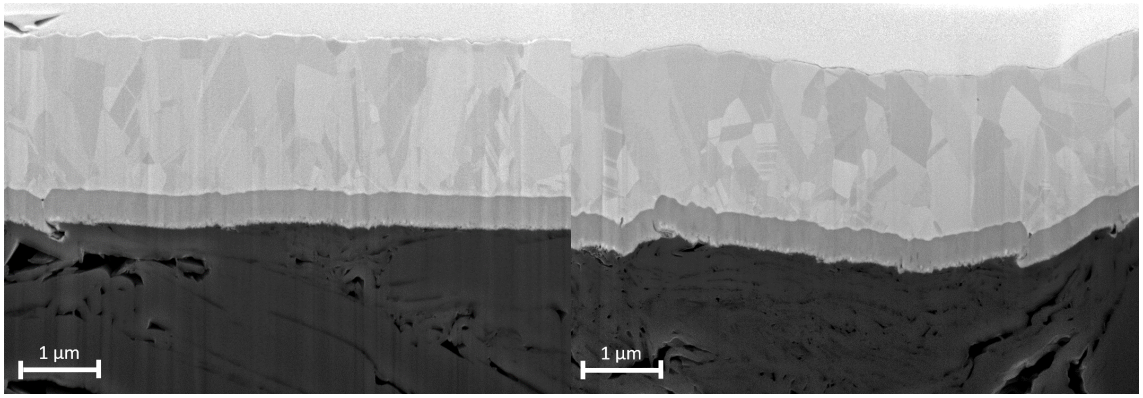

(a) HIPIMS Cu-coating on MoGr Nb8304Ng. (b) HIPIMS Cu-coating on graphite R4550.

Figure 5.9: Microstructure of Cu-coated produced with HIPIMS on MoGr Nb8304Ng and graphite R4550.

Chapter 6

Irradiated material characterization

This chapter is dedicated to the investigation of the radiation-induced changes of the material properties. The evolution of materials under the ion beam is analysed in terms of fluence and the corresponding dpa, to allow a direct comparison with other irradiation tests. In particular, the electrical resistivity of graphitic samples and metallic films is presented. The microscopic investigation of the radiation damage is accomplished with Raman spectroscopy for graphite composites, and with Focused Ion Beam-Scanning Electron Microscope (FIB-SEM) for the coatings.

6.1 Graphite-based materials

6.1.1 Electrical resistivity

The electrical resistivity is a key property of absorber materials, and it is very sensitive to the creation of defects during irradiation. The irradiated layer is characterized by a non-uniform dpa along the ion trajectory, as explained in Sec. 3.4.3. The dpa value close to the surface is, in fact, almost two orders of magnitude lower with respect to the maximum dpa at the end of the ion range. For this reason, it is worth reporting the average and the peak dpa reached in irradiated layer of the samples, as shown in Tab. 6.1.

Fluences $\left[\frac{\text{ions}}{\text{cm}^2}\right]$	Peak dpa bulk	Average dpa bulk
$1 \cdot 10^{12}$	$8 \cdot 10^{-5}$	$5 \cdot 10^{-6}$
$1 \cdot 10^{13}$	$8 \cdot 10^{-4}$	$5 \cdot 10^{-5}$
$2 \cdot 10^{13}$	$1 \cdot 10^{-3}$	$1 \cdot 10^{-4}$
$7 \cdot 10^{13}$	$6 \cdot 10^{-3}$	$3 \cdot 10^{-4}$
$1.4 \cdot 10^{14}$	$1 \cdot 10^{-2}$	$7 \cdot 10^{-4}$
$4 \cdot 10^{14}$	$3 \cdot 10^{-2}$	$2 \cdot 10^{-3}$

Table 6.1: Irradiation fluences and the corresponding peak and average dpa along the ion trajectory.

In Fig. 6.1, the evolution of the electrical resistivity as a function of the average

dpa is shown. All the materials exhibit an increase of resistivity as a function of the dpa. The absolute resistivity of MoGr grades remains below the one of Gr and CFC up to an average dpa of $3 \cdot 10^{-4}$. At higher dpa, the resistivity of MoGr Nb8403Ng approaches the value of graphite. The higher resistivity value is, however, detected for CFC at maximum dpa.

The error bars refer to the standard deviation detected for the measured voltage over 20 measurements. Despite the good repeatability of the measurements, when the irradiated layer becomes resistant, a small variation in the voltage measurement significantly impacts the resistivity calculation.

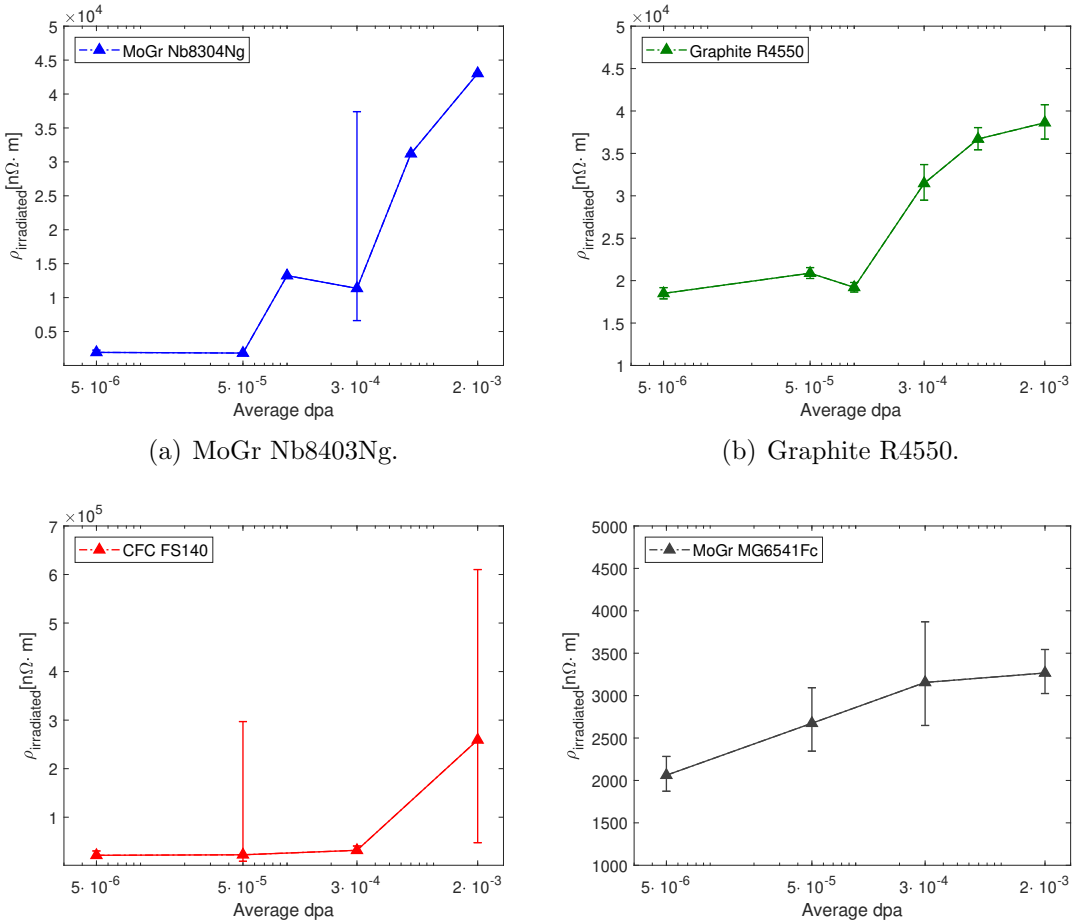

(a) MoGr Nb8403Ng.

(b) Graphite R4550.

(c) CFC FS140.

(d) MoGr MG6541Fc.

Figure 6.1: Electrical resistivity of the four bulk materials investigated as a function of the average dpa in the irradiated layer.

It is interesting to observe the evolution of the irradiated resistivity normalized to its pristine value as a function of dpa, as shown in Fig. 6.2. At the initial stage of irradiation all the materials present a similar trend. MoGr Nb8403Ng and CFC register, however, a steeper increase that starts at $5 \cdot 10^{-5}$ dpa for MoGr Nb8304Ng and at $3 \cdot 10^{-4}$ dpa for CFC FS140.

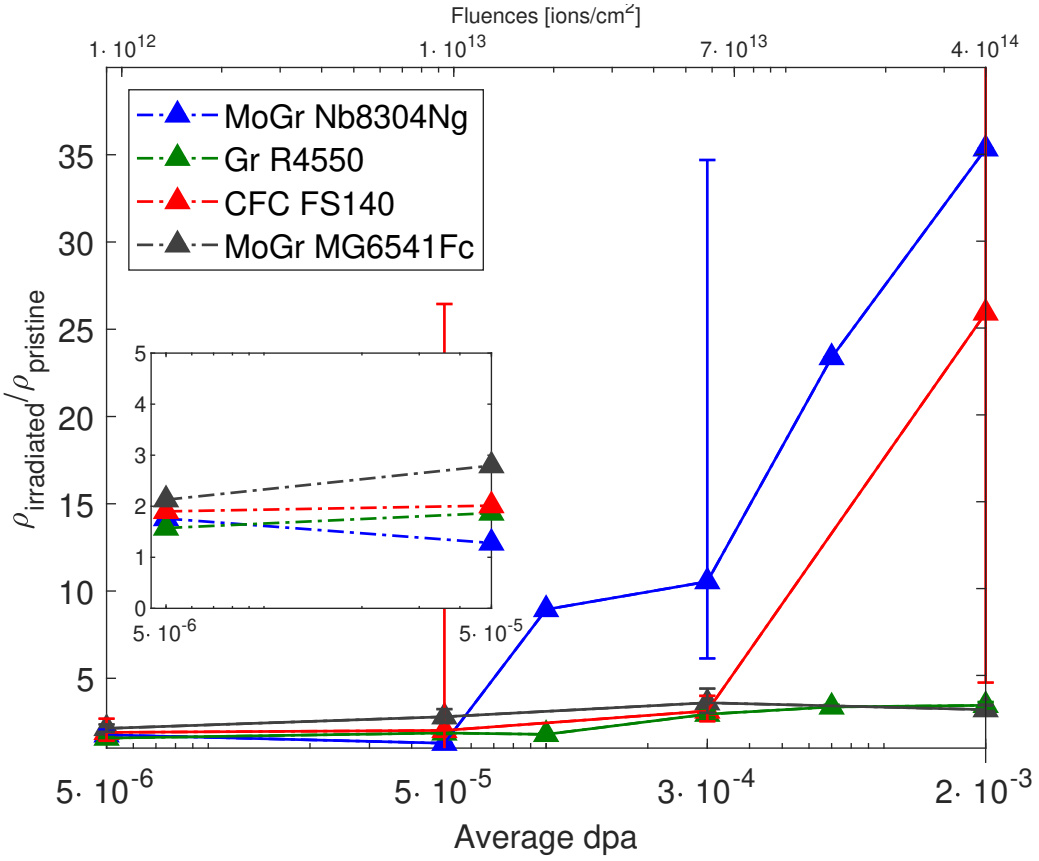

Figure 6.2: Normalized electrical resistivity of the four bulk materials investigated as a function of the average dpa in the irradiated layer.

6.1.2 Raman spectroscopy

Raman spectroscopy is a very useful technique to detect the microstructural order of graphite crystals, as explained in 5.1.2. During irradiation, the projectile particles displace the atoms from their ideal lattice positions, inducing vacancies, interstitials or clusters of defects, thus modifying the response of material during the spectroscopy experiment.

The penetration depth of laser at 514.5 nm in graphite is around $\approx 40 - 100$ nm [168–170]. For this reason, the Raman spectroscopy is a very useful tool to investigate radiation damage induced by ions. The response of the material is, in fact, coming only from the irradiated layer (≈ 50 μm). From the dpa simulations, it is possible to calculate the average dpa rate in the area probed by the laser. Fig. 6.3 represents the dpa rate as a function of the ion penetration depth, and, in particular, it focuses on the area of interest for the Raman spectroscopy. The dpa rate is constant over the first hundreds of nanometers, and it ranges around $1.2 - 1.4 \cdot 10^{-5}$ dpa/h. By knowing this value, it is possible to calculate the corresponding dpa values for the different fluences, which are shown in Tab. 6.2.

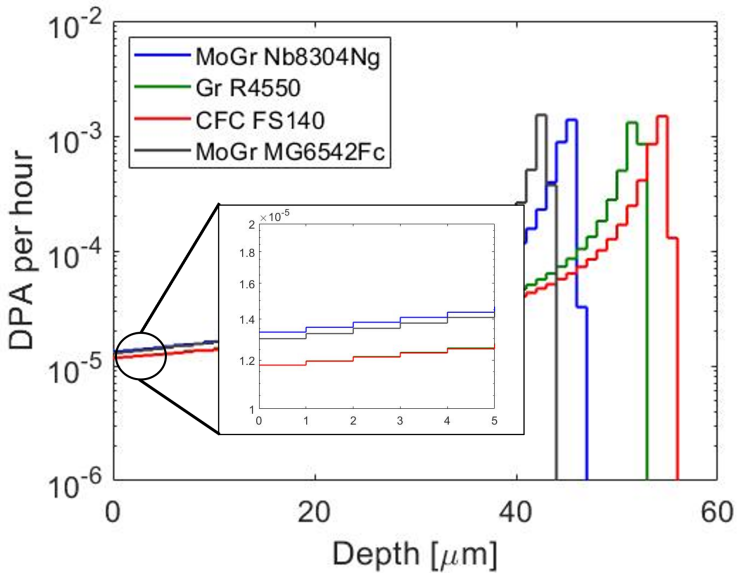

Figure 6.3: Dpa rate as a function of the ion penetration, with a zoom in the area of interest for Raman spectroscopy test.

Fig. 6.4, 6.5, 6.6, and 6.7 show the spectra of the four graphitic samples irradiated at different fluences (i.e. at different dpa). The thicker line represents the average spectrum, calculated as explained in Ap. B, while the thinner lines are all the five spectra measured. For all the materials, an increase of the D peak intensity and a small shift to higher frequency values is observed. For MoGr Nb8304Ng (Fig. 6.4) at higher dpa, the D peak develops a shoulder which is not observed in the pristine samples, but it is detected in ion-irradiated highly oriented pyrolytic graphite (HOPG) [170, 171]. This change is accompanied for all the materials by a small increase of the D' peak. The D and G peak remain, however, well separated, and they do not merge to form an asymmetric band. This transition to a single asymmetric peak is related to amorphization [168, 172], which can be therefore

Fluence $\left[\frac{\text{ions}}{\text{cm}^2}\right]$	dpa
$1 \cdot 10^{12}$	$7 \cdot 10^{-7}$
$1 \cdot 10^{13}$	$7 \cdot 10^{-6}$
$2 \cdot 10^{13}$	$1.5 \cdot 10^{-5}$
$7 \cdot 10^{13}$	$5 \cdot 10^{-5}$
$1.4 \cdot 10^{14}$	$1 \cdot 10^{-4}$
$4 \cdot 10^{14}$	$3 \cdot 10^{-4}$

Table 6.2: Irradiating fluences and corresponding dpa in the area investigated by Raman spectroscopy.

excluded for the analysed samples.

At high fluences, however, some of the samples require the introduction of an additional peak for the first order spectra fitting at $\approx 1500\ cm^{-1}$, as underlined in Ap. B. This additional band is included in graphite starting from a dpa of $5 \cdot 10^{-5}$, and in CFC and MoGr MG6541Fc at the maximum dpa. This feature is not detected for MoGr Nb8403Ng. This band is related to amorphous bonds, and in particular to the presence of interstitial atoms between adjacent basal planes which are involved in sp^3-like bonds [173, 174].

In the second order spectra, the two MoGr grades shown in Fig 6.4 and Fig. 6.7, maintain the characteristic doublet peak of the 2D band, as before irradiation. For graphite and CFC, in Fig. 6.5 and Fig. 6.6, which already before irradiation present a single 2D peak, the shape remain unchanged, but its intensity relatively to the G peak decreases with irradiation.

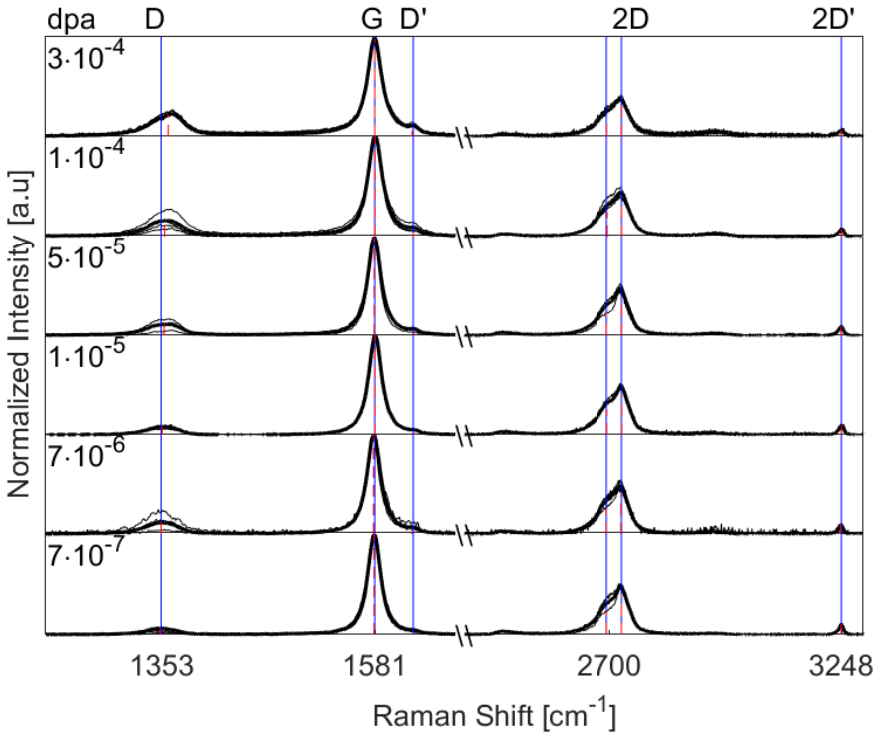

Figure 6.4: Raman spectra evolution for MoGr Nb8304Ng for different levels of dpa.

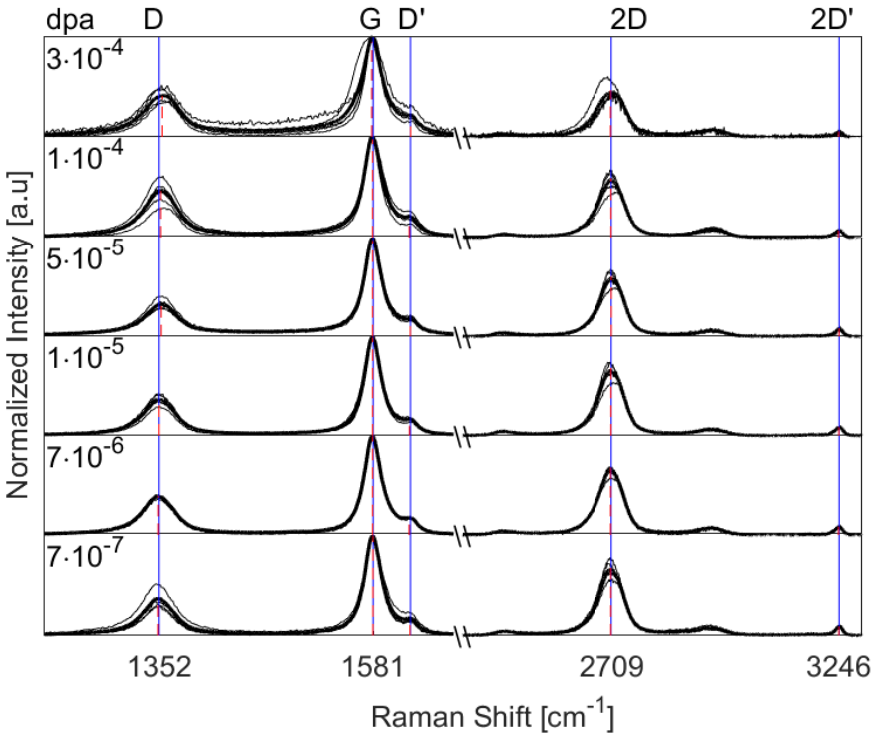

Figure 6.5: Raman spectra evolution for graphite R4550 for different levels of dpa.

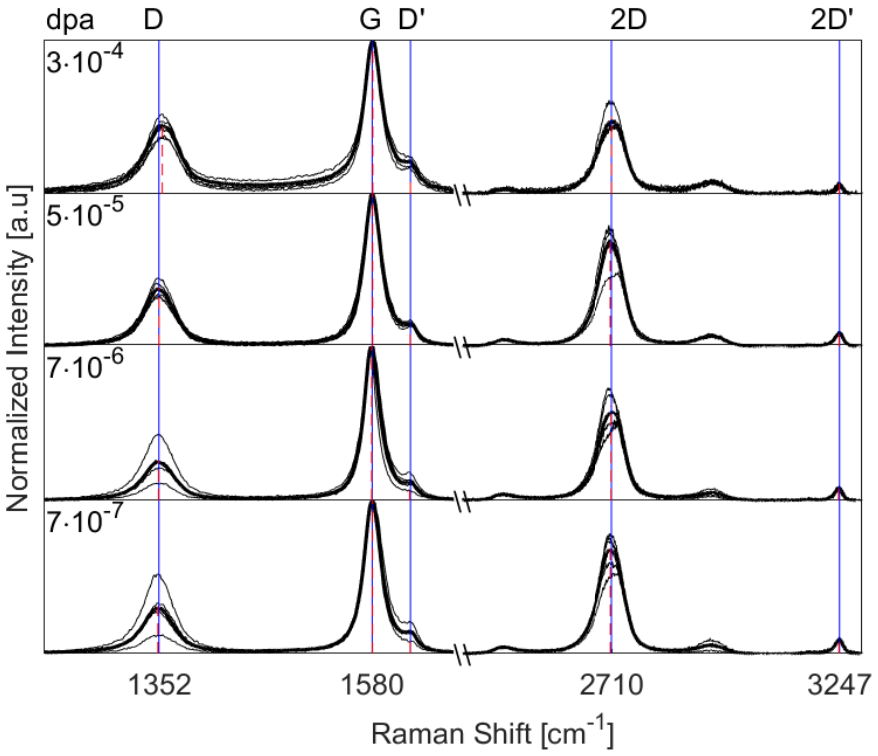

Figure 6.6: Raman spectra evolution for CFC FS140 for different levels of dpa.

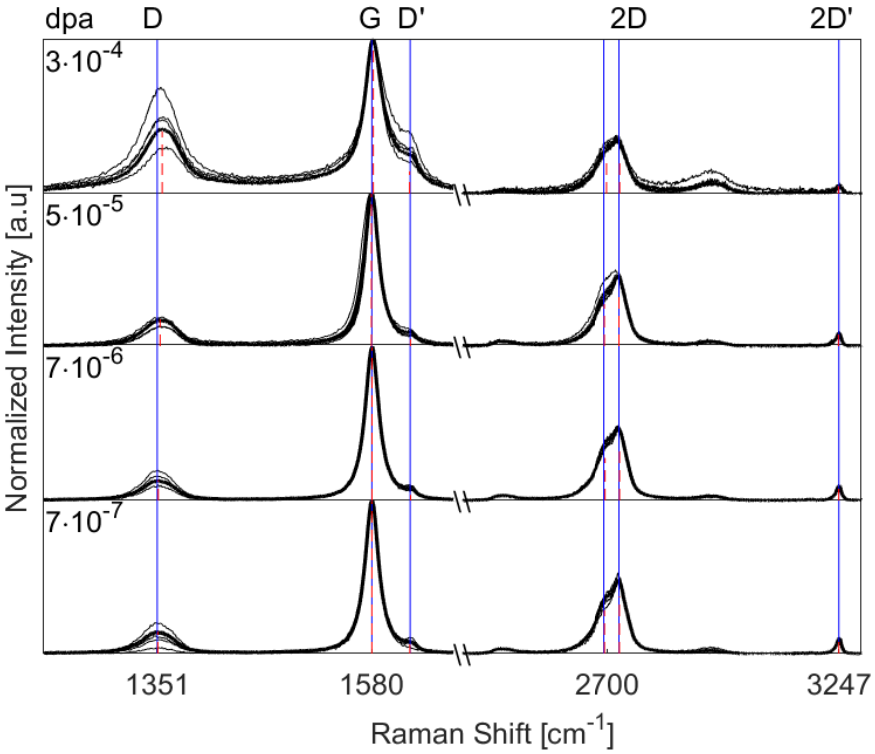

Figure 6.7: Raman spectra evolution for MoGr MG6541Fc for different levels of dpa.

A quantitative analysis is performed after fitting the spectra of the irradiated samples. The error bars represent the expected variation observed on the single samples, as explained in Ap. B.

A first important parameter is the intensity of the D peak compared to the one of the G peak. The increase of the D peak during irradiation does not necessarily correspond to a decrease of the crystallite size, but it can also represent an accumulation of vacancies in the graphite planes [172].

The initial disorder level of the analysed material is very different, as shown in 5.1.2, and it also varies between samples of the same materials. It is therefore worth analysing the relative increase of the D peak intensity normalized to its pristine value to understand the radiation-induced changes.

The plot in Fig. 6.8 shows the peak intensity ratios I_D/I_G of the four different materials normalized for their pristine values as a function of the dpa. Although some oscillations are present, an increase of I_D/I_G is registered for all the materials . The initial decrease observed for MoGr MG6541Fc may be related to the annihilation of some defects present in the pristine structure of the material.

It is interesting to note that the two MoGr grades have the higher variation. These materials are characterized by a better graphitization level before the irradiation. This consideration applies also to CFC, whose initial D peak intensity is lower with respect to graphite, but its increase during irradiation is faster. The correlation between the damage evolution and the pristine graphitization level is indeed extended to all the material studied.

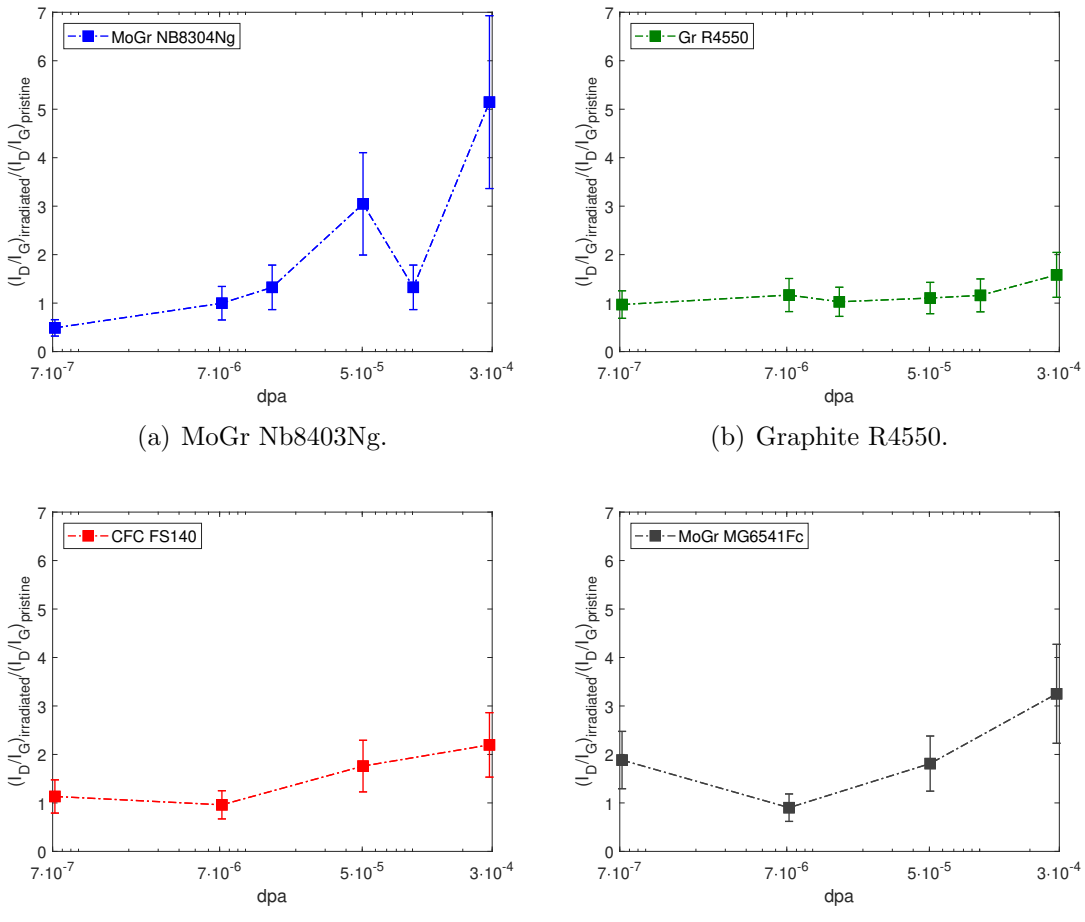

(a) MoGr Nb8403Ng.

(b) Graphite R4550.

(c) CFC FS140.

(d) MoGr MG6541Fc.

Figure 6.8: Evolution of the peak intensity ratios I_D/I_G normalized for their pristine values as a function of the dpa for the different materials investigated.

Fig. 6.9 shows the normalized ratios I_D/I_G as a function of I_D/I_G before irradiation for the highest irradiation fluence. The graphs indicates that at the highest damage level (i.e. the highest dpa) there is an exponential decrease of the induced damage as a function of the initial disorder level in the structure. If the error bars are considered, the difference is less marked for the two MoGr grades, but it is clearly visible when the most (MoGr) and the less (graphite) graphitized materials are compared.

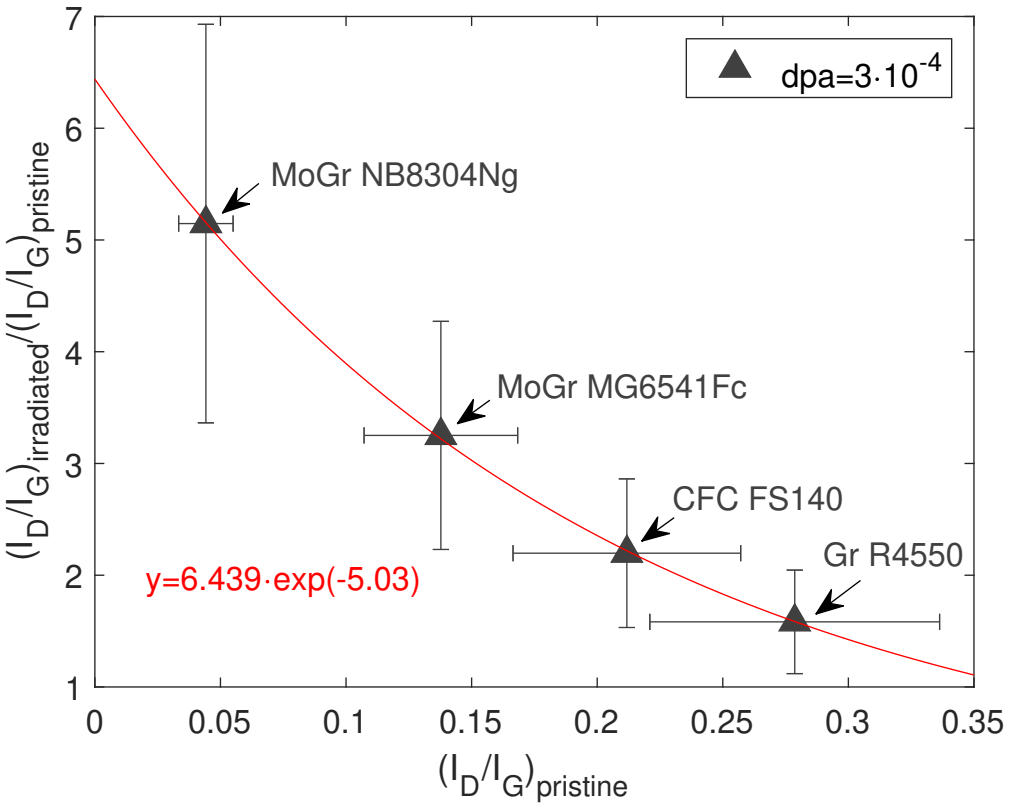

Figure 6.9: Peak intensity ratios I_D/I_G normalized for their pristine value as a function of their initial values at the highest dpa.

In spite of the faster damage accumulation, it is worth mentioning that, in terms of absolute values, the MoGr grades maintain a lower I_D/I_G ratio during irradiation, except for the MoGr MG6541Fc that approaches the level of graphite at the highest dpa, as shown in Fig. 6.10.

Fig. 6.11 shows the FWHM of the G peak normalized to the values before irradiation as a function of the dpa. This is another parameter that relates to the crystalline order along the basal planes, and its increase confirm that the materials become more disordered as the irradiation proceeds. The difference between materials is less pronounced compared to the evolution of the ratio I_D/I_G, and it is not strictly dependent on the initial graphitization level.

The relation between the FWHM of the G peak and the I_D/I_G ratio is represented in Fig. 6.12. Before irradiation, all the samples of different materials are represented along a line, according to the different graphitization level. The irradiated samples seem to belong to the same line that is describing the pristine materials. This

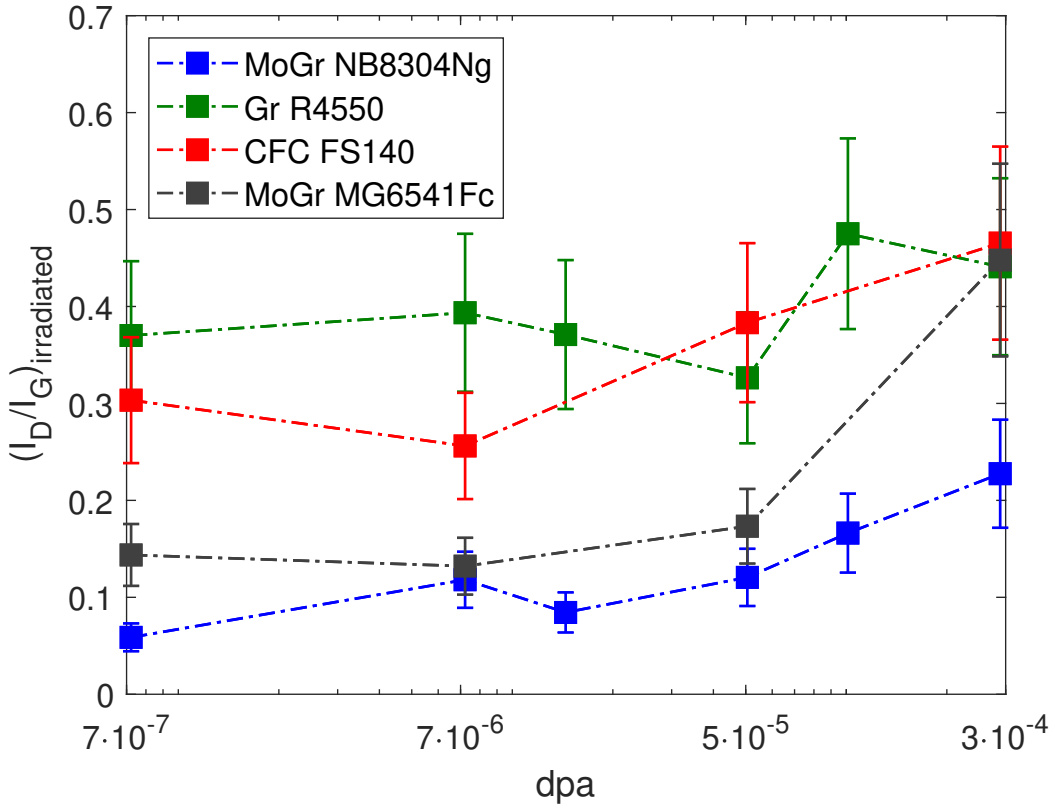

Figure 6.10: Peak intensity ratios I_D/I_G as a function of the dpa.

behaviour is related to an accumulation of vacancies along the basal plane and it confirms that any onset of amorphization is detected. When amorphization occurs, in fact, the in-plane bonds present a different angle and distances, which leads to peak broadening much faster with respect to the increase of the D peak and thus to an upward deviation from the represented line [172].

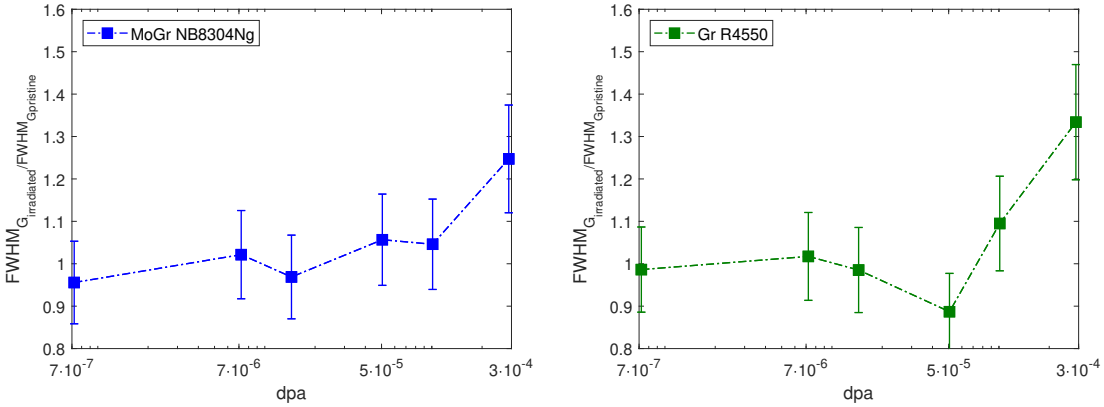

(a) MoGr Nb8403Ng.

(b) Graphite R4550.

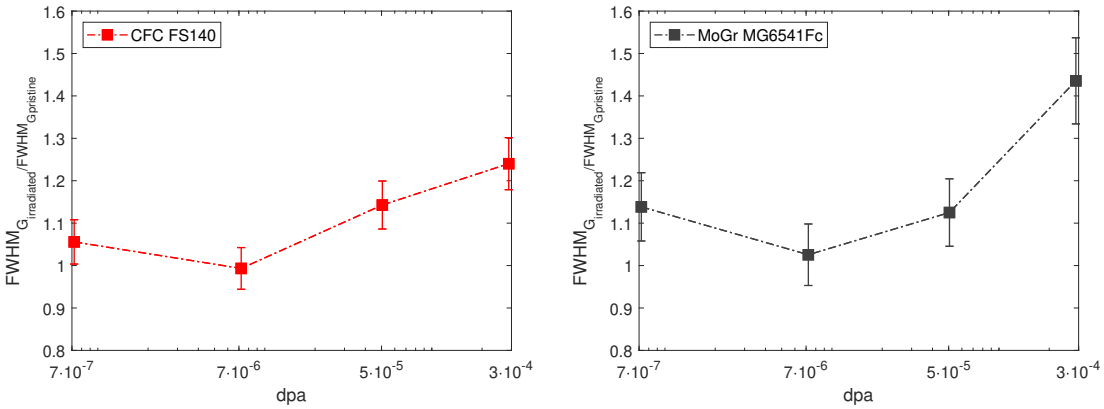

(c) CFC FS140 .

(d) MoGr MG6541Fc .

Figure 6.11: Evolution of the FWHM of the G peak as a function of the dpa level for the four material investigated.

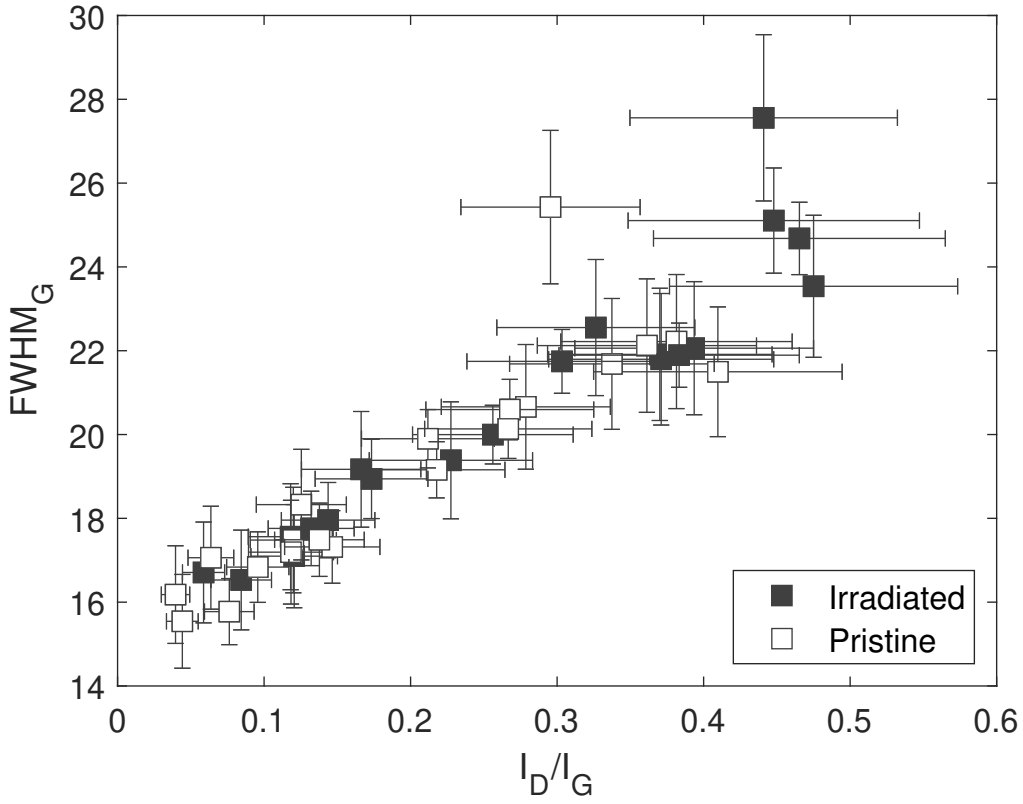

Figure 6.12: FWHM of the G peak as a function of the peak intensity ratios I_D/I_G for all the material before and after irradiation.

The irradiation has an effect, although limited, also on the second order parameters. For the MoGr grades, which present a two-peaks 2D band, the parameter of interest is the relative intensity of these two peaks I_{2DA}/I_{2DB}. In Fig. 6.13(a), the I_{2DA}/I_{2DB} ratio of the MoGr NB8304Ng is represented as a function of the dpa. An initial decrease is detected, as for the I_D/I_G ratio in Fig. 6.8, while at higher dpa it increases. The variation is however negligible if the uncertainty is considered. For the MoGr MG6541Fc represented in Fig. 6.13(b), a monotonic increase of the ratio is observed. This parameter gives an insight on the graphite order perpendicular to the basal planes, and it is related to the out-of-plane lattice parameters c [147]. An increase of this ratio is related to the accumulation of interstitial atoms between the basal planes, and it leads to an increase of the distance between planes.

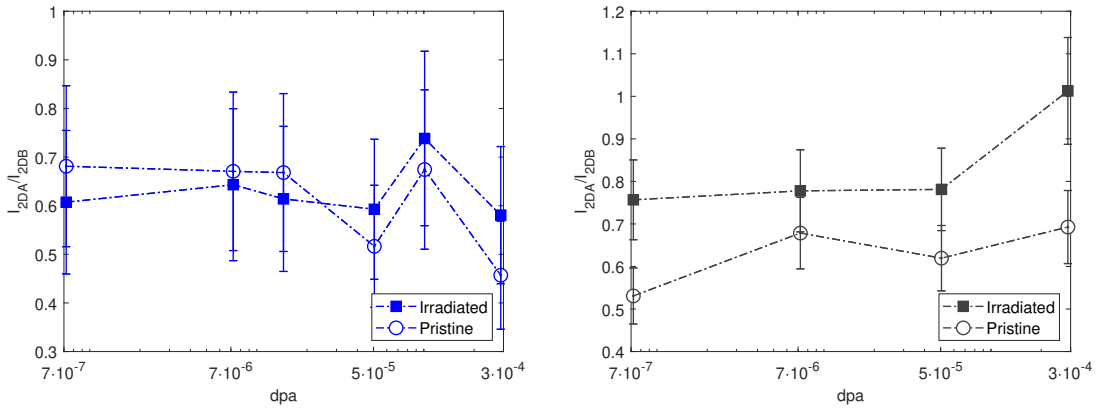

(a) MoGr NB8304Ng . (b) MoGr MG6541Fc.

Figure 6.13: Intensity ratio of the two components of the 2D band as a function of the dpa for the two MoGr grades. The graphs also include, for each of the irradiated samples, the corresponding value measured before irradiation, which are marked as 'pristine'.

For graphite and CFC, which present a single peak 2D band before irradiation, it is useful to analyse the variation of the intensity ratio of the 2D peak intensity with respect to the G peak. The I_{2D}/I_G ratio, normalized for its pristine value, as a function of the dpa is shown in Fig. 6.14. The decrease of this ratio, despite some oscillation at intermediate dpa, indicates a disordering of the structure.

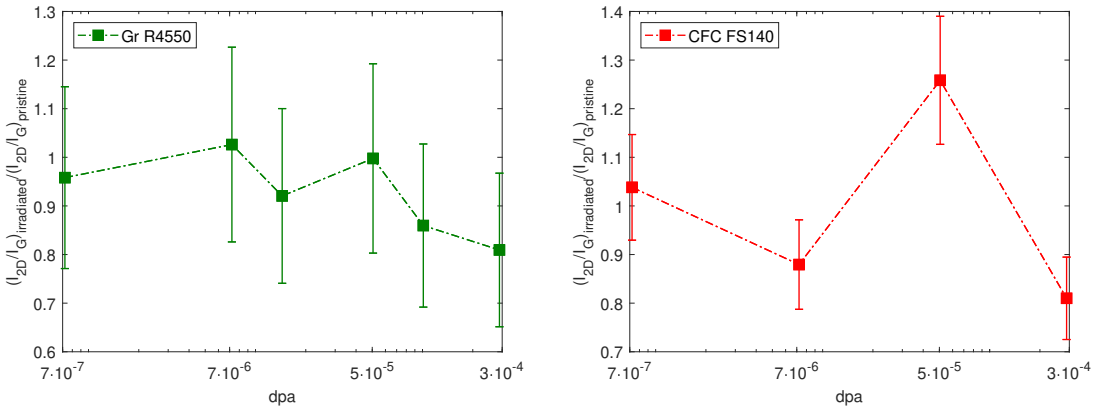

(a) Graphite R4550 .

(b) CFC FS140.

Figure 6.14: Ratio of the intensity of the 2D and G peak as a function of the dpa.

6.1.3 Thermal annealing

In this section, the evolution of Raman spectra of MoGr NB8304Ng and graphite R4550 after thermal treatment at different temperatures is presented. The sensitivity of Raman spectra to radiation-induced defects can be used to detect the temperature-related evolution of the irradiated microstructure. In particular, it is interesting to investigate the minimum temperature needed to activate defect diffusion and annihilation in different graphite matrices. This study is performed on samples irradiated at different dpa to assess if different defects clusters are present, and therefore if the activation temperatures are different.

In Fig. 6.15 and Fig. 6.16, the spectra of MoGr and graphite irradiated at different dpa are reported after annealing at different temperature. For both the materials, it is possible to observe a decrease of the D peak intensity, as reported in literature [175], while an effect of the FWHM of the G peak is not detected.

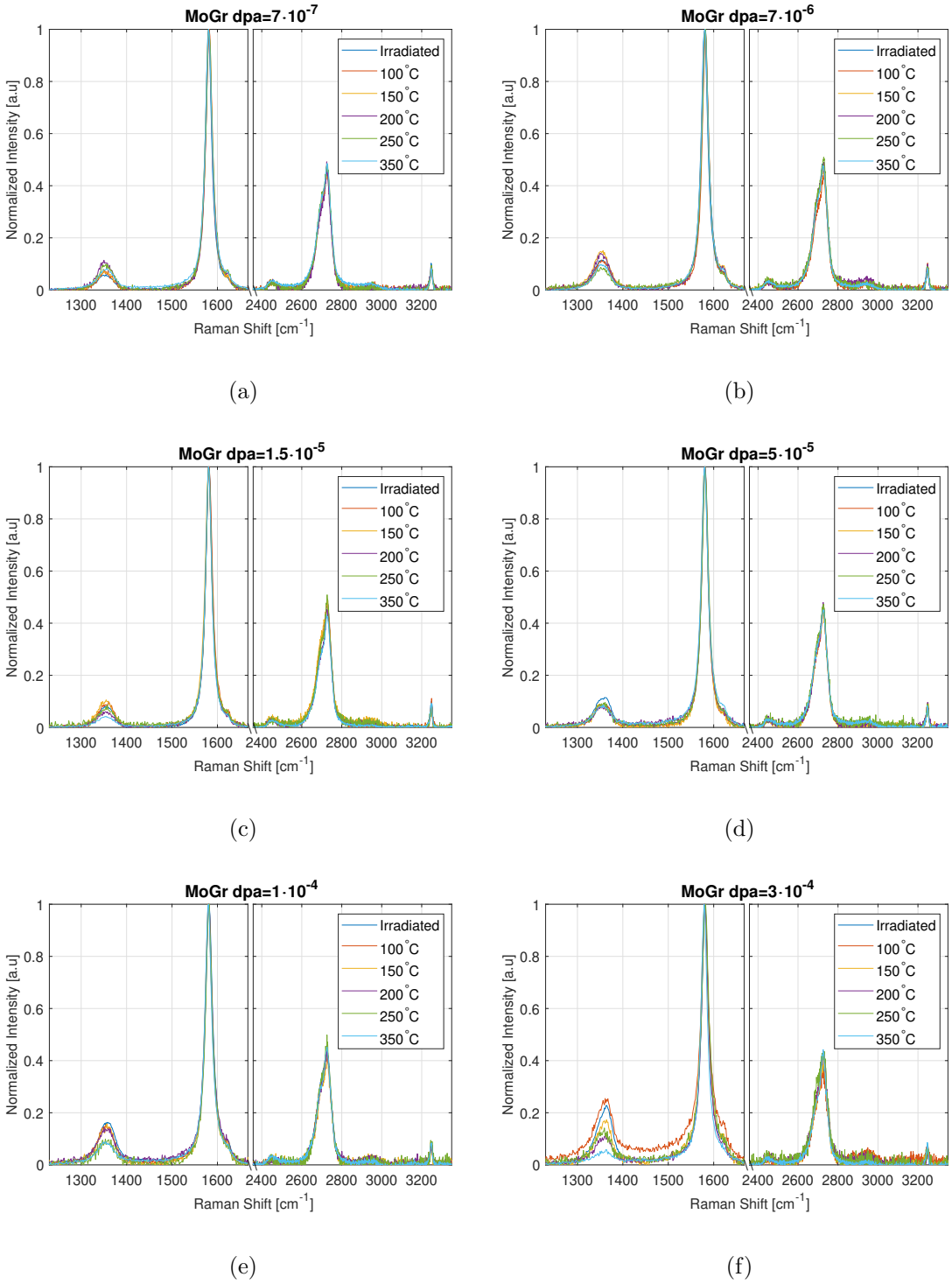

Figure 6.15: Evolution of Raman spectra of MoGr Nb8304Ng irradiated at different dpa as a function of the annealing temperature.

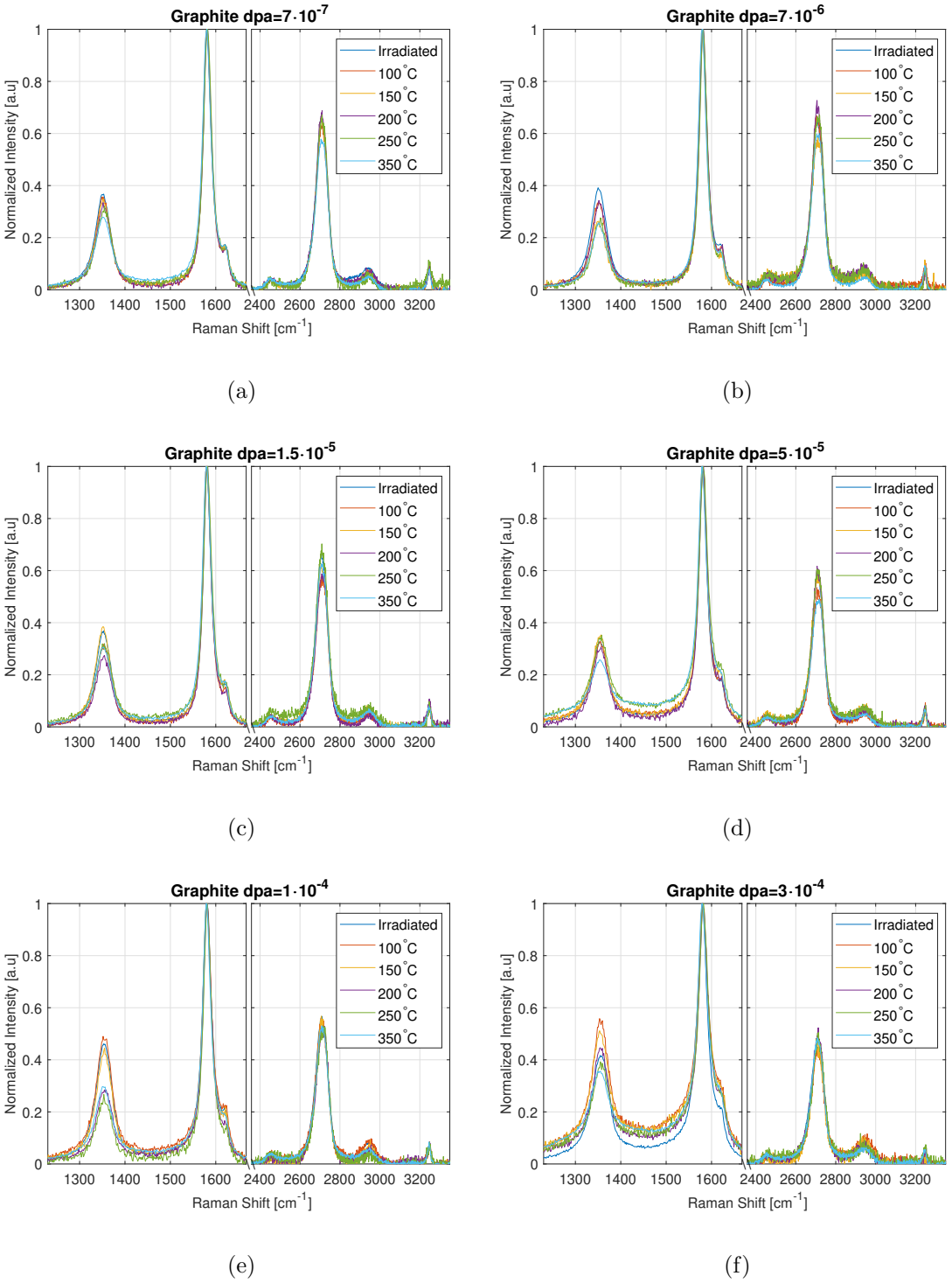

Figure 6.16: Evolution of Raman spectra of graphite R4550 irradiated at different dpa as a function of the annealing temperature.

The analysis performed in Sec. 6.1.2 shows that the ratio I_D/I_G is the most affected by irradiation. This parameter represents the concentration of defects in the materials, and it is worth analysing its changes as a function of the annealing temperature. For a meaningful analysis, it is decided to focus on the samples irradiated at dpa higher than $1 \cdot 10^{-4}$, where the radiation-induced increase of the I_D/I_G ratio is more relevant.

Fig. 6.17 represents the evolution of the I_D/I_G ratio as a function of temperature for two samples of MoGr irradiated at different dpa. It is interesting to notice that for the sample irradiated at the lowest dpa (Fig. 6.17(a)) the unirradiated value of I_D/I_G recovers after a thermal treatment at 200-250 °C, while at higher dpa (Fig. 6.17(b)) a temperature of 350 °C is needed. This behavior might indicate the formation of more stable and complex defects at higher dpa.

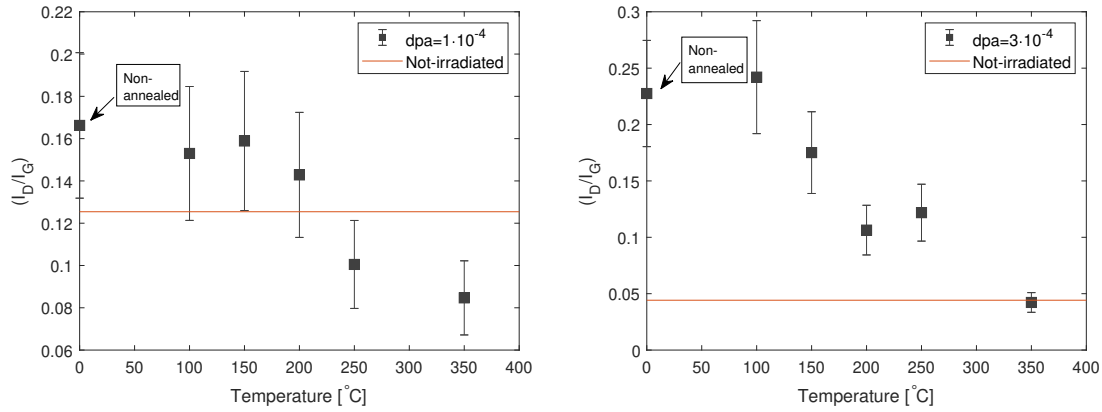

(a) dpa=$1 \cdot 10^{-4}$. (b) dpa=$3 \cdot 10^{-4}$.

Figure 6.17: Evolution of I_D/I_G as a function of temperature for MoGr Nb8304Ng samples irradiated at different dpa levels.

Similar considerations apply to the irradiated graphite samples, as shown in Fig. 6.18. The temperature needed for a complete recovery of the pristine structure are, however, lower: the small increase of I_D/I_G observed at low dpa is, in fact, already recovered at 100 °C, while for the higher dpa a temperature of 250 °C is needed to approach the pristine value.

For both materials, the temperature of complete annealing of the radiation-induced damage reveals that the increase of I_D/I_G is not related to a reduction of the crystallite size, but to an accumulation of defects in the crystals. The recrystallization of graphite is in fact relevant at temperature higher than 1500 °C, which are far above the annealing performed on the irradiated samples. The annealing of graphite below 300 °C is generally assigned to a mutual recombination of unstable in-plane point defects [175].

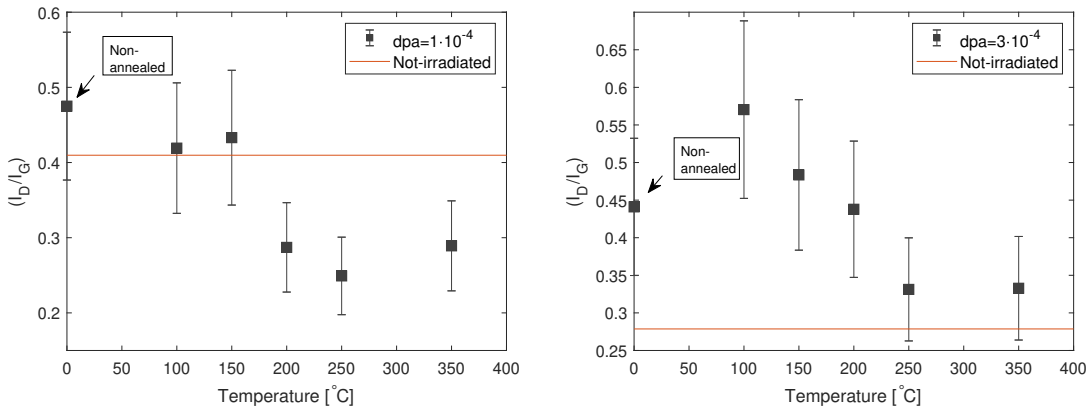

(a) dpa=$1 \cdot 10^{-4}$. (b) dpa=$3 \cdot 10^{-4}$.

Figure 6.18: Evolution of I_D/I_G as a function of temperature for graphite R4550 samples irradiated at different dpa levels.

6.2 Coatings

6.2.1 Electrical resistivity

For coated samples, the electrical resistivity of the metallic film is calculated as explained in 4.1.1. In Fig. 6.1, the evolution of electrical resistivity as a function of the dpa for four coating materials is investigated. Contrary to what is observed for uncoated graphitic materials, the creation of dpa in the thin coating layer is uniform, and it is therefore not necessary to distinguish between average and peak dpa. For all the coating produced with HIPIMS, in Fig. 6.19(a), 6.19(b), 6.19(d) , the increase of resistivity is not proportional to the dpa. The most relevant increase of resistivity is instead detected for the Mo coating produced with DCMS technique.

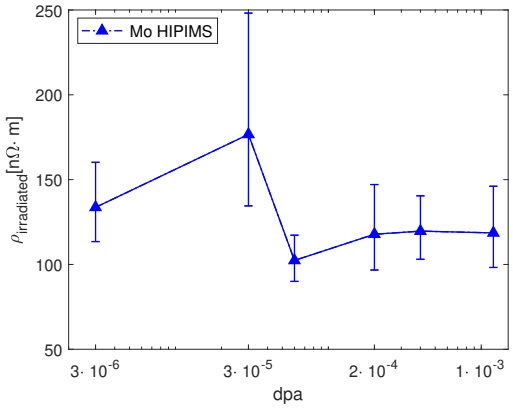

(a) HIPIMS Mo coating on MoGr Nb8403Ng.

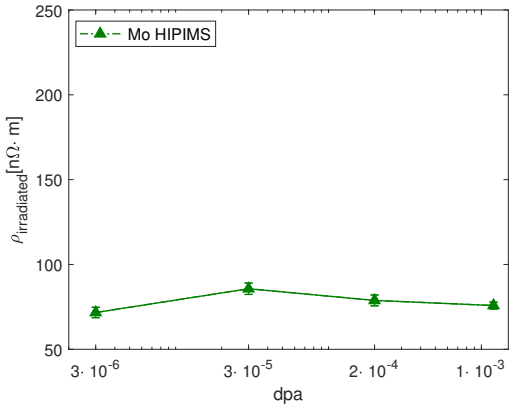

(b) HIPIMS Mo coating on graphite R4550.

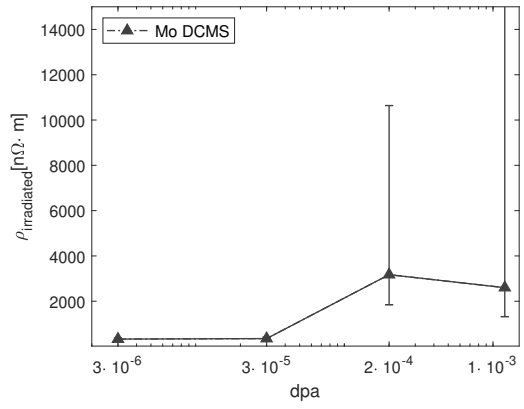

(c) DCMS Mo coating on MoGr MG6541Fc.

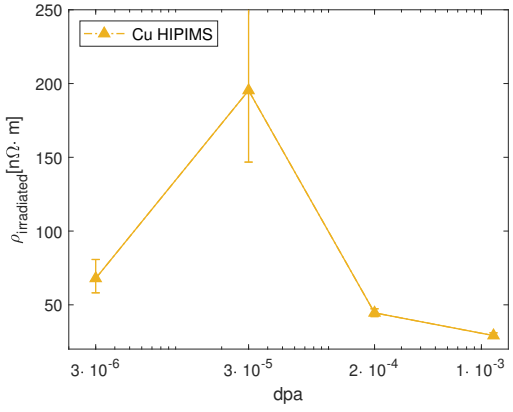

(d) HIPIMS Cu coating on MoGr Nb8403Ng..

Figure 6.19: Electrical resistivity of the coating materials investigated as a function of the dpa.

A similar information comes from the electrical resistivity normalized to its pristine values, as shown in Fig. 6.20 for all the coating. All the coating produced with HIPIMS present an electrical resistivity a factor of 2-4 higher with respect to their pristine values, but there is not a visible trend as a function of the dpa. On the contrary, the coating produced with DCMS shows a relevant increase of the electrical resistivity, which increases as a function of the dpa.

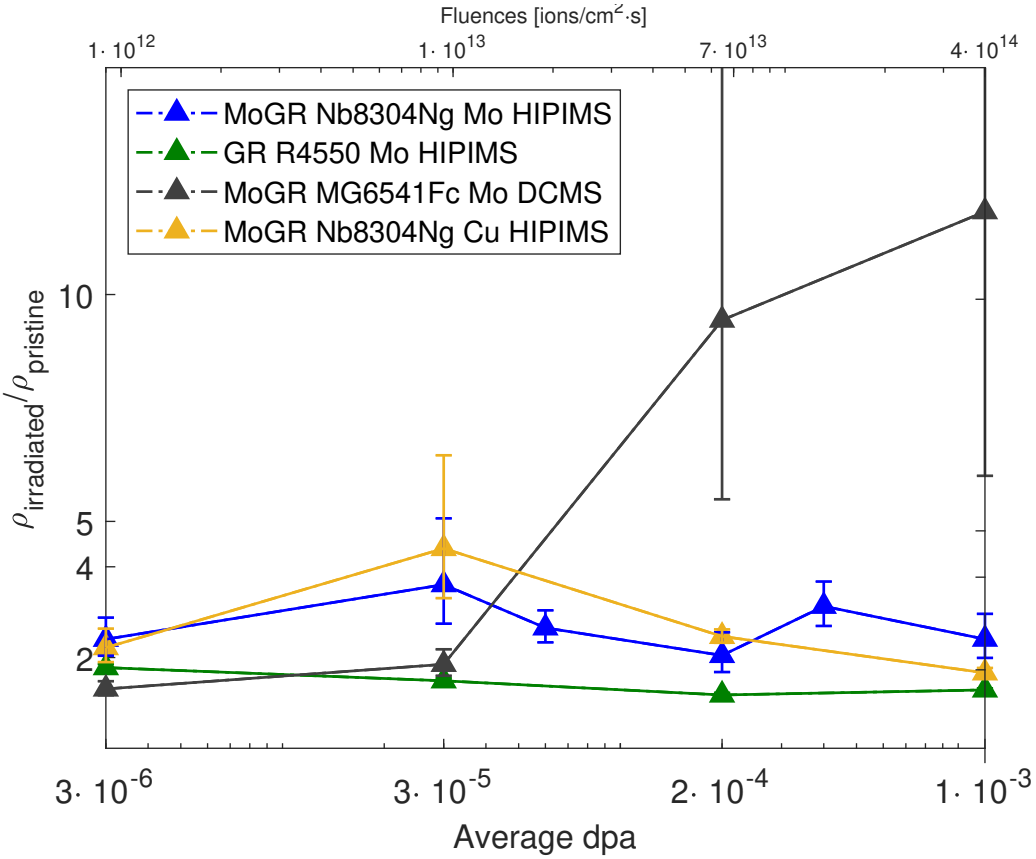

Figure 6.20: Normalized electrical resistivity of the coating materials investigated as a function of dpa.

6.2.2 Microstructure

In this section, the microstructure of the coating after irradiation is presented. In particular, the analysis focuses on the samples irradiated at the maximum fluence, whose dpa level correspond to the expected dpa reached in the coating of secondary collimators at the end of the HL-LHC era.

The HIPIMS Mo coating on MoGr Nb8304Ng is shown in Fig. 6.21: the top panels show the irradiated coating, and, as a comparison, the pristine state is reported in the bottom figures Fig. 6.21(c) and Fig. 6.21(c). The top-view shown in Fig. 6.21(a) reveals a smooth and well-connected structure which resembles the pristine materials. The cross-section of this coating is presented in Fig. 6.21(b). The columnar and dense structure is preserved and there are no macroscopic defects. The adhesion to the substrate is also ideal as before irradiation. The vertical dimensions should be computed by multiplying the marked scale by 1.178 to take into account the tilt correction, as detailed in [176].

The same considerations apply to the HIPIMS Mo coating on graphite shown in Fig. 6.22, and no observable changes are detected after irradiation. Some minor porosities are however present close to the interface with the bulk material, as shown in the cross-section of Fig. 6.22(b). This feature is also visible in non-irradiated materials, in correspondence of surface irregularities of the graphite substrate, and it is thus not strictly ascribed to radiation damage.

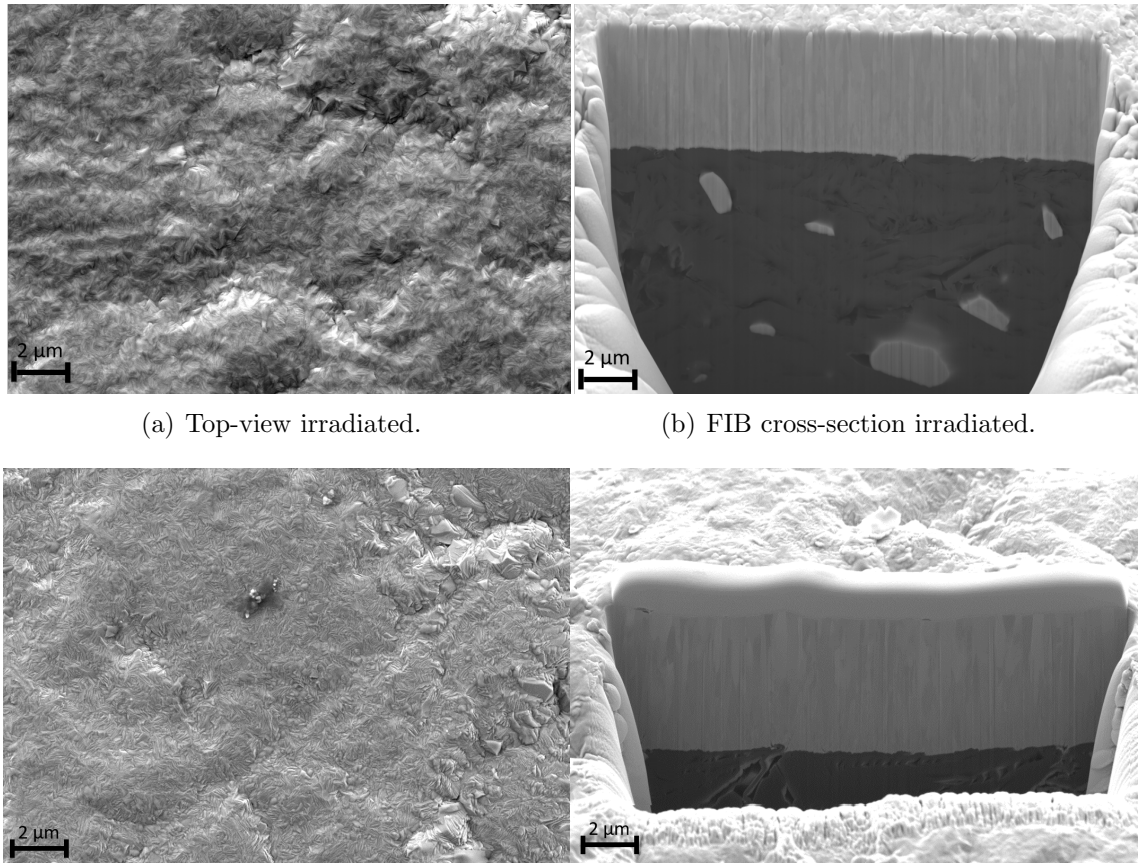

(a) Top-view irradiated.

(b) FIB cross-section irradiated.

(c) Top-view pristine.

(d) FIB cross-section pristine.

Figure 6.21: Microstructure of HIPIMS Mo-coating on MoGr Nb8304Ng irradiated at the maximum dpa (10^{-3}). The bottom panels represent the same coating before irradiation.

In Fig. 6.23 the microstructure of the Mo coating produced with DCMS is presented. This coating is characterized by porosities already before irradiation, which are visible also in the cross-sectional picture of Fig. 6.23. Other defects which can be ascribed to radiation are not present.

Finally, in Fig. 6.24 the Cu coating is shown. Here, as well, there are no changes in the coating morphology.

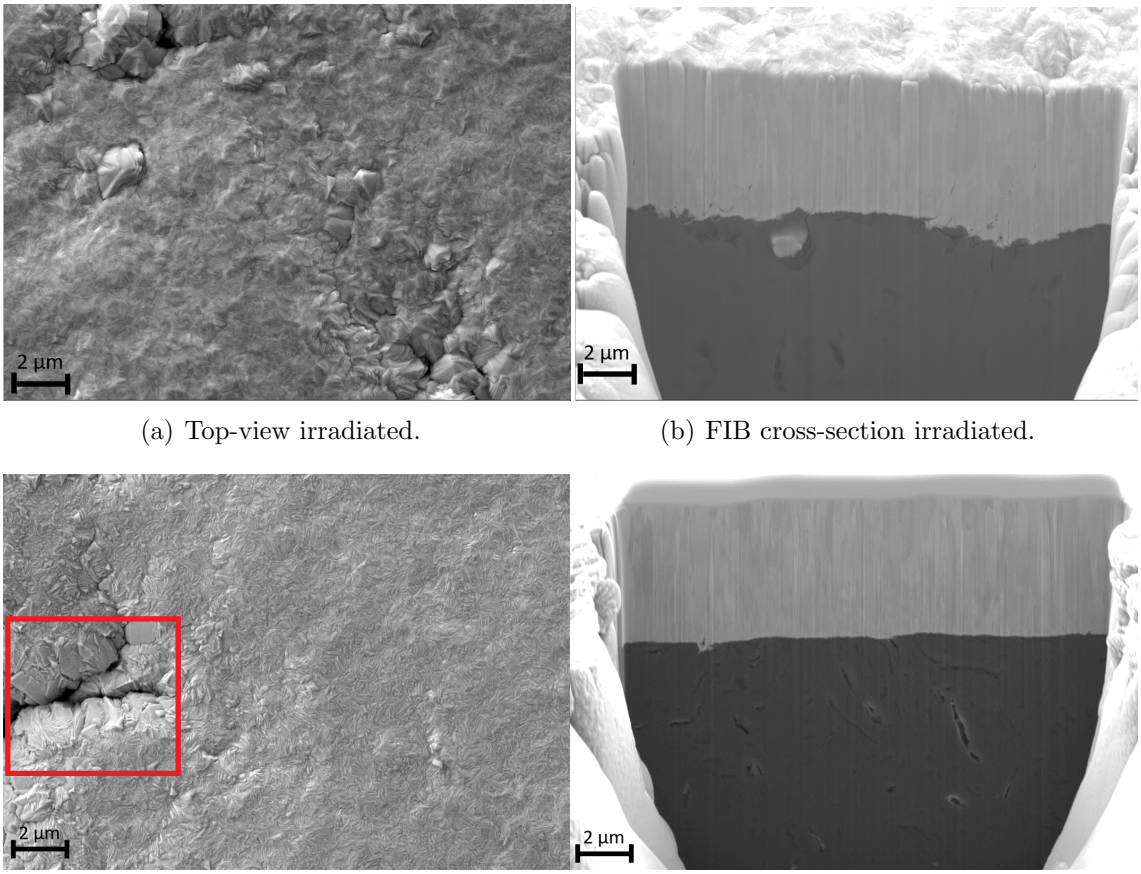

(a) Top-view irradiated.

(b) FIB cross-section irradiated.

(c) Top-view pristine.

(d) FIB cross-section pristine.

Figure 6.22: Microstructure of HIPIMS Mo-coating on Gr R4550 irradiated at the maximum dpa (10^{-3}).

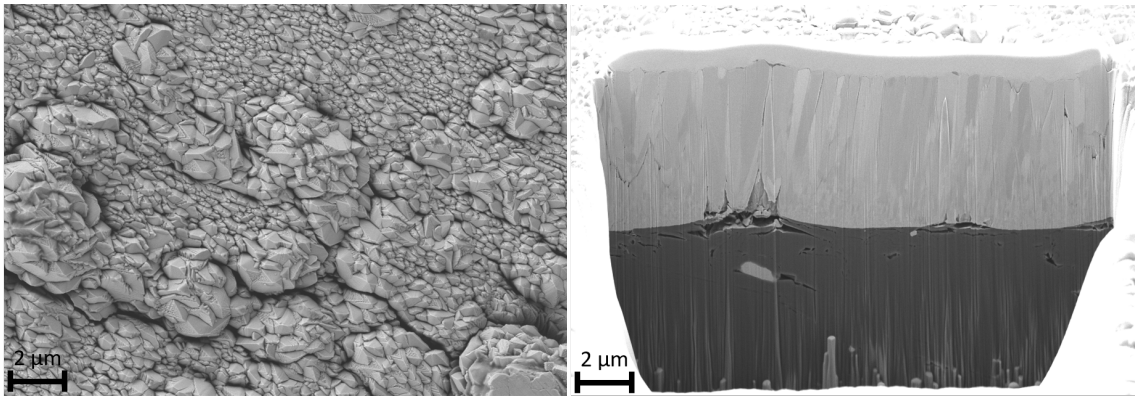

(a) Top-view irradiated.

(b) FIB cross-section irradiated.

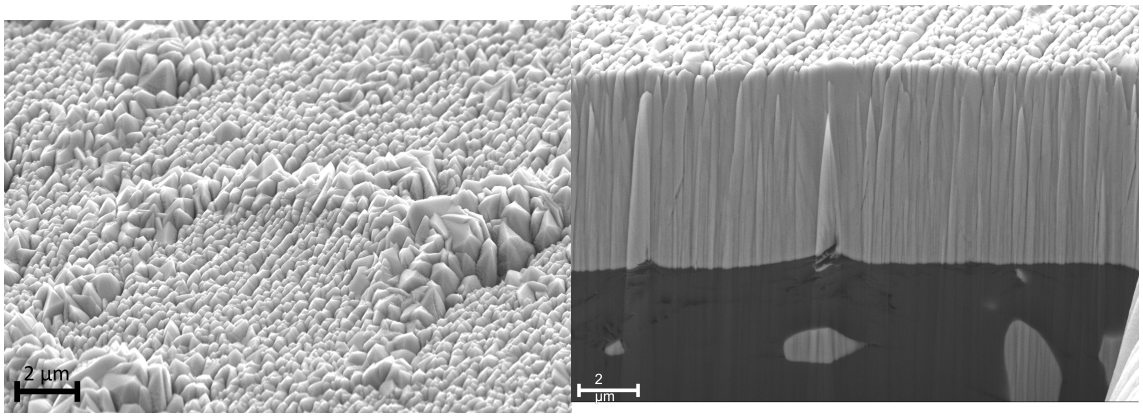

(c) Top-view pristine.

(d) FIB cross-section pristine.

Figure 6.23: Microstructure of DCMS Mo-coating on MoGr MG6541Fc irradiated at the maximum dpa (10^{-3}).

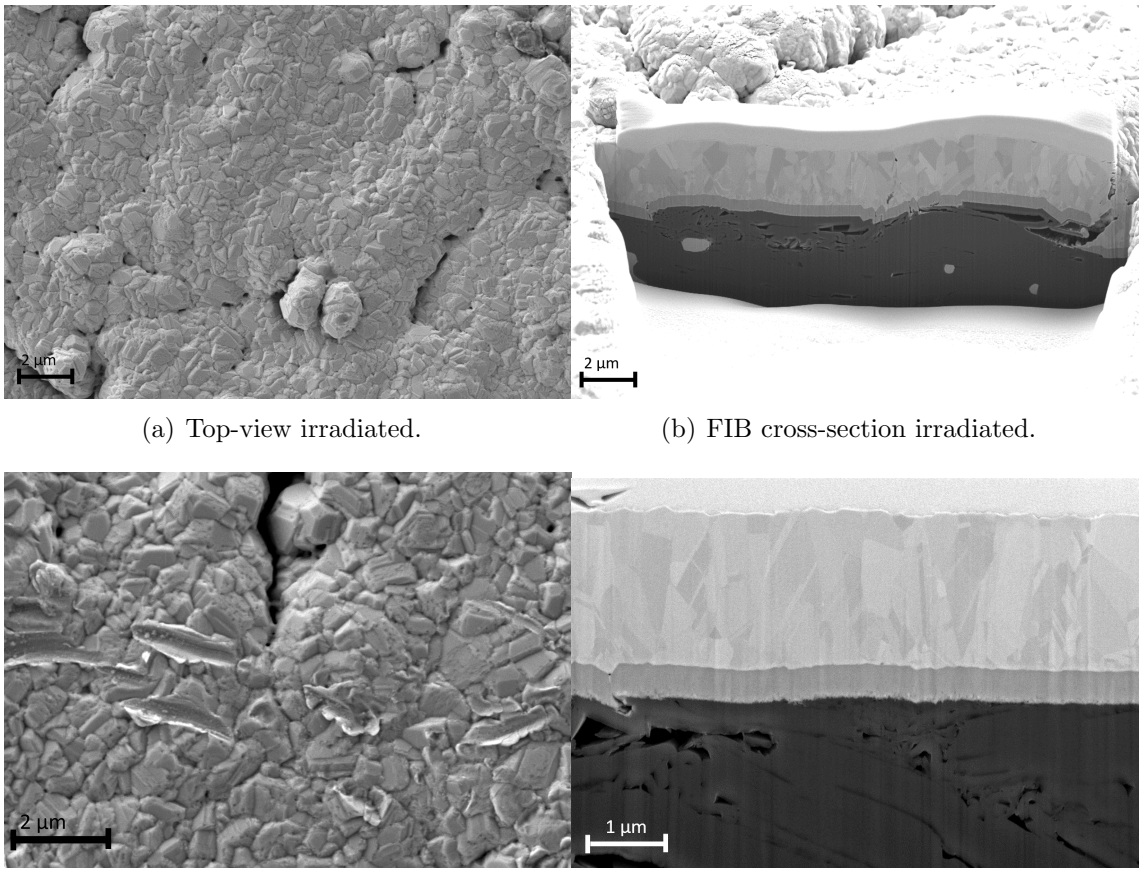

(a) Top-view irradiated.

(b) FIB cross-section irradiated.

(c) Top-view pristine.

(d) FIB cross-section pristine.

Figure 6.24: Microstructure of HIPIMS Cu-coating on MoGr Nb8304Ng irradiated at the maximum dpa (10^{-3}).

Chapter 7

Discussion

In this chapter the results presented in Ch. 6 are discussed to gather a deeper understanding of the radiation damage induced by ions on the materials investigated. First, the attention is placed on the microscopic analysis performed on graphite-based materials with Raman spectroscopy. The typical features of the irradiated spectra are used to assess the defect structure and the dependence on the initial material state. The electrical resistivity changes are then analysed and correlated to the microscopic behavior of both graphite and metallic coating. Finally, the presented data are compared to the expected damage level in HL-LHC collimators, to try to infer the impact on operation.

7.1 Influence of initial microstructure on the radiation damage

One of the main effects of radiation in inorganic materials is the displacement of atoms from their lattice position, and the creation of vacancies and interstitials. In this work, the effect of radiation damage on the microstructure of graphitic materials is studied by analysing the evolution of the Raman spectra under irradiation.

The shape of the first order band permits to exclude the amorphization of the of the materials investigated, according to the analysis presented in [172].

The main changes registered for all the materials investigated are the increase of the I_D/I_G ratio and the $FWHM_G$ as a function of the dpa. These effects are well reported after ion-irradiation of Highly Oriented Pyrolytic Graphite (HOPG) [169, 177] and polycrystalline graphite [178], but also for neutron-irradiated carbon fibres [172] and proton-irradiated graphite [179].

Although the I_D/I_G ratio has been correlated to the crystallite size [146], the increase of the D band intensity under irradiation cannot be related to the crystal size reduction, as underlined by a parallel investigation of the Raman spectra and the diffraction pattern obtained with TEM [172].

The damage induced by ion irradiation in this study should be therefore regarded as the effect of the increased concentration of defects, which affects the phonon correlation length [169]. The annealing of the initial microstructure, which is detected both for MoGr and graphite already at relatively low temperature (350 °C), confirms that the reduction of the crystallite size should be ruled out, as the re-crystallization

temperature of graphite happens at much higher temperature. Complex clusters that break the basal plane are also more difficult to recover, and they are therefore excluded for the present studies [180].

Detectable changes of I_D/I_G ratio are detected at dpa values as low as $5 \cdot 10^{-5}$, similarly to what is observed in [172]. In the following, the differences between materials are analysed to understand if the initial microstructure influences the development of the radiation-induced defects.

The MoGr grades, which exhibit a more ordered structure before irradiation, show the most relevant changes under irradiation, as demonstrated by the increase of the normalized I_D/I_G ratio in 6.1.2. It is important to understand if this corresponds to a higher number of defects that are retained in the graphitic matrix.

In HOPG irradiated with ions, a square-root dependence of the I_D/I_G ratio as a function of the irradiation dose (i.e. the dpa) is experimentally found. According to the so-called *dislocation-accumulation model* [172, 181], this behaviour is related to an increase of vacancy concentration C_V proportional to the irradiation dose, implying that the contribution of the vacancy-interstitial mutual annihilation is neglected. The initial microstructure of HOPG resembles a single graphite crystal, whose Raman spectra is characterized by the absence of the D peak. For the materials presented in this analysis, it is important to consider the contribution of the pristine I_D/I_G ratio, which is therefore subtracted from the irradiated value to highlight only the contribution of the radiation-induced defects. In Fig. 7.1, the incremental increase of I_D/I_G as a function of the dpa is shown and compared to the HOPG data found in literature [172].

From these data, it is possible to conclude that the defects accumulation in the materials is similar. At this level of dpa, the initial microstructure plays a minor role. In particular, the contribution of pre-existing defects, such as grain boundaries, is not relevant in absorbing the radiation-induced defects, as reported in literature [182]. It is, however, interesting to note that the graphite, whose initial microstructure is more disordered, shows the lower value of vacancy concentration, and the almost perfect crystalline structure of HOPG the highest. This difference may become important at higher dpa values, when the defect concentration is higher.

It is worth mentioning that the defects that contribute to the increase of the D peak are characterized by a planar structure with sp^2 bonds [183]. Different configuration may arise from the rearrangement of the basal planes. Interstitial atoms that create bonds between two basal planes are not characterized by sp^2 bonds, and they do not activate the D peak. In this work, graphite, CFC and MoGr MG6541Fc present, however, a new peak at 1500 cm^{-1} when irradiated at higher dpa, which is related to interstitial atoms between adjacent basal planes [173, 174]. These defects are not contributing to the increase of the D peak.

The MoGr Nb8304Ng is the only one that does not develop this additional peak upon irradiation. It is, however, characterized by another peculiar feature. After irradiation at the maximum dpa, in fact, its D band is characterized by an asymmetric shape, which is likely a convolution of two peaks, as shown in Fig. 7.2. This band shape is observed in ion-irradiated HOPG, when irradiated along the edge of the basal planes [184], but also in flexible graphite [185]. In particular, the low-frequency peak is related to the graphite edge, and the high-frequency peak to the radiation-induced peak. The splitting of the D-band is also observed in non-planar

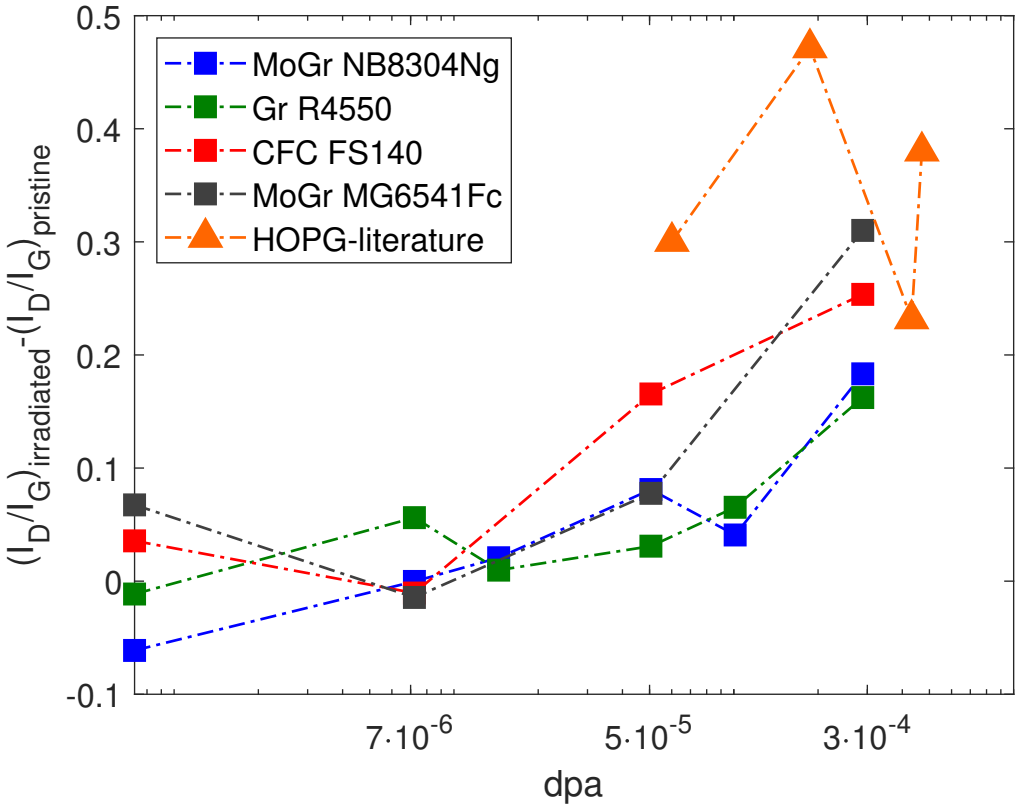

Figure 7.1: Incremental increase of the I_D/I_G ratio as a function of the dpa for the materials presented in this work. As a comparison, the effect of ion irradiation on HOPG is taken from [172].

graphite [186], thus suggesting that the MoGr Nb8304Ng basal planes are partially bending and folding during irradiation. After the thermal annealing, the intensity of the D is significantly reduced, and it is not possible to observe if the band is still split into two peaks. It is, however, worth noticing that the position of the D peak in MoGr irradiated at the maximum dpa is shifted towards higher frequency also after the annealing at 350 °C. This may indicate that the high frequency component of the D band is still present although it is hardly detected due to its low intensity. The defect related to the splitting of the band are therefore more stable and difficult to be removed by annealing.

This analysis leads to the conclusion that in-plane defects accumulation during irradiation is similar for all the materials involved in this work, as demonstrated by the relative increase of the I_D/I_G ratio. The use of such parameter for the analysis of the radiation-induced damage is however not conclusive. The full analysis of the first order Raman spectra underlines, in fact, some differences. In particular, the MoGr Nb8304Ng presents a two-peak shape of the D-band, which has been previously observed in highly-oriented materials after irradiation [185, 187]. Interestingly, this is not detected for the other MoGr grade, whose initial structure has a similar graphitization level. This material develops a new peak at 1500 cm^{-1}, similarly to graphite and CFC, whose initial microstructure is, however, characterized by a higher disorder both along and perpendicularly to the basal planes. The onset of

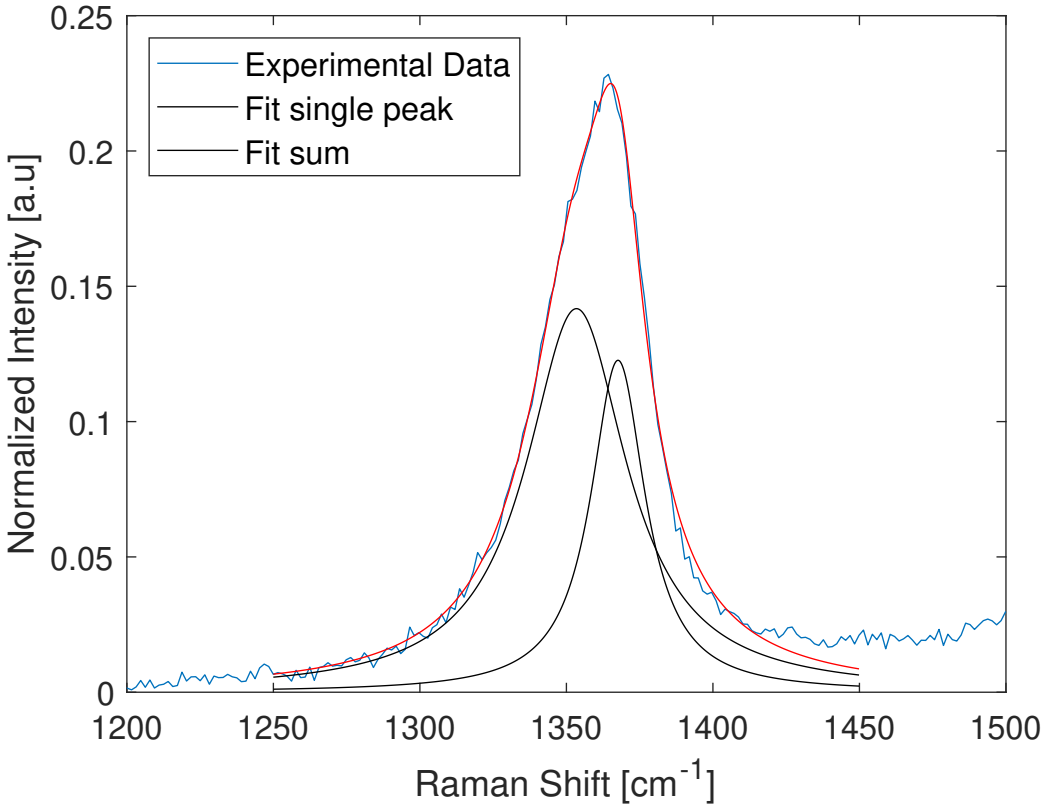

Figure 7.2: Two-peaks fitting of the D band in irradiated MoGr Nb8304Ng.

the peak at 1500 cm^{-1} has also been detected in HOPG, but in correspondence with higher values of the I_D/I_G, typically approaching 1 [188]. This peak has been related to interstitials between the basal planes. This evidence is supported by the increase of the I_{2DA}/I_{2DB} ratio in the second order band of MoGr MG6541Fc, which is related to an increase of the inter-layer spacing. In this sense, the information coming from the first and second order Raman spectra are coherent. This finding is supported by the fact that interstitials demonstrate an affinity with disordered region [182], where the AB stacking is not perfect.

7.2 Correlation between microscopic damage and macroscopic properties

7.2.1 Graphite-based materials

As already mentioned in Ch. 1, the radiation-induced defects decrease the carrier mobility because they are scattering centers, thus increasing the electrical and thermal resistivity. The macroscopic effects of defects are, however, not only dependent on their concentration but critically influenced by their configuration. For this reason, at the same irradiation level (e.g. at the same dpa), the change of properties depends on the pristine state, that, in turn, influences the defects configuration.

The relative increase of electrical resistivity is similar for all the materials anal-

ysed in this work up to an average dpa rate of $5 \cdot 10^{-5}$. At increasing fluences, the MoGr Nb8304Ng starts showing a steeper increase, as shown in Fig. 6.2. If the analysis is limited to this MoGr grade, graphite and CFC, the increase of electrical resistivity is inversely proportional to the initial value. This finding is coherent with neutron irradiation studies on pyrolytic graphite electrical resistivity, where changes are more significant for materials with lower initial resistivities [49]. An exception is represented by the MoGr MG6541Fc, that presents the lowest pristine resistivity, but its increase during irradiation is similar to the one of graphite.

For comparing the microstructural information obtained with Raman spectroscopy to the changes of electrical resistivity, it is important to recall that the dpa rates in the regions probed with the two techniques are different. Close to the irradiated surface, the ions induce a dpa of $1.2 - 1.4 \cdot 10^{-5}$ dpa/h, whereas the average dpa along the ion trajectory, taken into account in the resistivity measurements, is about $9 \cdot 10^{-5}$ dpa/h. For comparing the same dpa, it is therefore necessary to consider the samples for Raman characterization and those for electrical resistivity irradiated at different fluences, as summarized in Tab. 7.1.

Fluence $\left[\frac{\text{ions}}{\text{cm}^2}\right]$	dpa Raman spectra	dpa electrical resistivity
$1 \cdot 10^{12}$	$7 \cdot 10^{-7}$	$5 \cdot 10^{-6}$
$1 \cdot 10^{13}$	$7 \cdot 10^{-6}$	$5 \cdot 10^{-5}$
$2 \cdot 10^{13}$	$1.5 \cdot 10^{-5}$	$1 \cdot 10^{-4}$
$7 \cdot 10^{13}$	$5 \cdot 10^{-5}$	$3 \cdot 10^{-4}$
$1.4 \cdot 10^{14}$	$1 \cdot 10^{-4}$	$7 \cdot 10^{-4}$
$4 \cdot 10^{14}$	$3 \cdot 10^{-4}$	$2 \cdot 10^{-3}$

Table 7.1: Irradiating fluences and corresponding dpa in the area investigated by Raman spectroscopy and electrical resistivity measurements.

The different dpa rate limits the comparison, as few samples are irradiated at the same dpa. It is interesting to note that the steeper increase of electrical resistivity of MoGr Nb8304Ng at dpa higher than $5 \cdot 10^{-5}$ does not correspond to a faster increase in the incremental I_D/I_G ratio, as shown in 7.1. It is, however, important to notice that this MoGr grade develops a two-peak shape of the D band, which is likely related to bending of the basal planes which may be responsible for the faster degradation of electrical conductivity.

In order to assess the reason of the different behaviour of the two MoGr grades under irradiation, it is worth recalling the main differences between the two materials. For what concerns the composition, the MoGr Mg6541Fc is characterized by a slightly lower volume percentage of metallic powders, and by the addition of short C-fibres (250 μm). In past experiment, the presence of C-fibres seemed to reduce the increase of electrical resistivity in MoGr during irradiation [80]. The grade investigated in this work, however, is produced at higher temperature, and the short C-fibres may have dissolved during the sintering. In this case, the presence of C-fiber could not be directly correlated to the enhanced radiation resistance. As mentioned, this grade is also characterized by a higher sintering and annealing temperatures, which are decreased in the MoGr Nb8304Ng to reduce its compaction and thus the outgassing rate. The beneficial effect of higher post-sintering temperature of MoGr

under irradiation is also detected with proton irradiation [125]. Further studies are, however, needed to confirm this hypothesis.

7.2.2 Coatings

The increase of electrical resistivity of the metallic coating produced by HIPIMS does not show a clear dependence on the dpa.

In order to investigate this behaviour, it is worth verifying the sensitivity of the results to the assumptions of the model. The electrical resistivity of the coating is indeed calculated by considering a three-layer resistor in parallel: the irradiated coating, the irradiated bulk and the unirradiated bulk, as explained in 4.1.1. The coating resistivity is considered the only unknown, as the irradiated bulk resistivity is calculated by assuming the same resistivity ratio ρ_X ($\rho_{bulk\_irradiated}/\rho_{bulk\_pristine}$) of the uncoated samples irradiated at the same fluence. The distribution of the dpa is, however, slightly different in the coated samples, and thus the resistivity variation could be affected. The coating resistivity can be expressed as a function of ρ_X, as shown in Eq. 7.1, which is obtained by rearranging Eq. 4.8, 4.9, 4.10, 4.11.

$$\rho_{coating} = \frac{w\, t_{coating}}{d} \frac{R_{parallel}}{1 - \dfrac{R_{parallel}\, w\, (t_{total} - t_{irradiated} + t_{irradiated}/\rho_X)}{\rho_{pristine}\, d}} \tag{7.1}$$

If all the other parameters are fixed (e.g. they are measured), the variation of the normalized coating resistivity as a function of the value assumed for ρ_X is shown in Fig. 7.3. The coating resistivity after irradiation would be lower if higher values of ρ_X are considered. The coating and the bulk are in fact modelled as two parallel resistors. If the bulk is more resistive than expected, the contribution of the coating must be lowered to guarantee the same total resistance. At low ρ_X, which correspond to low fluences, a small variation can significantly affect the calculated coating resistivity. When irradiation proceeds, and the irradiated substrate material resistivity increase, its contribution to the total substrate resistance becomes negligible. At this point, even a big variation of ρ_X with respect to the value assumed in the model, would not affect the coating resistivity values.

In light of these consideration, it is excluded that flat trend of the coating resistivity as a function of the dpa could be related to a wrong assumption of ρ_X.

It is worth mentioning that the aluminium sample holder guarantees a uniform temperature for all the samples installed, as explained in Ap. A. Therefore, it is excluded that the samples irradiated at higher fluences undergo a different annealing with respect the low-fluence ones.

In order to understand the flat behaviour of the HIPIMS coating resistivity, more statistic is therefore needed.

The microscopic investigation presented in Sec. 6.2.2 does not show visible defects in the microstructure for all the irradiated coated samples. The interface with the bulk is not damaged and the adhesion is good. The changes in the resistivity could be therefore related to electron scattering by point-defects.

The DCMS-Mo coating is instead presenting a sharper increase of resistivity, starting from a dpa of $2 \cdot 10^{-4}$.

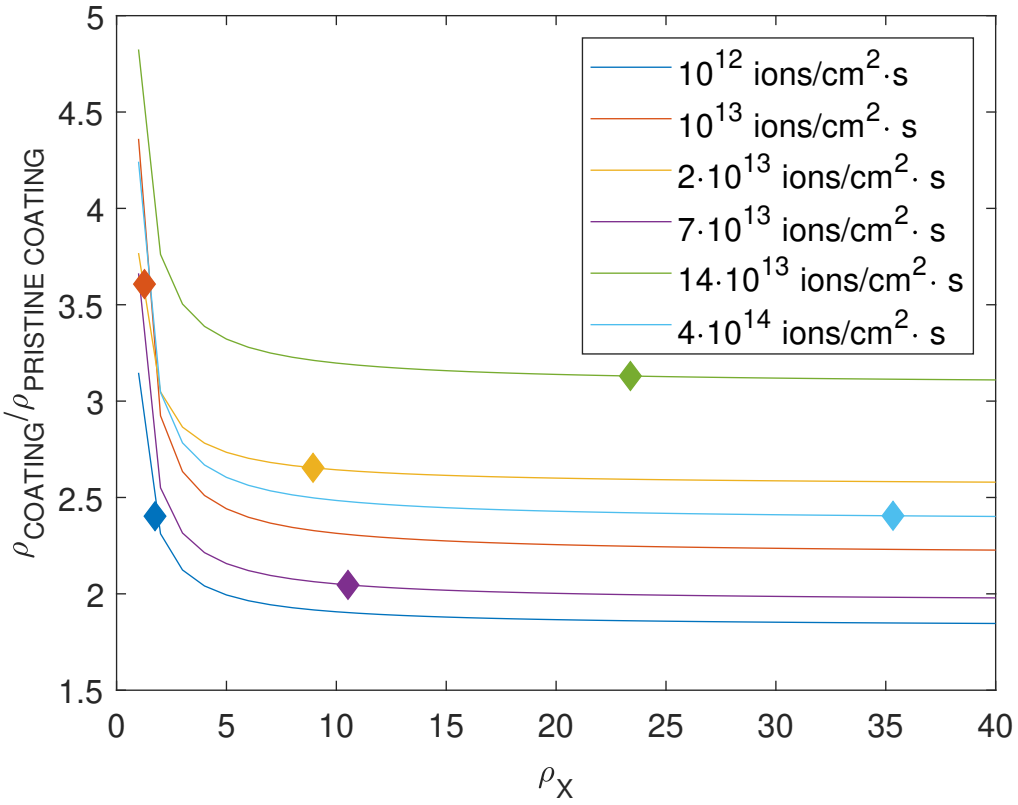

Figure 7.3: Ratio of the irradiated and pristine coating resistivity as a function of the ratio of the irradiated and pristine bulk resistivity ρ_X. The solid points on the curves correspond to the ρ_X and the corresponding $\rho_{coating}$ calculated in Ch. 6.

It is worth reminding that the different electrical properties observed in the coating produced with DCMS and HIPIMS before irradiation are not related to the grain size, but to the poor connection between grains obtained with the DCMS method. The grains observed in the DCMS coating are indeed slightly bigger with respect to the HIPIMS. After irradiation, the grain observed in the FIB cut are still in the range of 0.5-1 μm.

It is well reported in literature that the grain boundaries act as sinks for point defects [189]. The HIPIMS coating presents a higher number of boundaries, which can therefore absorb a higher number of defects. For metals, the mobility of point defects is indeed already relevant at 100 °C, and their diffusion to grain boundaries plays an important role.

7.3 Consequences on HL-LHC collimators

In this section, the irradiation conditions reached during the irradiation are reviewed and compared to the expected radiation environment of the LHC.

As discussed in Chapter 1, the radiation damage depends on a number of parameters.

A first important factor is the irradiation temperature, which affects the defects mobility and hence their annihilation or clustering. The maximum temperature

expected in the ion irradiation experiment presented in this work is around 100 °C. The strong interaction of ions with matter guarantees a complete absorption of their energy in a relatively thin layer. The combination of material properties and the time-scale analysed in this work gives rise to a similar temperature increase in all the material investigated. On the contrary, the high-energy protons circulating in the LHC do not deposit all their energy in the collimator, and their interaction with the absorber blocks is strongly affected by the atomic number and density of the materials.

For the design scenario corresponding to steady-state losses, the maximum expected temperature in the most loaded secondary collimator in case this is equipped with MoGr block is around 130 °C [125]. In the design case corresponding to the 0.2 h beam life-time (fast losses), a maximum temperature of about 250 °C is expected, however collimators are cooled down in few tens of seconds.

The highest dpa reached in the Mo coating during the ion irradiation equals the maximum dpa expected in the most exposed secondary collimators, after 12 years of operation in the HL-LHC configuration. Results presented in this work reveal that the electrical resistivity of the coating is expected to increase by a factor around two at most. In particular, the value found at the maximum dpa level slightly overcomes the technical requirement specified for the coating [190]. The microscopic investigation also reveals that there are no visible changes in the microstructure and the interface with the substrate remains unchanged.

The evaluation of the effects on uncoated graphitic materials is more complicated. The most exposed primary collimator presents, in fact, a strongly localized distribution of the impacting proton, which leads to a non-uniform dpa in the surface layer of the absorber. A peak dpa of about 0.2 is reached in an area extending for less than 500 μm in the direction perpendicular to the beam, represented as the y axis in Fig. 7.4. The dpa value falls rapidly moving away from the beam axis. At a distance of about 750 μm from the peak, the dpa values are in fact ranging from 10^{-3} to 10^{-4}. The results presented in this work do not encompass the peak dpa value reached in the most loaded area of the jaw. At a dpa $3{\cdot}10^{-4}$ the electrical resistivity increases of a factor of about 10. The resulting resistivity of MoGr Nb8304Ng is however still lower with respect to the ones of graphite and CFC. At lower dpa values, the resistivity is almost two times the initial value. These dpa levels are expected in less loaded collimators or in the lateral regions of the most loaded collimator, typically at few tenths of millimeters away from the beam axis.

From a practical point of view, the collimator jaw is equipped with a motor, the so-called 5^{th} axis [101]. Thanks to this mechanism, the collimator jaws can be moved by ± 10 mm along the y direction and the less damaged absorber surface would be exposed to the beam, thus minimizing the perturbation related to the increased resistivity.

Another possible mitigation action, which can be easily implemented in collimators, is the in-situ bake-out. The collimator tank is indeed equipped with heating jackets that can heat the jaws at a temperature of about 250 C°. This bake-out is implemented to reduce the collimator outgassing, and is regularly performed in the LHC tunnel [88, 191]. At this temperature, the annealing results presented in the work reveal a significant decrease in the intensity of the defect-induced D band in Raman spectroscopy, with an expected recovery of thermo-physical properties.

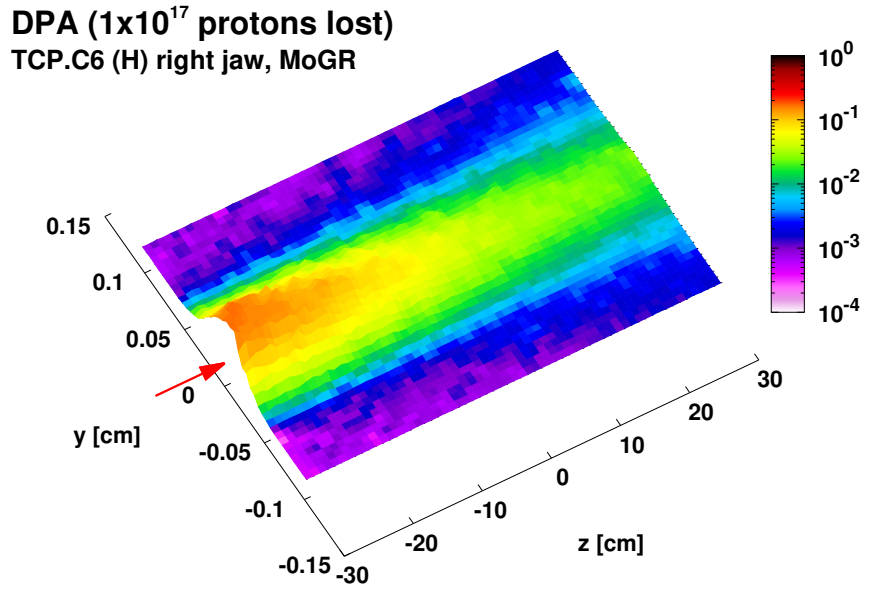

Figure 7.4: Spatial distribution of dpa in a primary collimator. The z direction is parallel to the beam axis.

The temperature increase induced by slow-losses is instead too low to activate a relevant annealing of damage. In the fast-losses scenario, the maximum temperature would be sufficient for thermal annealing, but the rapid cool-down of the collimator jaw is probably minimizing this effect.

Chapter 8

Conclusion

In view of the High-Luminosity upgrade of the Large Hadron Collider, a novel family of metal carbide-graphite composite materials has been developed to equip the jaws of primary and secondary collimators. The main scope of this material upgrade is to decrease the electrical resistivity of the absorber blocks, which largely contribute to the accelerator impedance. R&D programs such as EuCARD, EuCARD2 [1] and ARIES [2] have supported the development of these composites, and in particular of molybdenum carbide - graphite (MoGr).

The present work focuses on a novel grade of MoGr (MoGr Nb8304Ng) that has been optimized for the installation in four primary collimators and eight secondary collimators. This grade is characterized by a lower sintering temperature compared to former MoGr grades; this entails to a slightly more porous structure. The combination of specific production parameters leads to a composite featuring good thermo-electrical and mechanical properties and compatibility with the UHV environment of the LHC [88]. In this work, the electrical resistivity and the microstructure of this material are characterized. The analysis of the Raman spectroscopy reveals an excellent graphitization level of the material, although planar defects are detected in the matrix.

HL-LHC secondary collimator are equipped with MoGr coated with a thin molybdenum film to further reduce the resistivity of the absorber blocks. The work presented in this thesis significantly contributed to the characterization of thin film deposition on graphitic substrates. In particular, it is found that the deposition with DCMS leads to a higher electrical resistivity because of the poor connection between the columnar grains. On the contrary, with HIPIMS process the nominal resistivity of bulk Mo is reached [127].

During HL-LHC operation, the collimation system interacts with and safely disposes of the halo particles, which in turn deposit their energy in the collimator materials. The microscopic evolution of materials under irradiation is commonly referred to as radiation damage, as it negatively affects their macroscopic properties. For this reason, the response of these materials is tested under irradiation.

This work focuses on the ion irradiation of materials for HL-LHC. Thanks to the high displacement cross-section of ions, their high dpa rate allows reaching dpa comparable with the HL-LHC level in few tens of hours. In particular, the materials presented in this thesis are irradiated at the at the M-Branch of the UNILAC accelerator at GSI with ^{48}Ca ions with an energy of 4.8 MeV/u. The dpa rate extracted

from Monte-Carlo simulations is used to determine the duration of the irradiation. In particular, the effect of a maximum dpa of $1{\cdot}10^{-}3$ in the coating is studied. This dpa corresponds to the maximum one expected in the coating of the most loaded secondary collimator after 12 years of HL-LHC operations. The samples are, however, also irradiated at lower dpa values to establish a relation between the dpa and the material degradation.

The thermo-mechanical verification of the experiment design is also presented to assess the maximum temperature reached during the irradiation and the thermal stresses induced in the samples.

The analysis demonstrates that the maximum expected degradation of electrical properties of the Mo coating is compatible with collimator operation. On top of this, the microscopic analysis reveals that there is no visible damage of the coating and the adhesion with the substrate is maintained. The effect of the coating production process on the microstructure and electrical resistivity is analysed. The Mo coating produced with HIPIMS guarantees a better grain connection compared to DCMS, but the microscopic analysis shows that the grain size is actually smaller for the HIPIMS coating. This feature may be responsible for the lower degradation of this coating under irradiation. The higher number of grain boundaries could, in fact, dissipates more efficiently the radiation-induced defects.

The configuration of primary collimators foresees bare MoGr absorber blocks. The new MoGr Nb8304Nb grade has been studied under irradiation for the first time. The material successfully survived the experiment, without any macroscopic damage. The set of data reveals a monotonic increase of electrical resistivity as a function of the dpa. A steeper increase is however detected at dpa higher than $5 \cdot 10^{-5}$. The comparison between the electrical properties and the microscopic structure seems to indicate that the MoGr degradation at higher dpa could be related to a partial bending of the basal planes, which is not detected for the other materials investigated. In future tests, this aspect shall be monitored to understand if it is specific to ion damage. The other MoGr grade does not present this feature, and the increase of the electrical resistivity is much more limited. Two hypotheses are addressed to explain this difference, but further studies are needed.

The observed degradation of electrical properties is analysed and compared to the expected radiation level of HL-LHC. This material would maintain a lower electrical resistivity with respect to the presently installed CFC up to a dpa level of $3 \cdot 10^{-4}$, which correspond to the dpa level reached in the most loaded secondary collimators. If needed, the increase of resistivity can also be compensated by moving the collimator jaw along the y direction, and thus exposing a less damaged surface to the beam.

On top of this, the annealing test presented in this work strongly suggests the use of the in-situ bake out of collimator to anneal the radiation-induced damage.

The presented data support the use of MoGr and Mo coating for the HL-LHC collimators. The complete modeling of the irradiation-induced damage in these materials would require, however, additional data to take into account the different irradiation conditions.

The methods and the theories developed in this work will be applied in future irradiation campaigns to extend the statistic and the understanding of the phenomena. In particular, a new Ca-ion irradiation campaign has been carried out at GSI in

March, 2021 on MoGr and graphite coated with Mo. This campaign focus on studying the effects of the flux, and thus the dpa rate, on the microscopic and electrical changes of materials. For this purpose, a new set-up for the electrical resistivity has been realized to reduce the uncertainty of the measurement.

The effects of transmutation gas cannot be accessed with the presented ion irradiation. This aspect is however accessible with the proton irradiation campaign held in BNL in 2018 on Mo-coated MoGr, in the framework of the RaDIATE [126] collaboration. The post-irradiation examination of these samples is going on at the time of the writing: the comparison with the presented results would help to establish a correlation between ion and proton irradiation.

Appendix A

Discussion of boundary conditions applied to thermal simulations of ion irradiation

The estimation of the maximum temperature reached by the samples during irradiation is important to evaluate the thermal-induced stresses, but also to understand if thermal annealing of radiation-induced defects is taking place.

The temperature is influenced by different parameters, and, in particular, some deviation from the expected value could be related to the conductances calculation. Their values is, in fact, determines by assuming a tightening torque, and by calculating the corresponding pre-load induced on the screws. This calculation has some uncertainties related to the assumed friction coefficient. On the top of this, for anisotropic materials the through-plane thermo-mechanical properties are used for the calculation of the conductance, according to Eq. 3.2 [129]. The contribution of the in-plane properties is therefore neglected in the model.

For this reason, the temperature change during irradiation is simulated with different values of conductances at the interfaces between the sample, the holder, and the clamp. A series of models are runs with conductances values ranging from the 1% up to 100% of the real ones, and the corresponding temperature evolution is shown in Fig. A.1. The maximum temperature, assuming conductance values down to the 1% of the calculated values, is 120°C.

The thermal conductivity of the irradiated samples degrades because of radiation damage, and this can influence the temperature evolution. For this reason, a simulation is run with thermal conductivities down to the 1% of the initial values, for the lowest conductance case. The maximum temperature remains below 130°C. In graphitic materials, the annealing of radiation-induced defects is negligible below 200 °C [148, 192–194]. The maximum temperature reached in the most conservative simulation is however below this values, and the effect of thermal annealing can thus be neglected in the present study.

The temperature along the sample holder is uniform, as shown in Fig. A.2, therefore the samples irradiated at different fluence seen the same maximum temperature.

For future irradiation campaigns, the effect of ion flux on the temperature evolution is investigated. In particular, a model with a flux one order of magnitude lower ($\phi = 8 \cdot 10^8 \ \frac{\text{ions}}{\text{cm}^2 \cdot \text{s}}$) is studied. In Fig. A.3, it is shown that for this flux the

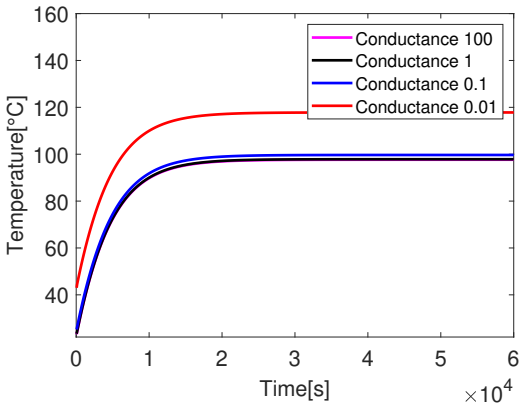

Figure A.1: Evolution of temperature on the irradiated sample as a function of time for different values of conductances at the interface with the sample holder.

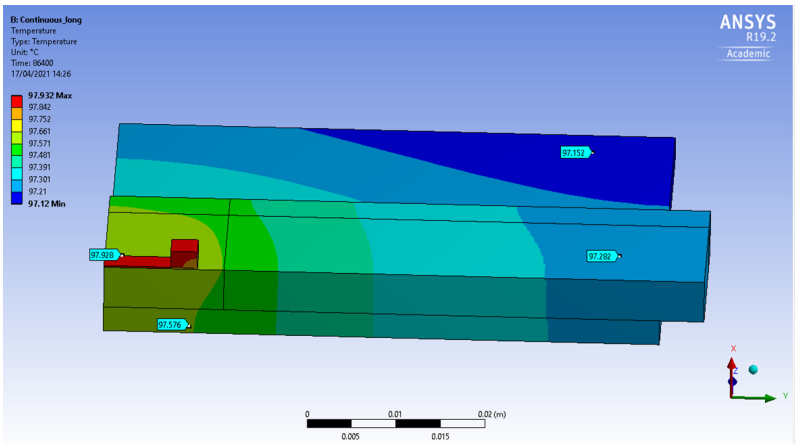

Figure A.2: Temperature distribution along the sample holder.

maximum temperature remains close to the ambient one. According to the present literature, the two temperature ranges are equivalent in terms of defect annealing for graphite. For the metallic coating this difference might play a role, and it should be considered when analysing the results.

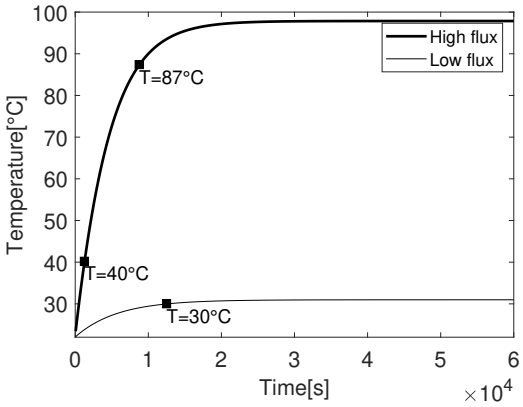

Figure A.3: Evolution of temperature on the irradiated sample as a function of time for high ($\phi = 8 \cdot 10^9 \ \frac{\text{ions}}{\text{cm}^2 \cdot \text{s}}$) and low ($\phi = 8 \cdot 10^8 \ \frac{\text{ions}}{\text{cm}^2 \cdot \text{s}}$) flux.

Appendix B

Raman spectroscopy analysis code

The analysis of the Raman spectra requires a deconvolution of the spectra in several peaks, and a fitting procedure of the data in order to extract the parameters for the microstructural characterization of the samples. The results presented in this work are obtained with a procedure implemented in a Matlab code, which is detailed below.

As explained in Sec. 4.3, five spectra per sample are collected. As a first step, the background induced by photoluminescence [136] is subtracted from the data. The procedure relies on a polynomial fitting of the background; this procedure is widely diffused and accepted [195]. The baseline fit and subtraction is applied with the code described in [196]. The user interactively selects the desired number of points of the curves for the fitting. The mean value of the curve over five points, centered on the selected ones, is calculated and then these values are used for a cubic spline interpolation. In Fig. B.1, one Raman spectrum of a graphite sample is shown before and after the background subtraction, and the baseline is also represented.

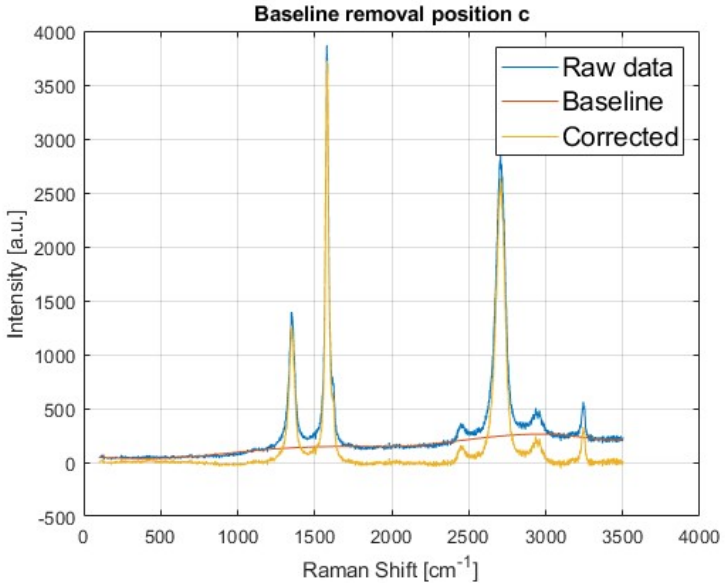

Figure B.1: Raman spectrum of one of the graphite samples analysed. In the graph, the raw data, the baseline interpolated with the aforementioned code, and the data with the baseline removed are plotted.

The five spectra are then averaged and the analysis is carried out for this spectrum. Before fitting the data, they are normalized by the maximum intensity, which always correspond to the G peak at $\approx 1582\ cm^{-1}$.

The different steps of the procedure are summarized in Fig. B.2.

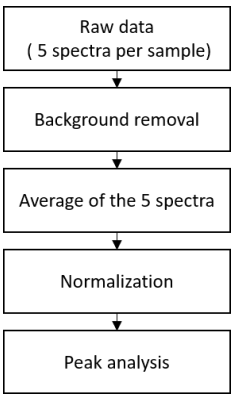

Figure B.2: Procedure implemented for the analysis of the Raman spectra.

The resulting spectrum is then decomposed to individuate the single component of the overlapping peaks with the code described in [197]. The curve is not fitted as a whole, but five independent intervals are analysed:

- The D, G and D' peaks are analysed together
- The 2D band peaks are analysed together
- The band at $\approx 2450\ cm^{-1}$ is fitted as a single peak
- The band at $\approx 2950\ cm^{-1}$ is fitted as a single peak
- The 2D' is fitted as a single peak

The main input parameters required for the code are specified in Tab. B.1 for the five groups of peaks analysed. The number of peaks, the peak shapes, and their initial position are assigned according to the literature [144].

In Fig. B.3 the result of the fitting is shown and compared with the experimental data.

The fitting of the 2D band is done with two peaks in MoGr grades, while only one is used for Gr and CFC. This choice comes from the experimental observation that the 2D shape is repeatably different for the aforementioned materials, as shown in Fig. B.4. As a trial, the 2D band of graphite and CFC is fitted also with a three-peaks model, as described in [147]. This solution is however discarded. Although a mathematical solution is found, the position and relative intensities of the peaks are not coherent with what is expected in literature.

On the top of the peak deconvolution, the program gives as output all the peak parameters (position, height, width, area), and the fitting error. These parameters are used to quantify the level of order in the graphite structure.

	D,G,D'	2D	band at ≈ 2450 cm^{-1}	band at ≈ 2950 cm^{-1}	2D'
Center of the interval [cm^{-1}]	1500	2690	2450	2950	3250
Window of the interval [cm^{-1}]	500	1000	200	200	200
# Peaks	3	1 or 2	1	1	1
Peak shape	Lorentzian	Lorentzian	Gaussian	Gaussian	Lorentzian
# Trials	40	40	10	10	10
Start guess position-width [cm^{-1}]	1352-25 1580-30 1620-5	2690-30 or 2675-15 2730-15	2450-50	2950-100	3250-100
Minimum width [cm^{-1}]	2	5	10	5	10

Table B.1: Summary of the input parameters to fit the peaks of the Raman spectra of the analysed materials.

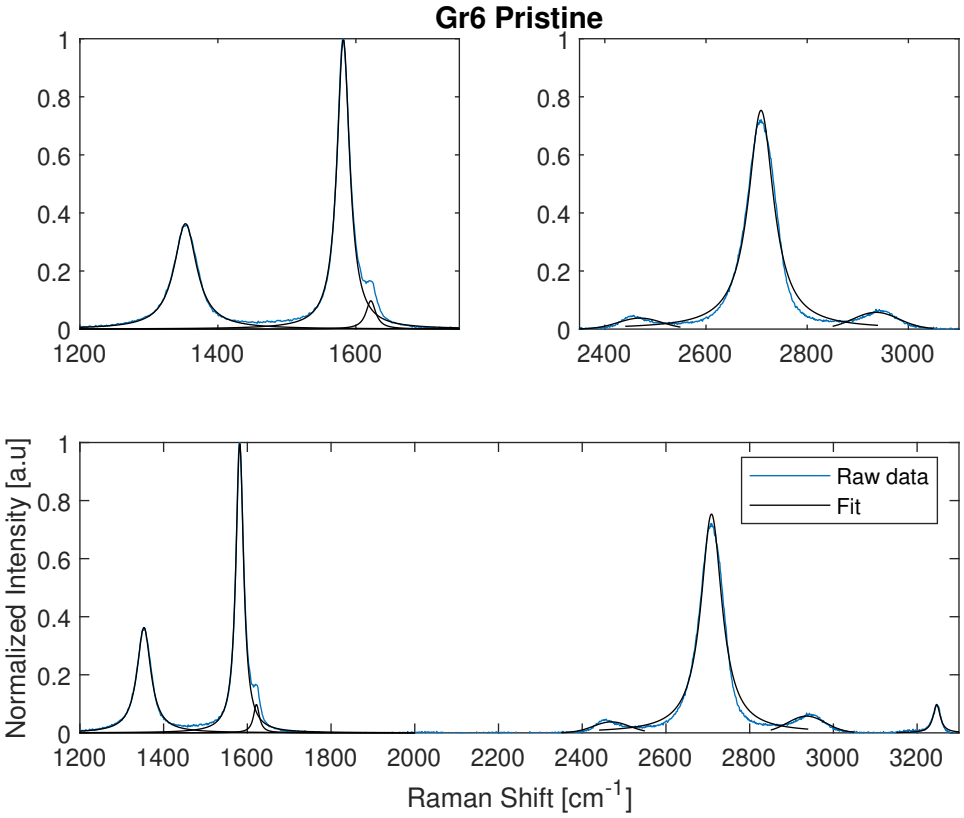

Figure B.3: The average and normalized Raman spectrum of a graphite sample is compared with the peak deconvolution obtained from the aforementioned code.

B.0.1 Irradiated materials

The aforementioned procedure is applied also to irradiated samples. At high dpa, some samples require however a different fitting. In particular, an additional peak

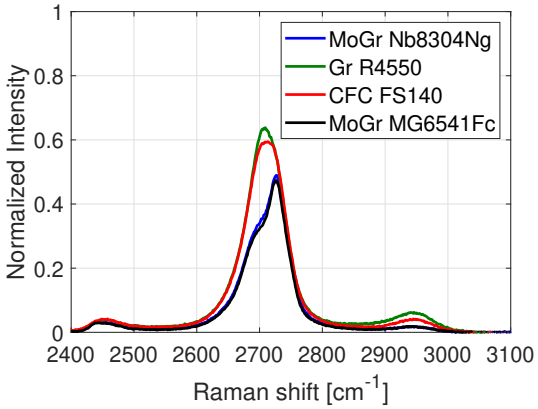

Figure B.4: 2D band of MoGr grades, graphite and CFC.

at $\approx 1500\ cm^{-1}$ is required to obtain a correct fit of the first order band. Without this peak, the experimental curve cannot be reproduced, and the intensity of the G peak is underestimated. In Fig. B.5, the experimental curve of a graphite sample irradiated at the maximum fluences is shown and compared with two fitting, one including the additional peak, and the other without. The curve that better replicate the experimental one includes the peak at $\approx 1500\ cm^{-1}$. This peak is observed both in soot [198], but also in ion-irradiated graphite [37].

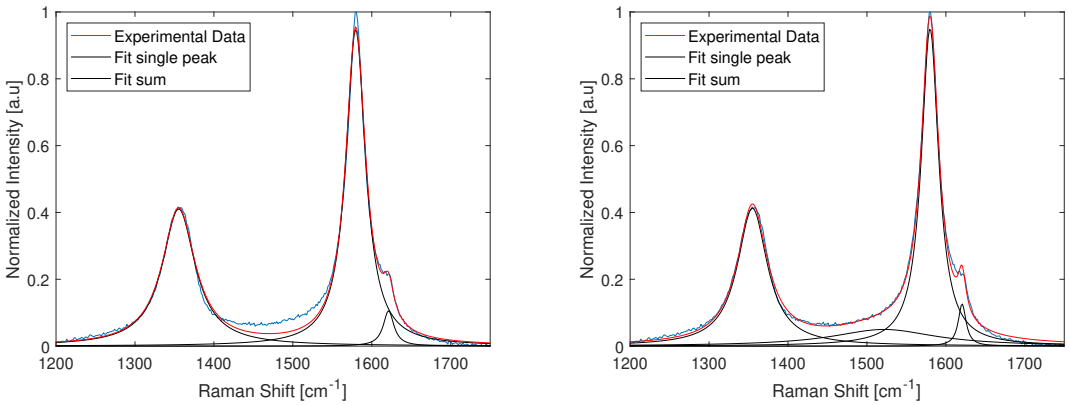

(a) Three-peaks fit of the first order spectra of irradiated graphite.

(b) Four-peaks fit of the first order spectra of irradiated graphite.

Figure B.5: Experimental curve and fitting of the graphite sample irradiated at the maximum fluence.

B.0.2 Uncertainty calculation

For the characterization before irradiation, six samples of each materials are characterized. The error bars of the peak parameters presented in 5.1.2 are therefore calculated as the standard deviation of the values found in the different samples tested.

For irradiated samples, this approach is not possible, as one sample of each materials is tested for each fluence. The main source of uncertainty comes from the

fact that the Raman spectra after irradiation are not taken exactly in the same point as before irradiation, and the dispersion between the spectra obtained in different points can affect the outcome. For this reason, one non-irradiated sample for each materials is considered, and the fitting analysis is performed for the spectra acquired in every position instead of on the average one. In this way, it is possible to estimate the expected variation of the parameters used for the analysis. The normalized spectra acquired in the five positions of one sample for the analysed materials are represented in Fig. B.6.

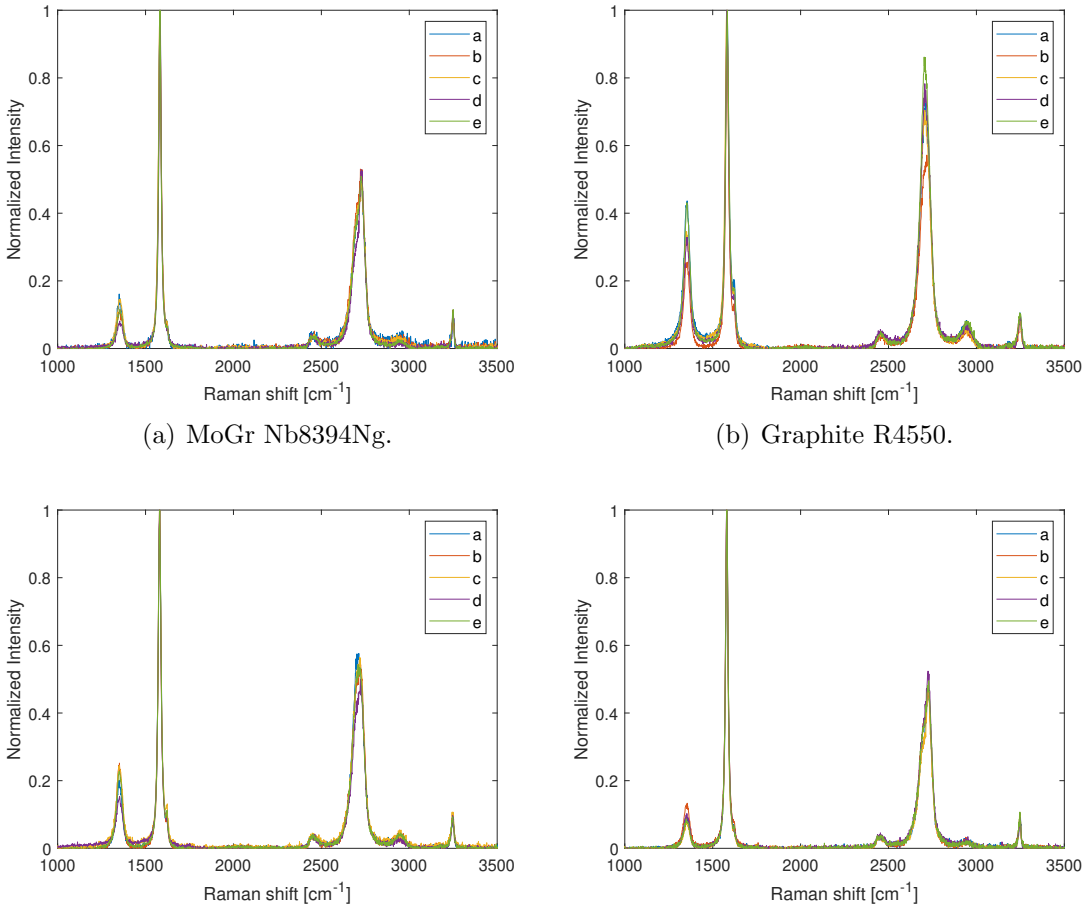

(a) MoGr Nb8394Ng.

(b) Graphite R4550.

(c) CFC FS140.

(d) MoGr MG6541Fc.

Figure B.6: Normalized spectra acquired in five different position of the samples for the four different materials analysed.

For each of this spectrum, a fitting procedure is implemented, as explained in the previous section. The average of the relevant parameters extracted from the fitting is calculated, together with their standard deviation (SD) and the percentage uncertainty. These values are presented in Tab. B.2,B.3,B.4,B.5 for the different materials.

The percentage uncertainties are then used to calculate the SD of each quantity, before and after irradiation. The flux is considered in fact uniform over the sample, and it is thus reasonable to assume a similar SD for the irradiated samples.

The analysis presented in 6.1.2 is based on the evolution of the parameters of

	I_D/I_G	FWHM$_G$	I_{2D_A}/I_{2D_B}
Average	0.12	17.39	0.73
SD	0.03	1.25	0.18
Uncertainty [%]	25	7	24

Table B.2: from the fitting of five Raman spectra of one sample of MoGr Nb8304Ng.

	I_D/I_G	FWHM$_G$	I_{2D}/I_G
Average	0.36	21.98	0.75
SD	0.07	1.59	0.10
Uncertainty [%]	21	7	14

Table B.3: from the fitting of five Raman spectra of one sample of graphite R4550.

	I_D/I_G	FWHM$_G$	I_{2D}/I_G
Average	0.22	19.31	0.57
SD	0.05	0.68	0.04
Uncertainty [%]	21	4	7

Table B.4: from the fitting of five Raman spectra of one sample of CFC FS140.

	I_D/I_G	FWHM$_G$	I_{2D_A}/I_{2D_B}
Average	0.10	17.23	0.64
SD	0.02	0.87	0.08
Uncertainty [%]	22	5	12

Table B.5: from the fitting of five Raman spectra of one sample of MoGr Mg6541Fc.

interest normalized for their values before irradiation. As the ratio between pristine and irradiated values is used, the rule of combined uncertainty is used, according to Eq. B.2 [134].

$$u = f(x_1, x_2, ..., x_N) \tag{B.1}$$

$$u_c^2(y) = \sum_{i=1}^{N} \left(\frac{\partial f}{\partial x_i} \right)^2 u^2(x_i) = \sum_{i=1}^{N} c_i^2 \, u^2(x_i) \tag{B.2}$$

In this case, the function is simply the ratio of two quantities, and Eq. B.2 is reduced to Eq. B.2 ratio.

$$u = \frac{x}{y} \tag{B.3}$$

$$u_c^2(y) = \left(\frac{x}{y} \right)^2 \left(\frac{{u_x}^2}{x} + \frac{{u_y}^2}{y} \right) \tag{B.4}$$

Bibliography

[1] URL: https://eucard2.web.cern.ch/eucard2/.

[2] URL: https://aries.web.cern.ch/.

[3] Peter Sigmund. "Particle penetration and radiation effects volume 2". In: *Springer series in solid-state sciences*. Vol. 179. Springer, 2014.

[4] Hem Raj Verma. *Atomic and nuclear analytical methods*. Springer, 2007.

[5] Stefaan Tavernier. *Experimental techniques in nuclear and particle physics*. Springer Science & Business Media, 2010.

[6] Ervin B Podgoršak et al. *Radiation physics for medical physicists*. Vol. 1. Springer, 2006.

[7] Glenn F Knoll. *Radiation detection and measurement*. John Wiley & Sons, 2010.

[8] John R Lamarsh and Anthony John Baratta. *Introduction to nuclear engineering*. Vol. 3. Prentice hall Upper Saddle River, NJ, 2001.

[9] Ronald Allen Knief. "Nuclear energy technology: theory and practice of commercial nuclear power". In: (1981).

[10] Anton Lechner. "CERN: Particle interactions with matter". In: *CERN Yellow Rep. School Proc.* 5 (2018), p. 47.

[11] A Bertarelli. "Beam-Induced Damage Mechanisms and their Calculation". In: arXiv:1608.03056 (Aug. 2016). Comments: 69 pages, contribution to the 2014 Joint International Accelerator School: Beam Loss and Accelerator Protection, Newport Beach, CA, USA , 5-14 Nov 2014, 69 p. DOI: 10.5170/CERN-2016-002.159. URL: https://cds.cern.ch/record/2207167.

[12] NV Mokhov and F Cerutti. "Beam-Material Interaction". In: *arXiv preprint arXiv:1608.02476* (2016).

[13] Daniela Kiselev. "Activation and radiation damage in the environment of hadron accelerators". In: *arXiv preprint arXiv:1303.6520* (2013).

[14] Marc Tavlet and Sorin Ilie. "Behaviour of organic materials in radiation environment". In: *1999 Fifth European Conference on Radiation and Its Effects on Components and Systems. RADECS 99 (Cat. No. 99TH8471)*. IEEE. 1999, pp. 210–215.

[15] Alexander Wu Chao, Karl Hubert Mess, et al. *Handbook of accelerator physics and engineering*. World scientific, 2013.

[16] Nikolai V Mokhov. "Beam—Materials Interactions". In: *Reviews of Accelerator Science and Technology*. World Scientific, 2014, pp. 275–290.

[17] Dan Gabriel Cacuci. *Handbook of Nuclear Engineering: Vol. 1: Nuclear Engineering Fundamentals; Vol. 2: Reactor Design; Vol. 3: Reactor Analysis; Vol. 4: Reactors of Generations III and IV; Vol. 5: Fuel Cycles, Decommissioning, Waste Disposal and Safeguards*. Springer Science & Business Media, 2010.

[18] Gary S Was. *Fundamentals of radiation materials science: metals and alloys*. springer, 2016.

[19] J Knaster, A Moeslang, and T Muroga. "Materials research for fusion". In: *Nature Physics* 12.5 (2016), pp. 424–434.

[20] MJ Norgett, MT Robinson, and IM Torrens. "A proposed method of calculating displacement dose rates". In: *Nuclear engineering and design* 33.1 (1975), pp. 50–54.

[21] Kai Nordlund et al. *Primary Radiation Damage in Materials. Review of Current Understanding and Proposed New Standard Displacement Damage Model to Incorporate in Cascade Defect Production Efficiency and Mixing Effects*. Tech. rep. Organisation for Economic Co-Operation and Development, 2015.

[22] TT Böhlen et al. "The FLUKA code: developments and challenges for high energy and medical applications". In: *Nuclear data sheets* 120 (2014), pp. 211–214.

[23] Giuseppe Battistoni et al. "Overview of the FLUKA code". In: *Annals of Nuclear Energy* 82 (2015), pp. 10–18.

[24] Nikolai V Mokhov. *The MARS code system user's guide version 13 (95)*. Tech. rep. SCAN-9506126, 1995.

[25] Alberto Fasso et al. "FLUKA realistic modeling of radiation induced damage". In: *Progress in Nuclear Science and Technology* 2 (2011), pp. 769–775.

[26] Jaroslav Koutsk and Jan Kocik. *Radiation damage of structural materials*. Elsevier, 2013.

[27] Kai Nordlund et al. "Improving atomic displacement and replacement calculations with physically realistic damage models". In: *Nature communications* 9.1 (2018), pp. 1–8.

[28] H Ullmaier. "Radiation damage in metallic materials". In: *Mrs Bulletin* 22.4 (1997), pp. 14–21.

[29] SJ Zinkle and BN Singh. "Analysis of displacement damage and defect production under cascade damage conditions". In: *Journal of nuclear materials* 199.3 (1993), pp. 173–191.

[30] J-P Riviere. "Radiation induced point defects and diffusion". In: *Application of Particle and Laser Beams in Materials Technology*. Springer, 1995, pp. 53–76.

[31] RA Johnson and Aleksej Nikolaevič Orlov. *Physics of radiation effects in crystals*. Elsevier, 2012.

[32] Rudy Konings and Roger E Stoller. *Comprehensive nuclear materials*. Elsevier, 2020.

[33] Joshua Pelleg. "Introduction to dislocations". In: *Mechanical Properties of Materials*. Springer, 2013, pp. 85–146.

[34] John Harry Walrond Simmons. *Radiation damage in graphite: international series of monographs in nuclear energy*. Vol. 102. Elsevier, 2013.

[35] Nicholas Simos et al. "Radiation Effects in Material Microstructure". In: *The Seventeenth International Offshore and Polar Engineering Conference*. International Society of Offshore and Polar Engineers. 2007.

[36] RS Averback. "Atomic displacement processes in irradiated metals". In: *Journal of nuclear materials* 216 (1994), pp. 49–62.

[37] Christian Hubert. "Characterization of radiation damage induced by swift heavy ions in graphite". PhD thesis. Technische Universität Darmstadt, Darmstadt, Germany, 2016.

[38] P Hurh et al. *Targetry Challenges at Megawatt Proton Accelerator Facilities*. Tech. rep. Fermi National Accelerator Lab.(FNAL), Batavia, IL (United States), 2013.

[39] J Liu et al. "Tracks of swift heavy ions in graphite studied by scanning tunneling microscopy". In: *Physical Review B* 64.18 (2001), p. 184115.

[40] M Bender et al. "Material-related issues at high-power and high-energy ion beam facilities". In: *Journal of Physics: Conference Series*. Vol. 599. CERN-ACC-2015-0214. 2015.

[41] Safa Kasap, Cyril Koughia, and Harry E Ruda. "Electrical conduction in metals and semiconductors". In: *Springer Handbook of Electronic and Photonic Materials*. Springer, 2017, pp. 1–1.

[42] BV Cockeram, JL Hollenbeck, and LL Snead. "Hardness and electrical resistivity of molybdenum in the post-irradiated and annealed conditions". In: *Journal of nuclear materials* 336.2-3 (2005), pp. 299–313.

[43] LL Snead, SJ Zinkle, and DP White. "Thermal conductivity degradation of ceramic materials due to low temperature, low dose neutron irradiation". In: *Journal of nuclear materials* 340.2-3 (2005), pp. 187–202.

[44] BT Kelly and JE Brocklehurst. "High dose fast neutron irradiation of highly oriented pyrolytic graphite". In: *Carbon* 9.6 (1971), pp. 783–789.

[45] JP Bonal and CH Wu. "Neutron irradiation effects on the thermal conductivity and the dimensional stability of carbon fiber composites". In: *Physica Scripta* 1996.T64 (1996), p. 26.

[46] CH Wu, JP Bonal, and B Thiele. "Thermal conductivity changes in graphites and carbon/carbon fiber materials induced by low neutron damages". In: *Journal of nuclear materials* 212 (1994), pp. 1168–1173.

[47] Tadashi Maruyama and Masaaki Harayama. "Neutron irradiation effect on the thermal conductivity and dimensional change of graphite materials". In: *Journal of Nuclear Materials* 195.1-2 (1992), pp. 44–50.

[48] W Primak and LH Fuchs. “Radiation damage to the electrical conductivities of natural graphite crystals”. In: *Physical Review* 103.3 (1956), p. 541.

[49] LCF Blackman, G Saunders, and AR Ubbelohde. “Radiation Damage in Well Oriented Pyrolytic Graphites”. In: *Proceedings of the Physical Society* 78.5 (1961), p. 1048.

[50] Alexey Prosvetov et al. “Degradation of thermal transport properties in fine-grained isotropic graphite exposed to swift heavy ion beams”. In: *Acta Materialia* 184 (2020), pp. 187–198.

[51] Sandrina Fernandes et al. “In-situ electric resistance measurements and annealing effects of graphite exposed to swift heavy ions”. In: *Nuclear Instruments and Methods in Physics Research Section B: Beam Interactions with Materials and Atoms* 314 (2013), pp. 125–129.

[52] Laura de Sousa Oliveira and P Alex Greaney. “Thermal resistance from irradiation defects in graphite”. In: *Computational Materials Science* 103 (2015), pp. 68–76.

[53] JT Adrian Roberts. *Structural materials in nuclear power systems*. Springer Science & Business Media, 2013.

[54] FA Nichols. “How Does One Predict and Measure Radiation Damage?” In: *Nuclear Technology* 40.1 (1978), pp. 98–105.

[55] M Griffiths. “Evolution of microstructure in hcp metals during irradiation”. In: *Journal of nuclear materials* 205 (1993), pp. 225–241.

[56] TD Burchell. “Radiation effects in graphite and carbon-based materials”. In: *MRS bulletin* 22.4 (1997), pp. 29–35.

[57] BT Kelly et al. “Irradiation damage in graphite due to fast neutrons in fission and fusion systems”. In: *IAEA Tecdoc* 1154 (2000).

[58] N Simos et al. “Proton irradiated graphite grades for a long baseline neutrino facility experiment”. In: *Physical Review Accelerators and Beams* 20.7 (2017), p. 071002.

[59] A Burkholz. “Irradiation Damage in Graphite. EUR 3056.” In: (1966).

[60] Federico Carra. “Thermomechanical response of advanced materials under quasi instantaneous heating”. PhD thesis, Politecnico di Torino, Italy. PhD thesis. 2017.

[61] Lucio Rossi. “The large hadron collider and the role of superconductivity in one of the largest scientific enterprises”. In: *IEEE Transactions on applied superconductivity* 17.2 (2007), pp. 1005–1014.

[62] Tiziana Spina. “Proton irradiation effects on Nb3Sn wires and thin platelets in view of High Luminosity LHC upgrade”. PhD thesis, University of Geneva, Switzerland. PhD thesis. 2015.

[63] Sören Möller. *Accelerator Technology: Applications in Science, Medicine, and Industry*. Springer Nature.

[64] Werner Herr and Bruno Muratori. “Concept of luminosity”. In: (2006).

[65] MA Plum. "Protection Related to High-power Targets". In: *arXiv preprint arXiv:1608.02787* (2016).

[66] M Benedikt et al. "LHC Design Report, volume III, The LHC injector chain". In: *CERN, Geneva* (2004).

[67] Georges Aad et al. "The ATLAS experiment at the CERN large hadron collider". In: *Jinst* 3 (2008), S08003.

[68] Kenneth Aamodt et al. "The ALICE experiment at the CERN LHC". In: *Journal of Instrumentation* 3.08 (2008), S08002.

[69] Serguei Chatrchyan et al. "The CMS experiment at the CERN LHC". In: *Journal of instrumentation* 3.8 (2008), S08004.

[70] A Augusto Alves Jr et al. "The LHCb detector at the LHC". In: *Journal of instrumentation* 3.08 (2008), S08005.

[71] Oliver Brüning et al. "LHC design report(Volume I, The@ LHC main ring)". In: *Reports- CERN* (2004).

[72] JC Brunet et al. "Mechanical design and layout of the LHC standard half-cell". In: *Proceedings of the 1997 Particle Accelerator Conference (Cat. No. 97CH36167)*. Vol. 3. IEEE. 1997, pp. 3368–3370.

[73] L Rossi. "The LHC superconducting magnets". In: *Proceedings of the 2003 Particle Accelerator Conference*. Vol. 1. IEEE. 2003, pp. 141–145.

[74] BJ Holzer. "Introduction to particle accelerators and their limitations". In: *arXiv preprint arXiv:1705.09601* (2017).

[75] Alexander V Zlobin and Daniel Schoerling. "Superconducting Magnets for Accelerators". In: *Nb3Sn Accelerator Magnets*. Springer, Cham, 2019, pp. 3–22.

[76] Lucio Rossi and Luca Bottura. "Superconducting magnets for particle accelerators". In: *Reviews of accelerator science and technology* 5 (2012), pp. 51–89.

[77] B Auchmann et al. "Testing beam-induced quench levels of LHC superconducting magnets". In: *Physical Review Special Topics-Accelerators and Beams* 18.6 (2015), p. 061002.

[78] Stefano Redaelli. "Beam cleaning and collimation systems". In: *arXiv preprint arXiv:1608.03159* (2016).

[79] RW Assmann et al. *Requirements for the LHC collimation system*. Tech. rep. 2002.

[80] Elena Quaranta. "Investigation of collimator materials for the high luminosity Large Hadron Collider". PhD thesis, Politecnico di Milano, Italy. PhD thesis. 2017.

[81] RW Assmann et al. *The final collimation system for the LHC*. Tech. rep. 2006.

[82] A Bertarelli et al. "The Mechanical Design for the LHC Collimators". In: LHC-Project-Report-786. CERN-LHC-Project-Report-786 (Aug. 2004), 4 p. URL: https://cds.cern.ch/record/794628.

[83] Rainer Wanzenberg. "Impedances and Instabilities". In: *arXiv preprint arXiv:2006.06540* (2020).

[84] E Métral. *Transverse resistive-wall impedance from very low to very high frequencies*. Tech. rep. 2005.

[85] Paolo Chiggiato. *Outgassing of vacuum materials and its reduction*. 2004.

[86] J.M. Jimenez. "Vacuum requirements for LHC collimators". In: *CERN EDMS note* 428155 (2003).

[87] G Bregliozzi et al. "Description of criteria for vacuum acceptance test". In: *CERN EDMS note* 1753872 (2017).

[88] C Accettura et al. "Ultra-High Vacuum characterization of Molybdenum-Carbide Graphite for HL-LHC collimators". In: *Journal of Physics: Conference Series*. Vol. 1350. 1. IOP Publishing. 2019, p. 012085.

[89] Hugh O Pierson. *Handbook of carbon, graphite, diamonds and fullerenes: processing, properties and applications*. William Andrew, 2012.

[90] Nicola Mariani. *Development of novel, advanced molybdenum based composites for high energy physics applications*. PhD thesis,Politecnico di Milano, Italy. 2014.

[91] CMS Collaboration, ATLAS Collaboration, et al. *Cern experiments observe particle consistent with long-sought higgs boson*. 2012.

[92] Giorgio Apollinari et al. "High luminosity large hadron collider HL-LHC". In: *arXiv preprint arXiv:1705.08830* (2017).

[93] Federico Carra et al. *Mechanical engineering and design of novel collimators for HL-LHC*. Tech. rep. 2014.

[94] S Redaelli et al. "Cleaning insertions and collimation challenges". In: *The High Luminosity Large Hadron Collider: The New Machine for Illuminating the Mysteries of Universe*. World Scientific, 2015, pp. 215–241.

[95] SA Antipov et al. "Transverse beam stability with low-impedance collimators in the High-Luminosity Large Hadron Collider: Status and challenges". In: *Physical Review Accelerators and Beams* 23.3 (2020), p. 034403.

[96] Laura Bianchi. "Thermophysical and mechanical characterization of advanced materials for the LHC collimation system". Master thesis,INFN, Pisa, Italy. PhD thesis. 2017.

[97] Carlotta Accettura. "Ultra-high vacuum characterization of advanced materials for future particle accelerators". Master thesis, Politecnico di Milano, Italy. PhD thesis. 2017.

[98] I Efthymiopoulos et al. *HiRadMat: a new irradiation facility for material testing at CERN*. Tech. rep. 2011.

[99] A Bertarelli et al. "Dynamic testing and characterization of advanced materials in a new experiment at CERN HiRadMat facility". In: *Journal of Physics: Conference Series*. Vol. 1067. 8. 2018.

[100] Giorgia Gobbi et al. "Novel LHC collimator materials: High-energy Hadron beam impact tests and nondestructive postirradiation examination". In: *Mechanics of Advanced Materials and Structures* (2019), pp. 1–13.

[101] Federico Carra et al. "Mechanical robustness of HL-LHC collimator designs". In: *Journal of Physics: Conference Series*. Vol. 1350. 1. IOP Publishing. 2019, p. 012083.

[102] M Pasquali et al. "Dynamic response of advanced materials impacted by particle beams: the MultiMat experiment". In: *Journal of Dynamic Behavior of Materials* 5.3 (2019), pp. 266–295.

[103] Jorge Guardia-Valenzuela et al. "Development and properties of high thermal conductivity molybdenum carbide-graphite composites". In: *Carbon* 135 (2018), pp. 72–84.

[104] Stefano Redaelli et al. *Staged implementation of low-impedance collimation in IR7: plans for LS2*. Tech. rep. 2019.

[105] Bahamonde Castro Cristina and Perez Martinez Rita. "TCSPM endoscopy". In: *LHC Collimation Working Group 244* CERN (2019).

[106] C. Accettura et al. "Conditioning of uncoated Molybdenum-Graphite for LHC collimators". In: *CERN EDMS note* 2050564 (2020).

[107] C. Accettura et al. "Conditioning of Molybdenum-Graphite for LHC collimators before and after coating". In: *CERN EDMS note* 2067775 (2020).

[108] E Quaranta et al. "Modeling of beam-induced damage of the LHC tertiary collimators". In: *Physical Review Accelerators and Beams* 20.9 (2017), p. 091002.

[109] Eleftherios Skordis. "Radiation impact of collimation beam losses in the LHC and HL-LHC". PhD thesis,University of Liverpool, England. PhD thesis. 2019.

[110] URL: `http://sixtrack.web.cern.ch/SixTrack/`.

[111] R Bruce et al. "Status of Sixtrack with collimation". In: (2018).

[112] DJ Mazey. "Fundamental aspects of high-energy ion-beam simulation techniques and their relevance to fusion materials studies". In: *Journal of nuclear materials* 174.2-3 (1990), pp. 196–209.

[113] SJ Jepeal, Lance Snead, and ZS Hartwig. "Intermediate energy proton irradiation: rapid, high-fidelity materials testing for fusion and fission energy systems". In: *Materials & Design* (2020), p. 109445.

[114] Pavel Vladimirov and Serge Bouffard. "Displacement damage and transmutations in metals under neutron and proton irradiation". In: *Comptes Rendus Physique* 9.3-4 (2008), pp. 303–322.

[115] N Galy et al. "Ion irradiation used as surrogate of neutron irradiation in graphite: Consequences on 14 C and 36 Cl behavior and structural evolution". In: *JNuM* 502 (2018), pp. 20–29.

[116] Lee C Northcliffe and R Fo Schilling. "Range and stopping-power tables for heavy ions". In: *Atomic Data and Nuclear Data Tables* 7.3-4 (1970), pp. 233–463.

[117] Gary S Was. "Challenges to the use of ion irradiation for emulating reactor irradiation". In: *Journal of Materials Research* 30.9 (2015), p. 1158.

[118] N Simos et al. "Multi-MW accelerator target material properties under proton irradiation at Brookhaven National Laboratory linear isotope producer". In: *Physical Review Accelerators and Beams* 21.5 (2018), p. 053001.

[119] Timothy D Burchell. "Radiation damage in carbon–carbon composites: structure and property effects". In: *Physica scripta* 1996.T64 (1996), p. 17.

[120] TD Burchell and T Oku. "Material properties data for fusion reactor plasma facing carbon-carbon composites". In: *Atomic and Plasma-Material Interaction Data for Fusion* 5 (1994), pp. 77–128.

[121] A Ryazanov et al. *Effect of High-energy Proton Beam Irradiation on the Behaviour of Graphite Collimator Materials for LHC*. Tech. rep. 2010.

[122] N Simos et al. "Radiation damage and thermal shock response of carbon-fiber-reinforced materials to intense high-energy proton beams". In: *Physical Review Accelerators and Beams* 19.11 (2016), p. 111002.

[123] J Stadlmann et al. *OVERVIEW OF EUCARD ACCELERATOR AND MATERIAL RESEARCH AT GSI*. Tech. rep. EuCARD-CON-2013-003. 2011.

[124] M Tomut et al. *Heavy ion induced radiation effects in novel molybdenum-carbide graphite composite materials*. Tech. rep. GSI Report 2015-1, 266 p. 'GSI', 2015.

[125] N Simos et al. "Proton irradiation effects in Molybdenum-Carbide-Graphite composites". In: *Journal of Nuclear Materials* (2021), p. 153049.

[126] URL: `https://radiate.fnal.gov/`.

[127] Carlotta Accettura et al. "Resistivity Characterization of Molybdenum-Coated Graphite-Based Substrates for High-Luminosity LHC Collimators". In: *Coatings* 10.4 (2020), p. 361.

[128] M. Pasquali et al. "Dynamic Response of Advanced Materials Impacted by Particle Beams: The MultiMat Experiments". In: *Journal of Dynamic Behavior of Materials* 5.3 (2019), pp. 266–295.

[129] B Snaith, SD Probert, and PW O'Callaghan. "Thermal resistances of pressed contacts". In: *Applied Energy* 22.1 (1986), pp. 31–84.

[130] Martha Borg et al. "Thermostructural characterization and structural elastic property optimization of novel high luminosity LHC collimation materials at CERN". In: *Physical Review Accelerators and Beams* 21.3 (2018), p. 031001.

[131] RS Sandhu. *A survey of failure theories of isotropic and anisotropic materials*. Tech. rep. AIR FORCE FLIGHT DYNAMICS LAB WRIGHT-PATTERSON AFB OH, 1972.

[132] Michael B. Heaney. *Electrical Measurement, Signal Processing, and Displays*. CRC Press, 2003.

[133] J. Guardia-Valenzuela. "Optimisation of Graphite-Matrix Composites for Collimators in the LHC Upgrade". PhD thesis, Universidad de Zaragoza. PhD thesis. 2019.

[134] *Evaluation of measurement data - Guide to the expression of uncertainty in measurement*. JCGM 100:2008. `https://www.bipm.org/utils/common/documents/jcgm/JCGM_100_2008_E.pdf`. 2008.

[135] PRGDJ Graves and D Gardiner. "Practical raman spectroscopy". In: *Springer* (1989).

[136] Peter Vandenabeele. *Practical Raman spectroscopy: an introduction*. Wiley Online Library, 2013.

[137] Peter Larkin. *Infrared and Raman spectroscopy: principles and spectral interpretation*. Elsevier, 2017.

[138] R Merlin, A Pinczuk, and WH Weber. "Overview of phonon Raman scattering in solids". In: *Raman scattering in materials science*. Springer, 2000, pp. 1–29.

[139] LG Cançado. "Raman spectroscopy of nanographites". PhD thesis, Department of Physics-Federal University of Minas Gerais, Brasil. PhD thesis. 2006.

[140] Jenő Sólyom. "The Quantum Theory of Lattice Vibrations". In: *Fundamentals of the Physics of Solids*. Springer, 2007, pp. 387–428.

[141] MA Pimenta et al. "Studying disorder in graphite-based systems by Raman spectroscopy". In: *Physical chemistry chemical physics* 9.11 (2007), pp. 1276–1290.

[142] Andrea C Ferrari. "Raman spectroscopy of graphene and graphite: Disorder, electron–phonon coupling, doping and nonadiabatic effects". In: *Solid state communications* 143.1-2 (2007), pp. 47–57.

[143] Andrea C Ferrari and John Robertson. "Interpretation of Raman spectra of disordered and amorphous carbon". In: *Physical review B* 61.20 (2000), p. 14095.

[144] Nicholas Larouche and Barry L Stansfield. "Classifying nanostructured carbons using graphitic indices derived from Raman spectra". In: *Carbon* 48.3 (2010), pp. 620–629.

[145] DDL Chung. "Review graphite". In: *Journal of materials science* 37.8 (2002), pp. 1475–1489.

[146] F Tuinstra and J Lo Koenig. "Raman spectrum of graphite". In: *The Journal of chemical physics* 53.3 (1970), pp. 1126–1130.

[147] LG Cancado et al. "Measuring the degree of stacking order in graphite by Raman spectroscopy". In: *Carbon* 46.2 (2008), pp. 272–275.

[148] Timothy D Burchell, Peter J Pappano, and Joe P Strizak. "A study of the annealing behavior of neutron irradiated graphite". In: *Carbon* 49.1 (2011), pp. 3–10.

[149] Michael Lasithiotakis, Barry J Marsden, and T James Marrow. "Annealing of ion irradiation damage in nuclear graphite". In: *Journal of nuclear materials* 434.1-3 (2013), pp. 334–346.

[150] Thomas M Devine and Fran Adar. "Raman Spectroscopy of Solids". In: *Characterization of Materials* (2002), pp. 1–38.

[151] Tao Mo et al. “Effect of carburization protocols on molybdenum carbide synthesis and study on its performance in CO hydrogenation”. In: *Catalysis Today* 261 (2016), pp. 101–115.

[152] BH Lohse, Al Calka, and D Wexler. “Raman spectroscopy as a tool to study TiC formation during controlled ball milling”. In: *Journal of applied physics* 97.11 (2005), p. 114912.

[153] Pierre Lespade et al. “Caracterisation de materiaux carbones par microspectrometrie Raman”. In: *Carbon* 22.4-5 (1984), pp. 375–385.

[154] LG Cançado et al. “General equation for the determination of the crystallite size L a of nanographite by Raman spectroscopy”. In: *Applied Physics Letters* 88.16 (2006), p. 163106.

[155] Axel Eckmann et al. “Probing the nature of defects in graphene by Raman spectroscopy”. In: *Nano letters* 12.8 (2012), pp. 3925–3930.

[156] GH Kinchin. “The electrical properties of graphite”. In: *Proceedings of the Royal Society of London. Series A. Mathematical and Physical Sciences* 217.1128 (1953), pp. 9–26.

[157] PD Desai et al. “Electrical resistivity of selected elements”. In: *Journal of physical and chemical reference data* 13.4 (1984), pp. 1069–1096.

[158] Felipe Cemin et al. “Low electrical resistivity in thin and ultrathin copper layers grown by high power impulse magnetron sputtering”. In: *Journal of Vacuum Science & Technology A: Vacuum, Surfaces, and Films* 34.5 (2016), p. 051506.

[159] AF Mayadas and M Shatzkes. “Electrical-resistivity model for polycrystalline films: the case of arbitrary reflection at external surfaces”. In: *Physical review B* 1.4 (1970), p. 1382.

[160] PB Barna and M Adamik. “Fundamental structure forming phenomena of polycrystalline films and the structure zone models”. In: *Thin solid films* 317.1-2 (1998), pp. 27–33.

[161] Kostas Sarakinos, J Alami, and Stephanos Konstantinidis. “High power pulsed magnetron sputtering: A review on scientific and engineering state of the art”. In: *Surface and Coatings Technology* 204.11 (2010), pp. 1661–1684.

[162] W Ensinger. “Low energy ion assist during deposition—an effective tool for controlling thin film microstructure”. In: *Nuclear Instruments and Methods in Physics Research Section B: Beam Interactions with Materials and Atoms* 127 (1997), pp. 796–808.

[163] J Alami et al. “On the relationship between the peak target current and the morphology of chromium nitride thin films deposited by reactive high power pulsed magnetron sputtering”. In: *Journal of Physics D: Applied Physics* 42.1 (2008), p. 015304.

[164] Mattias Samuelsson et al. “On the film density using high power impulse magnetron sputtering”. In: *Surface and Coatings Technology* 205.2 (2010), pp. 591–596.

[165] Ulf Helmersson et al. “Ionized physical vapor deposition (IPVD): A review of technology and applications”. In: *Thin solid films* 513.1-2 (2006), pp. 1–24.

[166] J Keraudy et al. “Comparison Between DC and HiPIMS Discharges. Application to Nickel Thin Films”. In: *International Conference on Engineering Research and Applications*. Springer. 2018, pp. 196–203.

[167] Dirk Ochs. “HIPIMS power for improved thin film coatings”. In: *Vakuum in Forschung und Praxis* 20.4 (2008), pp. 34–38.

[168] DM Hembree et al. “Raman spectroscopy of C-irradiated graphite”. In: *MRS Online Proceedings Library Archive* 279 (1992).

[169] Kazutaka Nakamura and Masahiro Kitajima. “Ion-irradiation effects on the phonon correlation length of graphite studied by Raman spectroscopy”. In: *Physical Review B* 45.1 (1992), p. 78.

[170] Jie Liu et al. “STM and Raman spectroscopic study of graphite irradiated by heavy ions”. In: *Nuclear Instruments and Methods in Physics Research Section B: Beam Interactions with Materials and Atoms* 212 (2003), pp. 303–307.

[171] PingHeng Tan et al. “Resonantly enhanced Raman scattering and high-order Raman spectra of single-walled carbon nanotubes”. In: *Applied physics letters* 75.11 (1999), pp. 1524–1526.

[172] Keisuke Niwase. “Raman spectroscopy for quantitative analysis of point defects and defect clusters in irradiated graphite”. In: *International Journal of Spectroscopy* 2012 (2012).

[173] T Jawhari, A Roid, and J Casado. “Raman spectroscopic characterization of some commercially available carbon black materials”. In: *Carbon* 33.11 (1995), pp. 1561–1565.

[174] Miroslawa Pawlyta, Jean-Noël Rouzaud, and Stanislaw Duber. “Raman microspectroscopy characterization of carbon blacks: Spectral analysis and structural information”. In: *Carbon* 84 (2015), pp. 479–490.

[175] K Niwase, T Tanabe, and I Tanaka. “Annealing experiment of ion-irradiated graphite by laser Raman spectroscopy”. In: *Journal of nuclear materials* 191 (1992), pp. 335–339.

[176] A. Baris. *Characterization of Molybdenum-Based Coatings on Graphite-Based Substrates by Focused Ion Beam Before and After Irradiation*. Tech. rep. EDMS 2340882. Geneva, Switzerland: CERN, Mar. 2020.

[177] K Niwase et al. “Electron microscope study of radiation damage in graphite produced by D+ and He+ bombardment”. In: *Journal of Nuclear Materials* 155 (1988), pp. 303–306.

[178] Wei Qi et al. “Behaviors of fine (IG-110) and ultra-fine (HPG-510) grain graphite irradiated by 7 MeV Xe 26+ ions”. In: *Nuclear Science and Techniques* 28.10 (2017), pp. 1–8.

[179] Qing Huang et al. "Raman spectra and modulus measurement on the cross section of proton-irradiated graphite". In: *Nuclear Instruments and Methods in Physics Research Section B: Beam Interactions with Materials and Atoms* 412 (2017), pp. 221–226.

[180] Tetsuo Tanabe. "Radiation damage of graphite-degradation of material parameters and defect structures". In: *Physica Scripta* 1996.T64 (1996), p. 7.

[181] Keisuke Niwase. "Irradiation-induced amorphization of graphite: a dislocation accumulation model". In: *Philosophical Magazine Letters* 82.7 (2002), pp. 401–408.

[182] RH Telling and MI Heggie. "Radiation defects in graphite". In: *Philosophical Magazine* 87.31 (2007), pp. 4797–4846.

[183] Jacob Eapen et al. "Early damage mechanisms in nuclear grade graphite under irradiation". In: *Materials Research Letters* 2.1 (2014), pp. 43–50.

[184] G Compagnini, O Puglisi, and G Foti. "Raman spectra of virgin and damaged graphite edge planes". In: *Carbon* 35.12 (1997), pp. 1793–1797.

[185] Alexey Prosvetov. "Ion-beam induced modifications of structural and thermophysical properties of graphite materials." PhD thesis, Technische Universität Darmstadt, Germany. PhD thesis. 2020.

[186] PingHeng Tan, Svetlana Dimovski, and Yury Gogotsi. "Raman scattering of non–planar graphite: arched edges, polyhedral crystals, whiskers and cones". In: *Philosophical Transactions of the Royal Society of London. Series A: Mathematical, Physical and Engineering Sciences* 362.1824 (2004), pp. 2289–2310.

[187] Alex Theodosiou, Albert Frederick Carley, and Stuart Hamilton Taylor. "Ion-induced damage in graphite: A Raman study". In: *Journal of nuclear materials* 403.1-3 (2010), pp. 108–112.

[188] Yutian Wang et al. "Defect-induced magnetism in graphite through neutron irradiation". In: *Physical Review B* 90.21 (2014), p. 214435.

[189] Christopher M Barr et al. "Interplay between grain boundaries and radiation damage". In: *JOM* 71.4 (2019), pp. 1233–1244.

[190] A. Kurtulus et al. "Detailed Electromagnetic Characterisation of HL-LHC Low Impedance Collimators". In: *presented at the 12th Int. Particle Accelerator Conf. (IPAC'21)* (Campinas, Brazil). JACoW Publishing, May 2021.

[191] Junichiro Kamiya et al. "Outgassing measurement of an LHC collimator and estimation for the NEG performances". In: *Vacuum* 85.12 (2011), pp. 1178–1181.

[192] PA Platonov et al. "Annealing of radiation damage in graphite". In: *Radiation Effects* 25.2 (1975), pp. 105–110.

[193] Koki Urita et al. "In situ observation of thermal relaxation of interstitial-vacancy pair defects in a graphite gap". In: *Physical review letters* 94.15 (2005), p. 155502.

[194] A Ammar and DA Young. "Electrical conduction in irradiated pyrolytic graphite". In: *British Journal of Applied Physics* 15.2 (1964), p. 131.

[195] PJ Cadusch et al. “Improved methods for fluorescence background subtraction from Raman spectra”. In: *Journal of Raman Spectroscopy* 44.11 (2013), pp. 1587–1595.

[196] Mirko Hrovat. *Baseline Fit*. Retrieved March 11, 2021. URL: https://mathworks.com/matlabcentral/fileexchange/24916-baseline-fit/.

[197] Tom O’Haver. *Matlab/Octave Peak Fitters*. URL: https://terpconnect.umd.edu/~toh/spectrum/InteractivePeakFitter.htm.

[198] Alexa Sadezky et al. “Raman microspectroscopy of soot and related carbonaceous materials: spectral analysis and structural information”. In: *Carbon* 43.8 (2005), pp. 1731–1742.